REPORT DOCUMENTATION PAGE

AFRL-SR-AR-TR-06-0023

1. REPORT DATE *(DD-MM-YYYY)*	2. REPORT TYPE	3. DATES COVERED *(From - To)*
31 October, 2005	Final Report	Sept. 1, 2001–June 30, 2005

4. TITLE AND SUBTITLE
Low Defect Density Substrates and High-Quality Epi-Substrate Interfaces for ABCS Devices and Progress Toward Phonon-Mediated THz Lasers

5a. CONTRACT NUMBER
F49620-01-1-0514

5b. GRANT NUMBER

5c. PROGRAM ELEMENT NUMBER

6. AUTHOR(S)
William Goodhue, David Bliss, Kannan Krishnaswami, Shivashankar Vangala, Jin Li ,

and Beihong Zhu

5d. PROJECT NUMBER
UMRF S13389280F00006

5e. TASK NUMBER

5f. WORK UNIT NUMBER

7. PERFORMING ORGANIZATION NAME(S) AND ADDRESS(ES)

University of Massachusetts-Lowell
Research Administration
Dugan Hall Rm 201
883 Broadway St.
Lowell, MA 01854
(978) 934-4000

8. PERFORMING ORGANIZATION REPORT NUMBER

9. SPONSORING / MONITORING AGENCY NAME(S) AND ADDRESS(ES)

DARPA, Mark Rosker
3701 N. Fairfax Drive.
Arlington, VA 22203-1714

AFOSR, Dr. Gernot Pomrenke
4015 Wilson Blvd.
Arlington, VA 22203

10. SPONSOR/MONITOR'S ACRONYM(S)
DARPA/AFOSR

11. SPONSOR/MONITOR'S REPORT NUMBER(S)

12. DISTRIBUTION / AVAILABILITY STATEMENT
Report approval for public release; Distribution Unlimited.

13. SUPPLEMENTARY NOTES

14. ABSTRACT Over the past four years the University of Massachusetts Photonics Center, the Center for Advanced Materials and the Submillimeterwave Technology Laboratory in partnership with AFRL/SNHC has been developing technology for producing low defect density substrates and high-quality epi-substrate interfaces for ABCS device applications as well as developing fabrication and device concepts for incorporation into quantum-cascade THz lasers. During the course of the project a number of new technologies were developed and demonstrated. A new Bridgeman-magnetic-stirring antimonide bulk growth method was developed and using the method 1) uniformly selinium n-type doped bulk GaSb crystals were grown, 2) Bulk InGaSb crystals were grown, and 3) GaAlSb bulk crystals were grown. In the areas of wafer polishing and epi-substrate interface control, novel gas cluster-ion-beam (GCIB) final polishing methods and bromine ion-beam assisted etching final polishing methods were developed that allow control of the epi-substrate interface when molecular beam epitaxy is employed for epigrowth. In the THz portion of the project novel THz photonic crystals were demonstrated and new phonon mediated THz quantum cascade laser design developed. The ABCS polishing work was moved toward commercialization through two joint collaborations with Galaxy Compound Semiconductors, Inc, a Phase I SBIR to develop bromine-based GaSb GCIB polishing (AFRL) and a Phasel/II project to develop novel final polishing techniques for GaSb and InSb wafers (DARPA). The THz work generated collaborations with Drs. T. Nelson and J.Ehret of WPAFB, Prof. Ram-Mohan of WPI/Quantum Semiconductor Algorithms, Inc. and Dr. Kurt Linden of Spire Corp.

15. SUBJECT TERMS
THz, GaSb, Gallium Antimonide, Dry Etching, Wafer Polishing, Photonic Crystal, THz Laser

16. SECURITY CLASSIFICATION OF:			17. LIMITATION OF ABSTRACT	18. NUMBER OF PAGES	19a. NAME OF RESPONSIBLE PERSON
a. REPORT	b. ABSTRACT	c. THIS PAGE	UL	127	19b. TELEPHONE NUMBER *(include area code)*

Table of Contents

List of Figures

List of Tables

Report Summary

This is the final report on the UMass Lowell Photonic Center's ABCS DARPA program in collaboration with AFRL/SNHC entitled " Low Defect Density Substrates and High-Quality Epi-Substrate Interfaces for ABCS Devices and Progress Toward Phonon-Mediated THz Lasers," contract no. F49620-01-1-0514, UMass Lowell Research Administration no. UMRF S13389280F00006. The report covers the period of 1 September 2001 to 30 June 2005.

a) Task Objectives

The UMass Lowell/SNHC team was given two main tasks in the DARPA ABCS program. These included 1) developing a novel bulk crystal growth technology for producing electrically uniform and defect free GaSb/InGaSb/AlGaSb ingots and 2) improving the state-of-the-art in GaSb surface preparation to allow epi-ready surfaces. Epi-ready surfaces are surfaces that can be directly inserted into a growth system with out any intermediate surface preparation. The UMass Lowell portion of the team was also charged with developing fabrication and design tools for developing phonon-mediated terahertz quantum cascade lasers (QCL).

b) Technical Problems

There were a number of major technical problems addressed. In the bulk growth area the problem is one of controlling the thermodynamics of the binary and alloy growth of these low melting point materials to produce stress (defect) free single crystals. In the wafer preparation area the problem is to develop a final polishing solution that allows the formation of easily thermally desorbible surface oxides while leaving a defect free smooth surface on which to commence epitaxial growth. In the development of THz laser sources the problems addressed included waveguiding, gain optimization, and device growth.

c) General Methodology

In the area of bulk crystal growth AFRL/SNHC developed a novel modified Bridgman reactor with magnetic stirring that employs 1) a submerged baffle to improve the uniformity of alloy composition along the ingot, 2) electromagnetic melt stirring to improve ingot radial uniformity, 3)excellent temperature profile control to reduce Hoop stress and 4) a submerged heater to avoid constitutional supercooling. In the area of final polishing/surface control UMass Lowell developed gas-cluster-ion-beam (GCIB) polishing, and 2) bromine-ion-beam-assisted polishing (Br-IBAE). A number of characterization tools were used to understand the polishing processes as they applied to MBE epigrowth. In order to improve and understand THz waveguide issues, UMass Lowell developed THz photonic crystal waveguides. In the THz modeling effort, Quantum Semiconductor Algorithms, Inc (UMass Lowell subcontractor) developed new code for implementing new phonon-mediated THz QCL designs. In order to produce high quality QCL material, the UMass Lowell Photonic Center installed a Veeco Gen II MBE machine (formally the Corning Lasertron machine) at the facility.

d) Technical Results

The modified Bridgeman with magnetic stirring approach for bulk antimonide grow was verified with boules of GaSb, AlGaSb and In GaSb grown using the technique. The GCIB final polishing technique was demonstrated to be able, depending on recipe, control the composition and thickness of the final surface oxide on GaSb wafers and allow epigrowth on the surface with only an in situ thermal desoption step. Br-IBAE was demonstrated as both a surface polishing technique as well as a technique to pattern the surface of the wafer and then overgrow the patterned regions. Prototype photonic crystal THz waveguides were demonstrated and new THz QCL designs developed. QCL material grown with the newly installed MBE system produced materials with excellent photoluminescence spectra.

e) Important Findings and Conclusions

This work shows that it is feasible to grow single crystal ingots of antimonide ternaries. The ability to grow AlGaSb for example may allow the development of semi-insulating near GaSb lattice mateched substrates for ABCS devices. The polishing portion of the work demonstrated that final dry etching techniques can be employed to produce epi-ready antimonide wafers. The smaller THz effort demonstrated the ability to develop photonic crystals at near THz frequencies and allowed the development of a more accurate model for determining THz QCL gain. The effort also allowed the Photonic Center to being growing QCL structures on a state-of-the-art MBE machine. Details of the most important findings and conclusions generated during the program are contained in the body of this report.

f) Implications for Further Research

The Photonic Center in partnership with Spire Corp. is in the process of preparing several THz QCL proposals based on the antimonides, where the gain may be at least three times stronger than the arsenide system. This effort will utilize all of the experience gained in the ABCS program. Furthermore the Photonics Center will continue to work on Arsenide based THz QCL's under a small Army contract.

g) Significant Hardware Development

Although no significant hardware was developed, the two SBIR Phase I efforts and SBIR Phase II effort spun out of this work produced a number of polished anitmonide substrates that were evaluated by a DOD laboratory and DOD contractors, for applications in DOD programs.

h) Special Comments

The Photonic Center appreciates DARPA and AFOSR's support of this project. Special thanks goes to Dr. Jag Shah, Dr. Mark Rosker and Dr. Gernot Pomrenke, the program managers for all their suggestions and help.

1. Introduction

This is the final report on the UMass Lowell Photonic Center's ABCS DARPA program in collaboration with AFRL/SNHC entitled " Low Defect Density Substrates and High-Quality Epi-Substrate Interfaces for ABCS Devices and Progress Toward Phonon-Mediated THz Lasers," contract no. F49620-01-1-0514, UMass Lowell Research Administration no. UMRF S13389280F00006. The report covers the period of 1 September 2001 to 30 June 2005.

This report was prepared by Prof. William Goodhue, Principal Investigator, with contributions by Prof. Changmo Sung, Center for Advanced Materials (CAM), Prof. James Whitten, CAM, Prof. Jerry Waldman, Submillimeterwave Technology Laboratory (STL), Dr. Lisa Allen, Galaxy Compound Semiconductors, Inc. (formally with Epion, Inc), Prof. Ramdas Ram-Mohan, Quantum Semiconductor Algorithms, Inc., Dr. David Bliss, AFRL/SNHC, Dr. Gerry Isler, Isler Associates, Dr. Thomas Nelson AFRL/SNDD, Dr. James Ehret AFRL/Materials Directorate, and a number of UMass Lowell students. The UMass Lowell graduate students who participated on the project and received a degree based on there work in the project included, Xianglin Li, M.S., Department of Chemical Engineering, Maria Ospina, M.S., Department of Chemical Engineering, Shiva Vangala, M.S. Physics Department, William Saggio, M.S. Physics Department, and Kannan Krishnaswami, Ph.D., Physics Department.

During the course of the project a number of new technologies were developed and demonstrated. A new Bridgeman-magnetic-stirring antimonide bulk growth method was developed and using the method 1) uniformly selinium n-type doped bulk GaSb crystals were grown, 2) Bulk InGaSb crystals were grown, and 3) GaAlSb bulk crystals were grown. In the areas of wafer polishing and epi-substrate interface control, novel gas cluster-ion-beam (GCIB) final polishing methods and bromine ion-beam assisted etching final polishing methods were developed that allow control of the epi-substrate interface when molecular beam epitaxy is employed for epigrowth. In the THz portion of the project novel THz photonic crystals were demonstrated and new phonon mediated THz quantum cascade laser design developed. The ABCS polishing work was moved toward commercialization through two joint collaborations with Galaxy Compound Semiconductors, Inc, a Phase I SBIR to develop bromine-based GaSb GCIB polishing (AFRL) and a PhaseI/II project to develop novel final polishing techniques for GaSb and InSb wafers (DARPA). The THz work generated collaborations with Drs. T. Nelson and Dr. James Ehret of WPAFB, Prof. Ram-Mohan of WPI/Quantum Semiconductor Algorithms, Inc. and Dr. Kurt Linden of Spire Corp.

2. Goals

High performance GaSb-based devices rely on a high degree of perfection in both the bulk substrate and surface crystal quality. The interface between the substrate and the epitaxial active layer is critical to performance issues such as transistor current gain, ability to pinch off, and turn-on voltage. Furthermore, since GaSb cannot be made semi-insulating, a bulk InGaAlSb quaternary with a larger band gap but near lattice match to

InGaAlAsSb epilayers would be a highly attractive approach to increasing the resistivity of the material. The ideal substrate would be a perfectly polished semi-insulating InGaAlSb wafer. However, in the absence of such substrates, many other solutions like wafer-bonding or metamorphic lattice-grading from semi-insulating GaAs or InP are being offered. All of these solutions require defect control at the substrate/epi interface to successfully fabricate high-quality devices. Killer defects can be caused by strain, surface damage, or particulates at the interface. **The bulk growth goal of the work was to establish a new a bulk growth technique that could not only grow high quality GaSb bouls but be extended to grow AlGaSb and InGaSb bulk alloy bouls and eventually InGaAlSb bulk alloy bouls.**

A major problem still facing the GaSb community is the lack of GaSb wafer quality control from the vendors. This very soft material with a variety of oxide states is very difficult to polish and at the same time form thermally desobable suface oxides for epitaxial overgrowth. **The polish goal of the work was to develop final polishing techniques that allowed improving the state-of-the-art in GaSb surface preparation to produce epi-ready surfaces.**

In the area of terahertz AlGaAs based laser technology major issues to be addressed include the development of suitable THz waveguides, gain optimization and device growth. **The goal of this smaller THz effort was to develop technologies for addressing the guide, gain and growth issues.**

3. Report Organization

This report is organized into three technical sections, the bulk crystal growth effort, the wafer polishing effort and the THz technologies effort. After the technical sections the personnel used in the effort are listed along with a listing of thesis manuscripts, conference papers/proceedings articles and journal articles. The report concludes with a summary and future work section and acknowledgements.

4. Crystal Growth of Semi-insulating III-V Alloy Crystals as Substrates for Terahertz Electronic Technology

4.1 Introduction

The first part of this report constitutes a general review of the principles and ideas that have gone into the development of our modified Bridgman growth method and a description of the growth hardware together with figures and some useful references. Part II covers the highlights of recent experimental results that may have implications for future work.

4.2 Part I

4.2.1 The Growth of High-Quality Uniform Crystals by the Vertical Bridgman Method

4.2.1.1 Growth of *Single* Crystals

For the growth of high-quality single crystals with the Bridgman method, or any bottom-seeded method, there are a number of principles that should be considered. First, in order to grow a boule consisting of one *single* crystal (rather than a polycrystalline ingot) a high-quality single crystal seed with the desired orientation of the crystal must be used. For each combination of material and growth rate a certain minimum vertical temperature gradient (not just inside the furnace heating elements but actually inside the melt) must also be maintained in order to avoid the nucleation of secondary grains at random orientations at or above the growth interface. For materials that do not melt congruently constitutional supercooling can occur, with dendrites shooting out from the growing crystal causing sudden and catastrophic polycrystallinity. This happens if the vertical gradient is not large enough to guarantee that the actual temperature of the melt just above the growth interface is above the specific liquidus temperature for the liquid alloy that exists at that position.

In addition the temperature stability during growth must be sufficiently high to prevent secondary nucleation but for many semiconducting materials, a more serious problem due to temperature excursions during growth may be that of twinning, since these defects are very likely growth accidents. The best stability limit that can be realized with modern PID temperature controllers is generally determined by the signal-to-noise level of the temperature sensor. For thermocouples the electrical noise level often limits the temperature stability to several tenths of a degree centigrade but for optical fiber sensors that limit can be more than an order of magnitude lower, i.e. hundredths and sometimes even thousandths of a degree.

Generally the shape of the growth interface must also be controlled to avert polycrystallinity. Secondary nucleation can occur at the periphery where the crystal-melt interface meets the container, and if the interface shape is concave these nuclei will tend

to grow inward toward the crystal center. Therefore the temperature profile of the growth furnace must be designed to accommodate any difference in the thermal conductivity of the solid crystal and the molten material from which it solidifies. A discussion of a method to generate more planar interface shapes during growth is included in the next section since a planar interface is also required to grow defect-free crystals.

4.2.1.2 Growth of Defect-Free Crystals

To grow a crystal with a high degree of perfection (with zero or low dislocation density) thermal stresses must be managed during growth and growth must be carried out under conditions that eliminate or at least reduce any growth accidents. Generally, in order to minimize thermal stresses the temperature profile that is imposed on the growth system must contain nearly planar horizontal isotherms especially in the region just below the growth interface where the grown crystal is at temperatures near the melting point. It is at this location where the yield stress of the material is lowest and therefore even moderate hoop stresses can easily lead to slip and dislocation multiplication. If the thermal conductivity of the crystal is less than that of the melt, as is most often the case for compound semiconducting materials, there will be a discontinuous change in the temperature gradient through the center of the axis of the crystal and melt at the growth interface. This change arises because the downward heat flux is either constant through the liquid-solid interface or it can in some cases actually be somewhat larger below the interface than above, due to the sensible heat of fusion generated by the freezing material at the interface. In either case the gradient is larger in the solid below the interface than in the liquid above. If the difference in thermal conductivity is large, it can result in a concave interface shape as indicated in Fig. 4.2. Since the downward heat flux through the growth ampoule wall material is essentially constant (because there is no abrupt change in its thermal conductivity) the temperature will vary more nearly linearly in the container walls, as shown. In addition, the average wall temperature will be only somewhat higher than the melt temperature if most of the heat flux is supplied from high up in the system rather than radially. The wall temperature then, just above the growth interface will be lower than the temperature of the melt at the same height. The net flow of heat out from the crystal center then will induce a concave isotherm shape and also a concave interface shape as shown. This effect is expected to be greater for crucibles made of materials with higher thermal conductivity.

One possible solution to this problem is to use a furnace temperature profile that closely matches the one through the center axis of the growing crystal so that there is a zero, or at least very small, radial temperature gradient in the crystal. A cylindrical furnace liner that fits closely around the growth ampoule and is made of a material with a moderate thermal conductivity can provide such a temperature profile if it is designed properly. In order to achieve this, the ratio of the wall thickness in the upper region which surrounds the melt to that in the lower region which surrounds the crystal should be equal to the ratio of the thermal conductivity of the liquid to that of the solid. In addition the temperature at the position of the wall thickness change must be maintained at the melting point during the growth process as indicated in Fig. 4.3. For the optimum effect on the interface shape, the growth ampoule should be made with thin walls from a material with low thermal conductivity. The total length of a crystal that can be grown with a liner as described is

limited to the length of the liner between the point where the wall thickness changes and where the water cooling begins: L_L. If a longer crystal were to be grown, the heat flow pattern would change (it would no longer be vertical) and the vertical temperature gradient in the melt would likely decrease. The maximum temperature gradient that can be induced in the melt is the gradient in the lower liner multiplied by the ratio of the thermal conductivity of the solid to that of the liquid (about 0.4 for GaSb). The maximum gradient in the lower section of the liner is the difference between the melting temperature of the material and the temperature of the liner where it is water cooled (maximum of 100^0 C) divided by the lower liner length: L_L.

One further idea to make the growth interface more nearly planar is that of a double-wall growth ampoule. The annular space between the two ampoules then creates a pseudo self-crucible since during growth the material in this region will contain both liquid and solid and therefore the temperature profile will exhibit the break in the temperature gradient at the interface. The use of a second ampoule (really an open-bottom tube) came about when magnetic stirring was induced with crossed magnetic and electric fields because the inside tube was made of graphite and served as the outer electrode for the radial current in the melt.

An earlier discussion of the great importance of interface shape and its relation to the ratio of the thermal conductivities of the solid and liquid phases is given by A. Horowitz [4.1] and by T. Jasinski and A. Witt [4.2]. In addition G. Muller [4.3] has written about planar growth interfaces: "A real alternative to the Czochralski process ....is the vertical Bridgman configuration... This method offers.....the best conditions for the growth of macroscopically and microscopically homogeneous crystals. Only buoyancy convection has to be controlled as no rotation and no free surface is necessary. .....In principle it is possible to reduce buoyancy so far that a purely diffusive heat and mass transfer can be approximately reached. This state is reached by a purely axial heat flux, which necessarily corresponds to a plane shape of the interface. This effect has a further advantage for III-V compounds because it reduces the thermal stress."

4.2.1.3 The Growth of Uniform Crystals

To grow a uniformly doped crystal or a ternary alloy crystal of uniform composition, a method to continuously restore the composition of the melt must be employed. In most cases the melt composition changes because the solid is of a different doping concentration or alloy composition than that of the liquid from which it freezes. One method that has been used successfully in the laboratory to maintain a constant melt composition makes use of a cylindrical baffle that is submerged in the Bridgman melt with a very small radial clearance between it and the growth ampoule walls [4.4]. The baffle effectively divides the Bridgman melt into two zones; a lower one from which the crystal grows and an upper one which is charged with material of the same composition as that desired in the crystal. As the crystal freezes from the molten material, at least one component of the melt is rejected into the lower melt, thus changing its composition. If the baffle is physically raised at the same rate that the crystal freezes, the lower melt volume is held constant. It is replenished with material from the upper zone. An

incremental volume of alloy with a particular composition freezes out and that same small volume of the same composition flows into the lower melt. In this way the average lower melt composition is held constant and therefore the average crystal composition will also be constant. The first requirement that must be met to obtain uniform crystals is that the two melts do not mix during growth. To effectively isolate the two melts the upward diffusive flux through the annular space around the baffle must be much smaller than the downward flow of molten material as the baffle is raised. Therefore the diffusion coefficient in the melt must be much less than the downward velocity of the melt flowing through the annulus, multiplied by the height of the cylindrical baffle. The equation is: $D<<<v\ H$, where D is the diffusion coefficient, H is the height of the submerged baffle and V is the velocity of the melt. For the growth of 50 mm diameter crystals at a rate of 2 mm per hour, $v = 0.2\Pi(2.5)^2/5\Pi(\delta r)3600$, where δr is the radial clearance between the baffle and the growth ampoule walls. D is generally of the order of $10^{-5}cm^2/sec$ for diffusion in liquids and therefore if the radial clearance is 0.5 mm and the baffle height is 4 cm the value of v H is 5.6×10^{-3} which is about two orders of magnitude greater than D.

A second condition that must be met to grow fully uniform crystals is that the lower melt composition must be made uniform, both in the radial and vertical directions. Since liquid from the upper melt zone flows down into the lower melt only in the annular space between the baffle and the growth ampoule walls, and there is little convection, the composition of the lower melt will tend to vary strongly from the periphery to the center. In addition, feeding from the top of the lower melt and the rejection of the component that is less strongly incorporated into the crystal at the bottom creates a vertical composition variation as well. One method to make the lower melt more nearly uniform is to stir it with a combination of a crossed electrical radial current in the melt with a vertical magnetic field. This produces a tangential force and can indeed stir a melt of GaSb with a steady magnetic field of only about 25 gauss and a radial current of only a few amps, for example. However this requires electrodes inside the melt and complicates the system considerably. Bourago et al [4.5] have modeled the effects of stirring by rotation of the submerged baffle. While this would indeed improve the melt uniformity, the difficulty of fabricating "bearing" assemblies that would not lead to twinning from vibration appears formidable. Still another way to induce stirring, however, is to simply impose an external rotating magnetic field on the melt. An electrically conducting melt then behaves somewhat as a synchronous motor rotor. We have demonstrated that a 6 pole 25 HP induction motor stator excited with 60 Hz current just below the Joule heating limit for the insulation on the copper coils (30 amperes in our case for the stator inside the growth chamber) appears to create a field sufficiently large to stir a 50 mm diameter GaSb melt. Thermocouples immersed inside protection tubes in the melt show reproducible changes due to the magnetic field produced by the stator and rotating at a rate of 1200 RPM.

If alloy crystals are grown, in which the composition of the solid that freezes is much different from that of the liquid from which it froze, yet another condition must be met to successfully employ the submerged baffle for uniform growth. The temperature of the liquid that is flowing down through the annulus must be greater than the liquidus temperature for the particular composition of the upper charge (which is also the

composition of the growing crystal). Therefore for any specific vertical temperature gradient that is imposed on the melt, a minimum height of the lower melt can be determined from the alloy phase diagram. For $Al_xGa_{1-x}Sb$ the minimum height becomes rather large even for a 25 degree C per cm gradient at moderately low Al content as shown in Fig. 4.4 because the liquidus and solidus boundaries are separated so far for this alloy system. For $In_xGa_{1-x}Sb$ on the other hand, the minimum lower melt height for the same gradient is more reasonable as shown in the figure. For the growth of crystals that are doped with donors or acceptors at concentrations typical for semiconducting materials (seldom greater than about one per cent in the melt) the liquidus and solidus temperatures are so close to each other that the lower zone could easily be as little as a fraction of a cm high for most temperature gradients that are useful. The Modified Bridgman growth technique that has been developed might also be useful for the $Cd_xZn_{1-x}Te$ alloy system. The required minimum lower zone height for this case is also shown in Fig. 4.4. It is quite small.

Another application of the modified Bridgman method might be the growth binary GaSb crystals with low anti-site defect concentration and therefore low hole concentration. Growth from Antimony-rich melts has been used for this purpose [4.6], however, the melt composition changes rapidly as the crystal freezes and rejects Antimony to make the melt still more Antimony rich thus limiting the size of the crystal to a very small fraction of the melt size. The modified Bridgman technique just described could be employed to grow GaSb from a solution containing about 82 atomic % Antimony in the lower zone at a growth temperature of about 610^0C with an upper charge of nominally stoichiometric GaSb. The temperature of the lower melt would need to rise to 710^0C at its top to melt the upper charge, but with a temperature gradient of 25^0C/cm in the melt the required lower zone height would be only 4 cm, which is reasonable. As shown in Fig. 4.5, extrapolation of the experimental data of reference 5 (which goes only as low as 680^0C) to temperatures as low as 610^0C indicates that crystals with residual acceptor concentration as low as $10^{15}cm^{-3}$ might possibly be achieved if grown from a solution containing about 80 atomic% antimony. The growth rate would ordinarily need to be very, very low but in this case stirring with the rotating magnetic field may allow a more reasonable rate.

Growth System Details, Crystal Growth Parameters and Procedure

In practice the submerged baffle also contains a heater in order to provide further control of the temperature profile. The system that has been designed and demonstrated at the Air Force Laboratory utilizes a baffle that consists of a fused silica housing that encloses a Molybdenum wire heater. The heater is wound into holes in a BN disc and the baffle is held stationary as the Bridgman growth ampoule is slowly lowered through the furnace containing the stainless steel liner with the abrupt change in wall thickness at the position of the growth interface. The "growth ampoule" actually consists of two concentric open-bottom tubes. The seed is of the same diameter as the crystal to be grown. The lower charge is a cast polycrystalline disc that sits atop the seed. The upper charge is a longer cylinder that has been cast with a small diameter graphite rod through its center. That rod is removed to make room for the vertical stem of the submerged heater/baffle. A diagram of the submerged heater is shown in Fig. 4.6.

The system is prepared for loading by securing a thermocouple to the BN hearth block with wire, checking the hearth heater resistance and tying Mo wires to opposite sides of the hearth for holding the growth ampoule down in good contact with the hearth as the ampoule is slowly lowered during growth. The two Mo wires are threaded up through the stainless steel liner and the hearth assembly is inserted into the liner. To load the system for growth the seed is placed into the inner tube and Dr. Becla has introduced a tight-fitting graphite disc about a cm high below the seed to further guarantee that no liquid spills out below. The lower charge is then added on top of the seed and a fine wire that is threaded around the bottom of the tube and graphite disc (a fine slot can be employed in the tube and disc to hold the wire in place during loading) is used to lower the tube into the stainless steel liner. That wire is then removed by pulling one end of it up and out of the system. The outer growth tube (ampoule) is then lowered into place. Next the upper charge is fitted onto the submerged heater/baffle stem and the whole assembly, including a thermocouple that runs down through the stem into a little well extending into the lower melt is lowered into the inner growth tube. Thermocouples are inserted into protection tubes and placed in the annular space between the two tubes as the prime indicators of the liquid-solid interface position during the initial heat up. Three equally spaced fused silica rods or tubes are placed in three slots on the inside of the stainless steel liner to center the growth ampoule and provide better temperature symmetry. The two Mo wires coming up from the hearth are then tied to a stainless steel ring on top of the growth ampoule and the position of the hearth is adjusted so that the top of the seed is at or just above the point at which the wall thickness of the stainless steel liner changes. A small diameter stainless steel rod is attached to the submerged heater/baffle assembly and secured to the growth chamber top so that it can not move up or down. After evacuating and backfilling the chamber with a mixture of A and H_2 gas, power is supplied to the main heater surrounding the liner and to the hearth and submerged heater. When the temperature of the liner (at the critical point where the wall thickness increases) reaches the desired liquidus temperature, the hearth should first be raised several mms to melt back part of the seed and to force out any remaining gas below the submerged heater. Finally to grow the crystal, the temperature of the hearth must be ramped down at a rate equal to the product of the hearth lowering speed (growth rate) and the temperature gradient in the lower part of the stainless steel liner.

4.2.2 References

4.1 A. Horowitz, In Praise of the Confined Vertical Growth of Semiconductors, Mat. Res. Bull., V 21, P1123, 1986

4.2 T. Jasinski and A. F. Witt, J. Crystal Growth, V 71, p295, 1985

4.3 G. Muller, Crystal Growth from the Melt, Springer Verlag Berlin, 1988, pps 126-127

4.4 A. G. Ostragorsky, J. Crystal Growth, V104, P 233, 1987

4.5 N. G. Bourago, A. I. Fedyushkin and V. I. Polezhaev, Adv. In Space RRRes., V24, p1245, 1999

4.6 F. J. Reid, R. D. Baxter and S. E. Miller, J. Electrochem. Soc. V113, p713, 1966

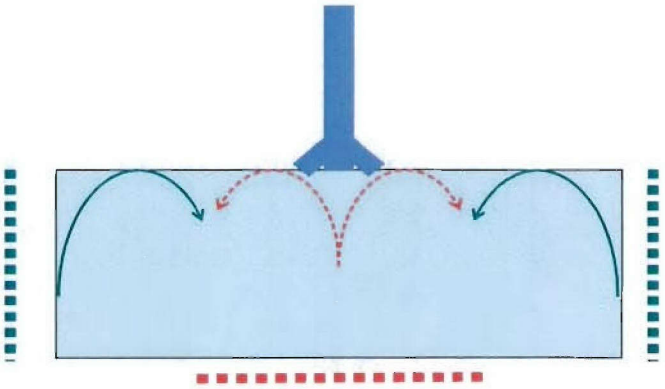

Figure 4.1. Schematic cross sectional diagram showing possible effect of bottom heating on fluid flow in Czochralski melt.

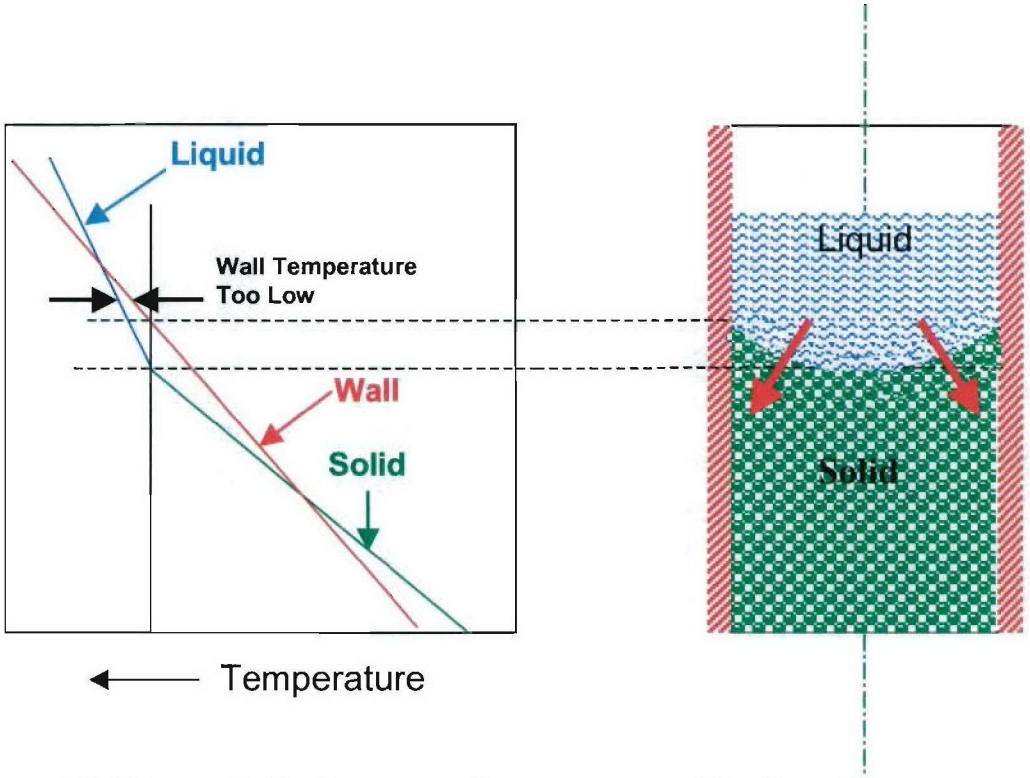

Figure 4.2. Diagram indicating expected temperature profiles through center of crystal and melt and through growth ampoule wall when thermal conductivity of solid is less than that of liquid. Temperature of growth ampoule wall is lower than that of center axis; therefore heat flow is outward and interface is concave.

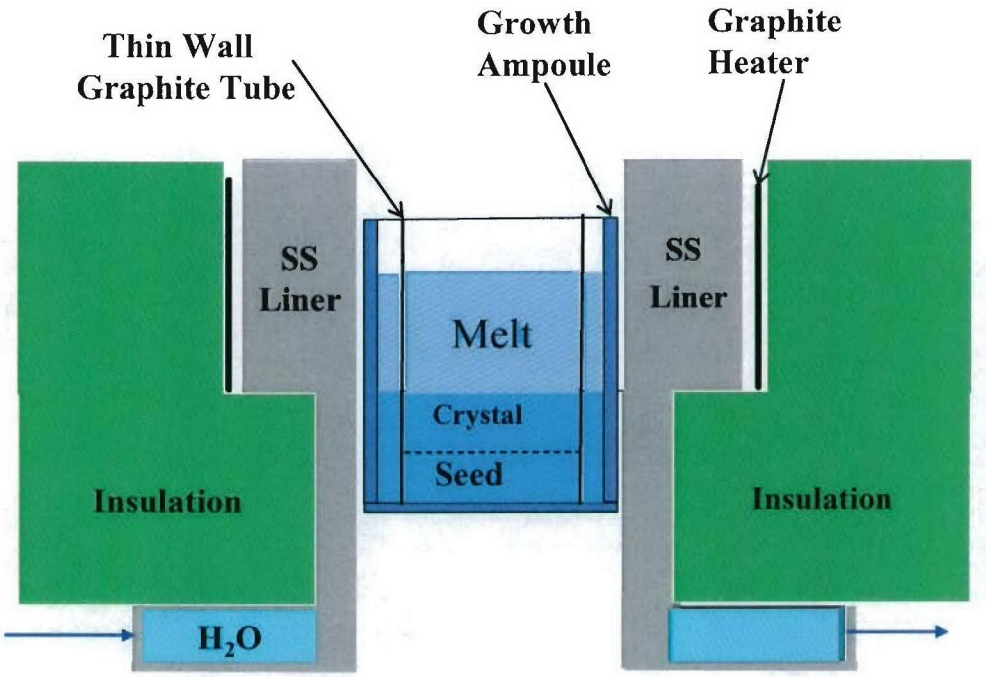

Figure 4.3. Schematic cross sectional diagram showing stainless steel liner that provides discontinuity in temperature gradient at growth interface as described in text.

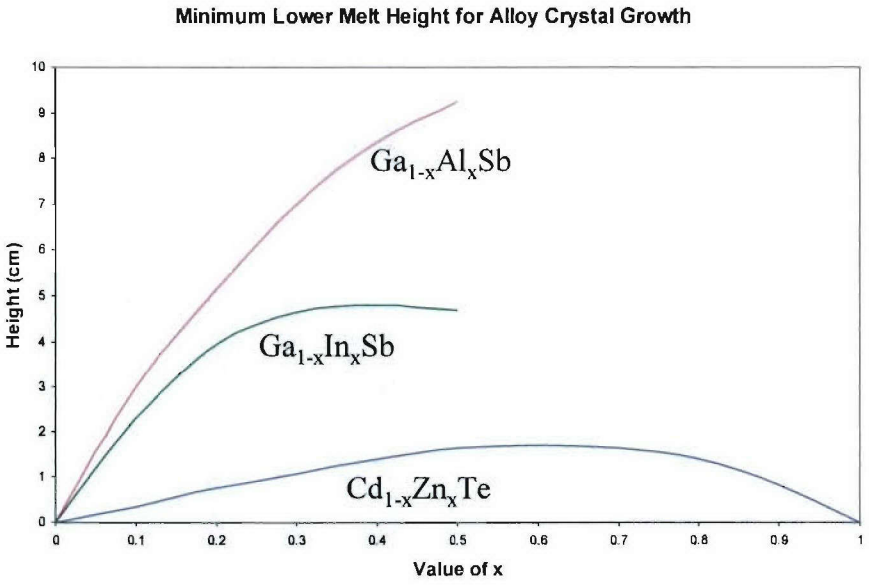

Figure 4.4. Minimum lower melt zone height for Bridgman growth with submerged baffle for three alloy systems calculated for 25^0C/cm temperature gradient in melt.

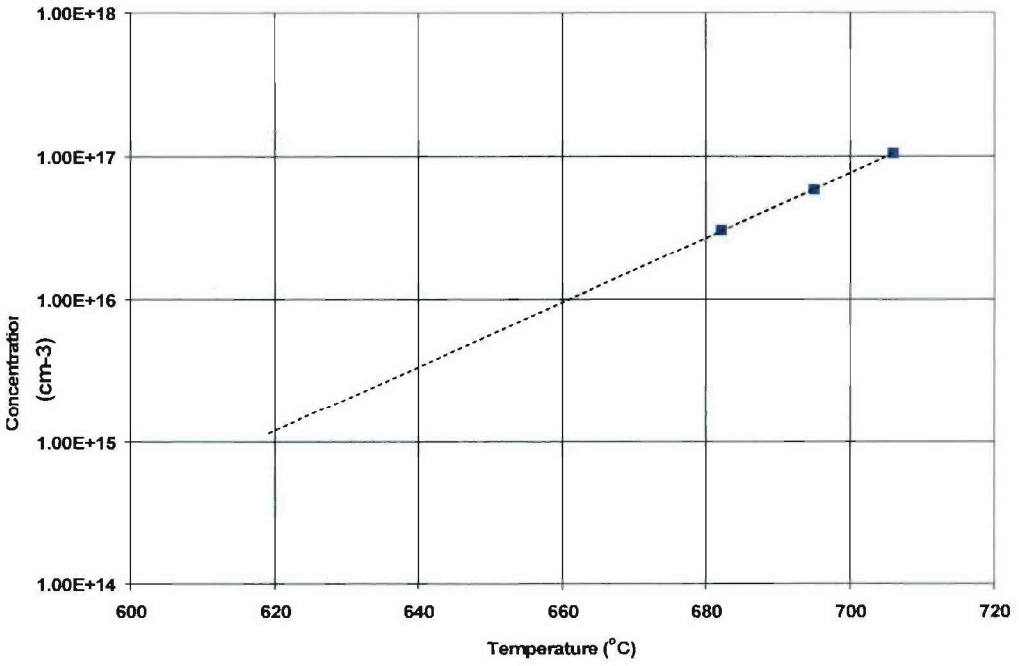

Figure 4.5. Hole concentration of nominally undoped GaSb for growth from Sb-rich solutions versus liquidus temperature. Data points are from reference 5 and dashed line is linear extrapolation to lower liquidus temperatures.

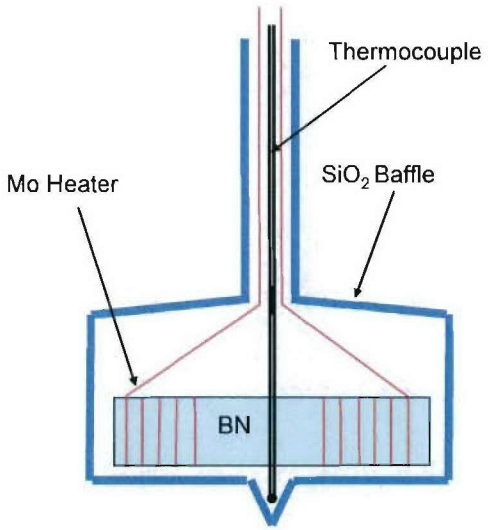

Figure 4.6. Schematic cross sectional diagram of submerged heater/ baffle assembly.

4.3 Part II

4.3.1 Summary of Recent Experimental Results with Implications for Future Work

4.3.1.1 Introduction

During this period a fiber optic thermometer was installed into our modified Bridgman crystal growth chamber in order to more precisely control the temperature during growth. Since the installation required the removal from the chamber of the synchronous motor stator, the opportunity was taken to measure the strength of the rotating magnetic field as a function of radial distance from the center axis. Another experiment to determine the ratio of the thermal conductivity of liquid material to that of solid by measuring a temperature profile through a column of liquid and solid was made except this time not for GaSb but for a GaInSb alloy. Finally, after reinstalling the stator into the chamber, a growth run was made with the lower charge consisting of a very Sb-rich melt, and the upper charge of compounded GaSb.

4.3.1.2 Crystal Growth System Modification and Characterization

In order to reduce the probability of twinning during growth, any temperature variations should be minimized. In an attempt to more precisely control the temperature, a fiber optic thermometer system was installed into our Bridgman system. In a first experiment utilizing an ordinary fused silica rod in the high temperature region near the Molybdenum heating element, the temperature at that point could easily be controlled to several hundredths of a degree Centigrade.

During the time that the motor stator was outside the growth chamber, a magnetometer was borrowed from The National Magnet Laboratory and a measurement of the strength of the rotating field was made as a function of radial distance from the center axis inside the open stator. The results are shown in Fig. 4.7 1 for the stator excited with the 60Hertz 30 ampere maximum allowable current that is employed during crystal growth. The measured field is very nearly zero at the center axis and increases with the square of the distance from the center as shown in the figure. The behavior of the magnetic field strength suggests that more vigorous stirring might be obtained by using a larger diameter growth crucible. The first thing that could easily be tried would be the elimination of the inner tube in the crucible (currently used to induce a pseudo "self crucible" to promote more nearly planar growth interfaces). Eliminating the inner tube would increase the crystal radius to 3 cm where the measured field is about 6.3 gauss as opposed to about 4.4 gauss at the 2.5 cm inside radius of the present tube.

The next experiment was one to further study the difference between the thermal conductivity of the melt and that of the solid, but in this case for a GaInSb alloy rather than for the binary compound, GaSb. A charge of reacted $Ga_{0.9}In_{0.1}Sb$ was placed into a fused silica ampoule and loaded into the Bridgman system. A schematic cross-sectional

diagram of the ampoule is shown in Fig. 4.8. A small diameter tube was fused into the ampoule at the bottom as shown in order to accommodate a thermocouple to measure the vertical temperature profile through the center axis of the ampoule when it was heated to contain solid alloy at the bottom and liquid at the top. The measured temperature gradient in the lower solid portion of the system is about 37^0C/cm while for the upper liquid section it is only about 11.5^0C/cm. If the temperature measurements are realistic, this must be due to a large ratio of the thermal conductivity of the melt to that of the solid; namely 37/11.5 or about 3.5. For pure GaSb, we have earlier found this ratio to be 2.5. Therefore it would be still more difficult to maintain a planar interface during growth for the alloy than for the binary compound.

The larger difference in the ratio of the liquid to solid thermal conductivity for the alloy than for the binary compound is probably due to different modes of heat transfer in the liquid and the solid. Since the liquid is a good electrical conductor, heat transfer probably occurs via free electrons as in a metal. Under these circumstances, the thermal conductivity probably would not change much with alloy composition. On the other hand in the solid, heat is transported primarily by the lattice and it is well known that "impurities", even isotopes of the same element can scatter phonons and increase thermal resistance significantly. For alloys the scattering is even greater. Adachi (1) has calculated the thermal resistance of $Ga_{1-x}In_xSb$ alloys and it has been converted to thermal conductivity and is shown in Fig. 4.9. The expected alloy composition profile for "normally frozen" material through the crucible axis containing the solid and liquid alloy is shown in Figure 4.10. It has been numerically calculated by using the expression; $k=x_{(liquid)}*0.277 + 0.123$ for the segregation coefficient of InSb, and assuming a perfectly uniform melt composition. Just below the liquid-solid interface the solid alloy for a "normal freeze" would contain about 3 mole % InSb. The thermal conductivity of this particular alloy, from Adachi's calculated curve in Figure 3, is reduced by a factor of 1.3 from that of GaSb. Therefore if the liquid thermal conductivity did not change with alloy composition, the ratio of the temperature gradient in the solid to that in the melt for this particular alloy would be expected to be 1.3 times larger than it is for pure GaSb or, 2.5 * 1.3 = 3.3, on the basis of that calculation. Our measurements showed a ratio of 3.5, in good agreement with that expected for a constant liquid conductivity. More measurements will be made for alloy compositions nearer to 50 mole % where the thermal conductivity of the solid is near its minimum value for the GaInSb alloy system. Notice that at compositions near the center of the range, the calculated thermal conductivity of the solid is reduced by about a factor of 9 from that of pure GaSb.

The consequences of the very large difference between the thermal conductivity of the liquid and solid for semiconductor alloy crystal growth have not been given much attention in the crystal growth literature. Researchers sometimes measure a temperature profile is in an empty vertical Bridgman tube furnace and a then suspend a loaded growth ampoule from the top and insert it into the furnace, with the expectation that a similar temperature profile will be found in the growing crystal and in the melt above it. In actual fact the vertical temperature profile through the center axis of the growing crystal and of the melt above it can be very, very different from the one measured in the empty furnace. First, since the liquid is generally quite a good thermal conductor, in order to achieve a

steep temperature gradient in the melt (where it is *required* to avoid constitutional supercooling) a significant vertical heat flow is necessary. This heat must be removed at the bottom of the ampoule, preferably in a manner that will allow fairly planar isotherms, at least near the growth interface. Secondly and probably more importantly, since the heat flow is constant or even *increases* below the interface due to the sensible heat of fusion especially if the growth rate is high) the temperature profile through the center axis of the melt and crystal will exhibit a large discontinuity in the temperature gradient right at the interface. High growth rates can not be used for alloy growth and therefore the heat flux is generally very nearly constant down through the center axis of the melt and crystal. Nonetheless, our data imply that the ratio of the gradient in the solid to that in the melt may easily be a factor of 15 or more for the growth of a crystal of $Ga_{0.75}$ $In_{0.25}Sb$ for instance. So to maintain a 10^0C/cm gradient in the melt, which may or may not be sufficiently large to prevent constitutional supercooling, the solid gradient would need to be 150^0C/cm! Non planar isotherms under these conditions are probably be very likely and very troublesome. Some means to shape the temperature profile in the Bridgman furnace itself definitely appears to be required if nearly planar isotherms are to be obtained. Use of the furnace liner with the heavy wall in the melt region and thinner wall in the region where the crystal freezes is the way that we have chosen to address this problem, but we have not yet provided for the *extremely* large ratios of liquid to solid conductivities that are expected for alloys containing more than a few per cent InSb.

4.3.1.3 Growth of GaSb from Sb-rich Charge

In 1966 Reid, Baxter and Miller had already reported that GaSb grown from Sb-rich solutions contained fewer acceptor defects than material grown from stoichiometric or Ga-rich charges. They achieved a reduction of hole concentration from the 1 to 2 x $10^{17}cm^{-3}$ levels typically observed for growth from stoichiometric charges to about 4 x $10^{16}cm^{-3}$ by growing from a solution containing 72 atomic% Sb. Their results were reported only for the first-to-freeze portions of the ingots that they grew since the Sb content of the growth solution increases rapidly with the fraction of the material that has frozen. Their work suggested that we might use the modified Bridgman method that has been developed here for alloy growth, to grow GaSb with low carrier concentration. Such material would be useful as substrates for thin film devices that require IR transparency of the substrate.

A growth run was made by loading a pre-cast charge of $Ga_{0.3}Sb_{0.7}$ above a polycrystalline "seed" and just below the submerged heater. The upper charge consisted of pure GaSb. The "seed" was 23mm tall. The Sb-rich charge about 4 cm high in order to guarantee that the upper charge would be melted in the region of the submerged heater. After heating the system until the thermocouple in the annular space between the growth ampoule and graphite tube located vertically just at the top of the "seed' reached 640^0C. Growth was then initiated by lowering the ampoule at a rate of 0.25 mm/hour. The ingot was sliced longitudinally and viewed in transmission with an IR camera and optical transmission and Hall coefficient measurements were made.

It is clear in the transmission image shown in Fig. 4.11 that the seed melted back somewhat (to about 17 mm in height from the original 23 mm) before the ingot began to grow. The abrupt dip in the interface is not understood but may represent an area of the lower cast charge that contained nearly pure Sb which dissolved the seed deeply at that point during the heating stage. The remaining seed that did not melt is clearly more opaque than is the grown crystal and indeed the hall measurement indicates that the hole concentration in the grown ingot is about $9 \times 10^{16} cm^{-3}$ compared to about $1.5 \times 10^{17} cm^{-3}$ for the seed, which was grown from a stoichiometric melt.. The results for the absorption coefficients calculated from the optical transmission experiment are shown in Fig. 4.12. The absorption coefficients found for the grown crystal are not a full factor of two less than that for the seed, but they are definitely smaller corresponding to the reduced hole concentration.

While the first experiment with growth from an Sb-rich charge did not produce an order of magnitude reduction in carrier concentration it did result in a crack-free ingot that is more transparent in the IR than are crystals frozen from stoichiometric melts. The slow growth rate of 0.25 mm/hour combined with the use of the rotating magnetic field likely reduced any boundary layer build up of more Sb. From the published phase diagram the probable Sb content of the lower zone should have reached approximately 80 atomic% with the interface temperature at 640^0C. For this composition, the data of Reid, Baxter and Miller extrapolate to about 2 or $3 \times 10^{16} cm^{-3}$ rather than the value of $9 \times 10^{16} cm^{-3}$ that we obtained. Their rapid growth rates may have increased the Sb content in the boundary layer nearly to the 87 atomic% Sb that corresponds to the eutectic point composition. In the near future we will carry out another GaSb growth run with an Sb-rich charge. The lower charge will be a cast ingot of the eutectic composition. The temperature at the interface point will be raised to about 5^0C above the eutectic temperature, i.e. to 595^0C. A small portion of the seed should then dissolve into the charge until the Sb content is reduced to that corresponding to the liquidus composition for 595^0C. Slow growth from this solution should provide a crystal with the lowest hole concentration that can be achieved by growth from the melt. If that hole concentration is reasonably easy to reproduce, it should be possible to closely compensate the residual acceptors with Se donors and to maintain a uniform net *electron* concentration throughout the entire crystal with the use of the submerged heater. Reducing the residual hole concentration is necessary because any variations in the difference between the donor and acceptor concentrations at the $10^{16} cm^{-3}$ level are expected to be a factor of 10 less than at the $10^{17} cm^{-3}$ level. The material should be n-type to minimize the free carrier IR absorption because at longer wavelengths the absorption cross section for electrons is less than that for holes.

4.3.2 References

4.7. S. Adachi, J. Appl. Phys.**54** (4), 1844 (1983)

4.8. F. J. Reid, R. D. Baxter, and S. E. Miller, J. Electrochem. Soc. **133,** 713 (1966)

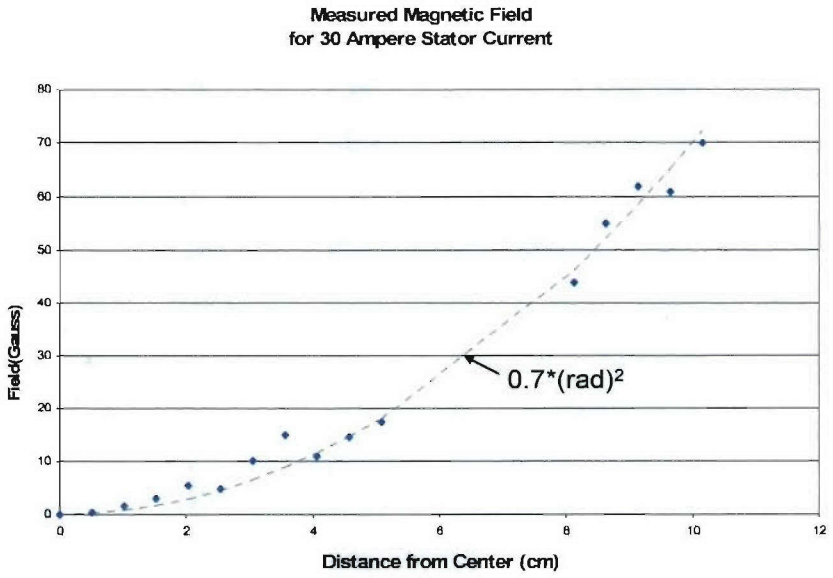

Figure 4.7. Measured magnetic field strength versus radial distance from center axis of empty motor stator for 30 ampere excitation at 30 Hz.

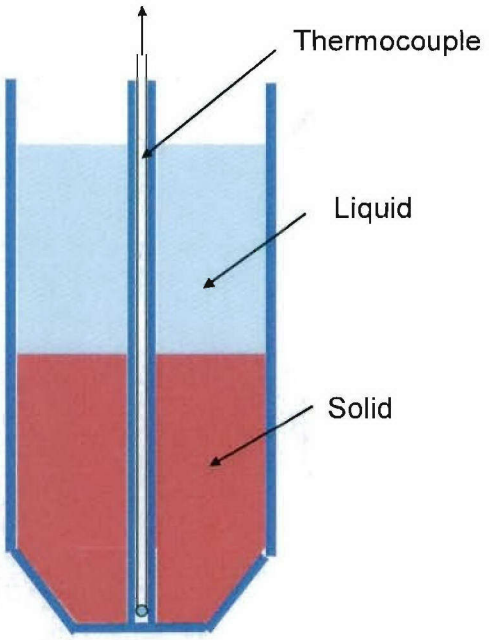

Figure 4.8. Fused silica ampoule used for measurement of vertical temperature profile through liquid and solid GaInSb alloy.

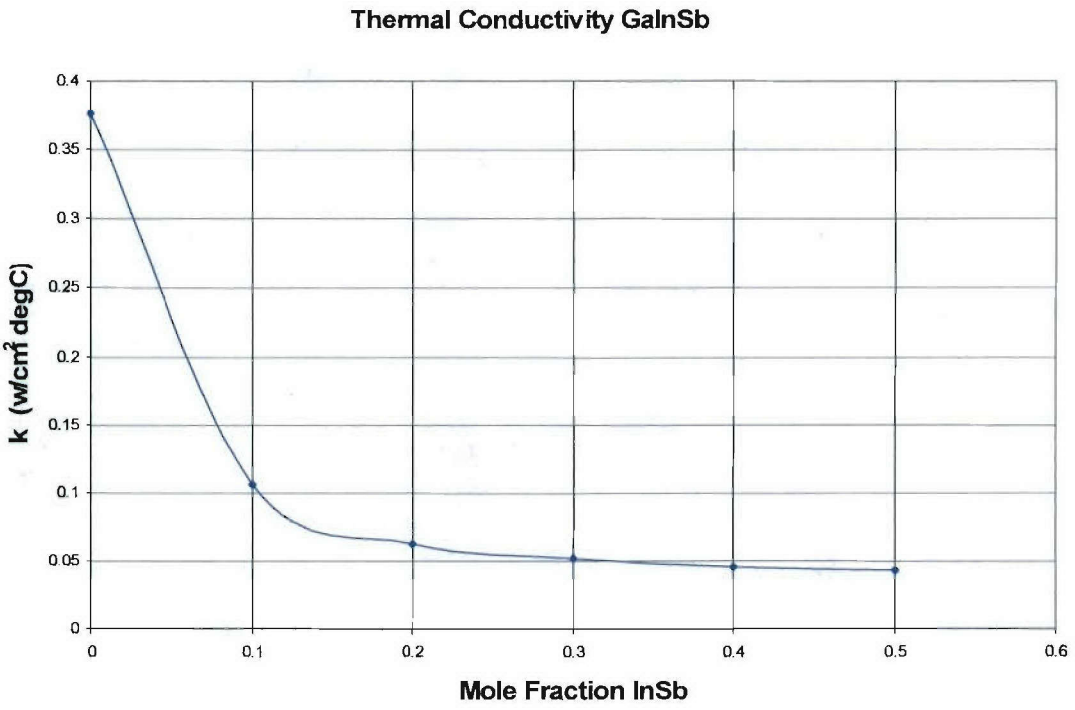

Figure 4.9. Value of thermal conductivity versus composition for GaInSb alloys calculated by Adachi.

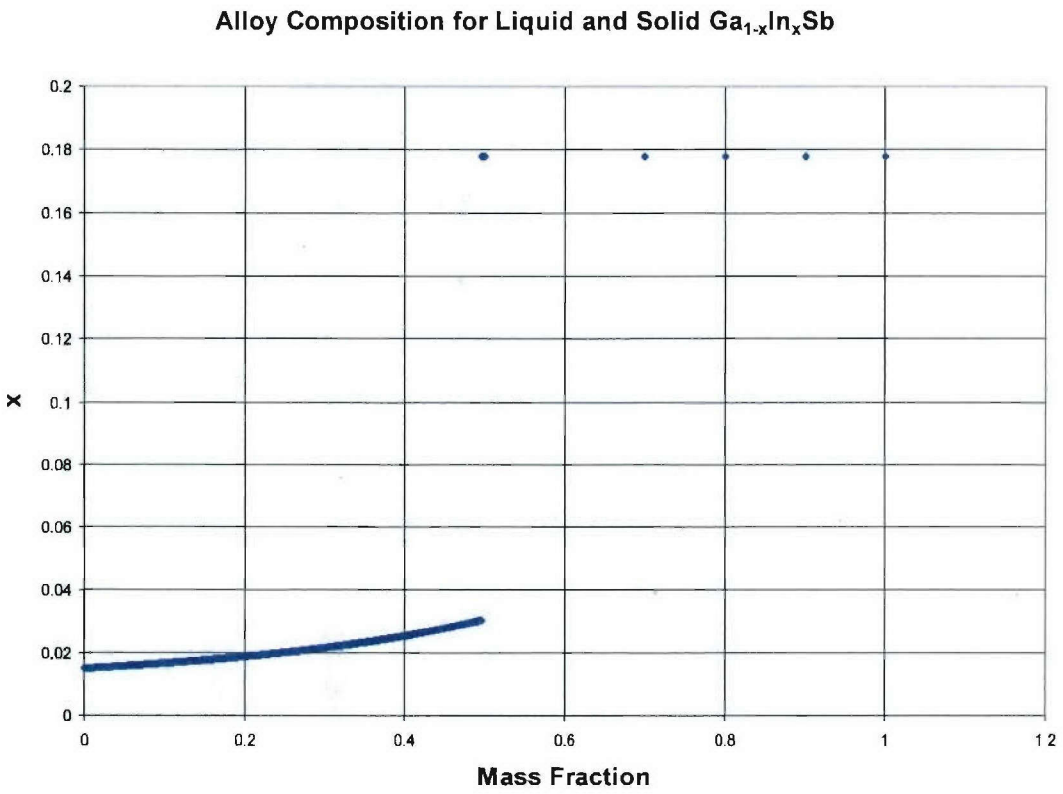

Figure 4.10. Expected alloy composition versus fraction frozen for $Ga_{0.9}In_{0.1}Sb$ starting charge for "nomal freezing".

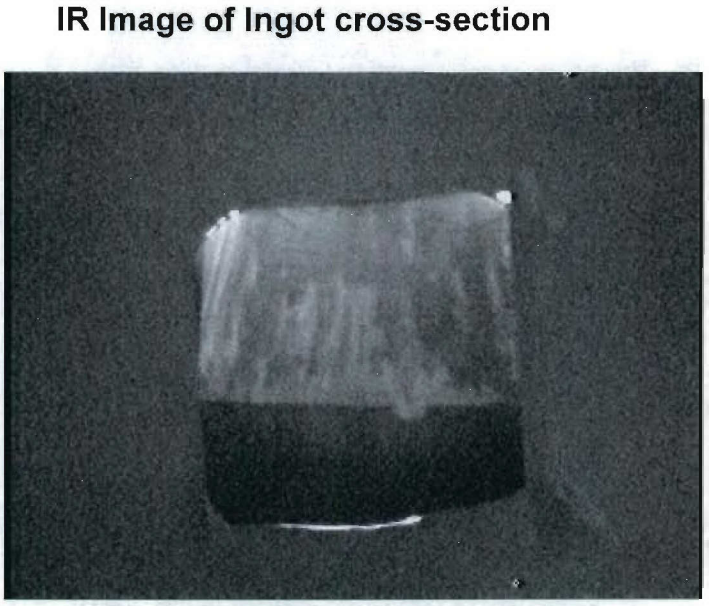

Figure 4.11. Infrared transmission image of crystal grown from Sb-rich melt. Dark bottom is seed region which absorbs more radiation due to more free holes.

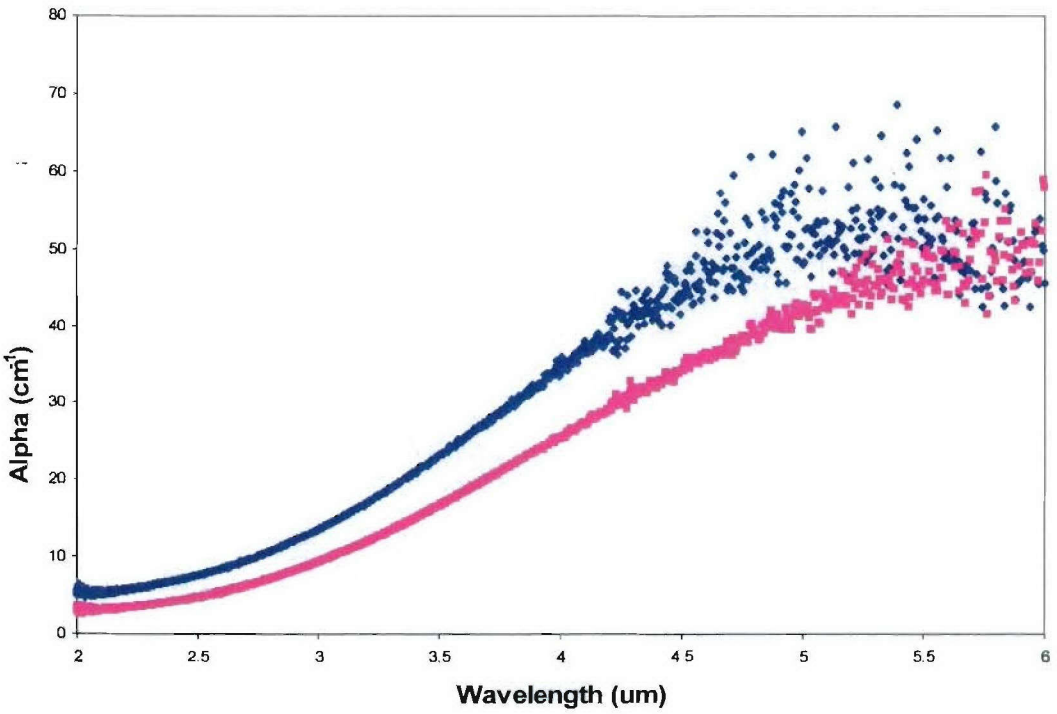

Figure 4.12. Optical absorption spectra calculated from optical transmission for seed (upper curve) and grown crystal (lower curve) of ingot shown in Fig. 4.11.

5. Wafer Polishing Effort

5.1 Overview

GaSb is a relatively soft material, making polishing difficult. Although a number of damage removal steps are used to eliminate saw, grind and intermediate polish damage, wafers can still retain a relatively high-density of scratches, pits and other near-surface defects after the final Chemical-Mechanical Polishing (CMP) step. Furthermore, the surface oxide left by the CMP polish may not be ideal for epitaxial growth over the surface in that the oxide may not fully desorb at sufficiently low temperatures in the growth reactor. **The polishing goal of this work was to develop a final GaSb and GaSb alloy polishing technique to improve the state-of-the-art in GaSb surface preparation to the point of producing epi-ready wafers.** Epi-ready wafers are wafers that can be directly inserted into a growth system with out any intermediate surface preparation.

The following technical achievements related to the polishing goal were made during the project:

1) New models and methods were developed for measuring figures of merit for the quality of a polished surface and to determine the nature of the oxide layer on the surface with respect to epitaxial growth by molecular beam epitaxy (MBE). These new tools included a surface oxide model, a fractile analysis method, and a thermal X-Ray Photoelectron Spectrometry (TXPS) analysis method.

2) Gas Cluster ion beam (GCIB) processing was demonstrated as a viable final polishing technique for producing epi-ready GaSb wafers.

3) Bromine-ion-beam-assisted etching was demonstrated top be a viable techinique for ething structures in GaSb surfaces and then overgrowing the structures.

5.2 Models and Methods

5.2.1 Surface Oxide Model

This discussion developes the models used to determine the chemical reactions taking place on the wafer surface during gas cluster ion beam (GCIB) processing. The chemical models for the Br-IBAE and the Cl-ICP processes are similar and will not be discussed. The GCIB subsections found here were based on Kannan Krishnaswami's Ph.D. thesis [5.1].

GCIB is a recent technology that modifies sample surfaces on the order of a nanometer [5.2-5.7]. In a GCIB surface smoothing mode, a relatively rough surface may be smoothed to typically 1/3 of the original RMS or better. In a practical GCIB etch mode, a surface may be etched up to several hundred nanometers. The process uses atomic or molecular clusters with a single electrical charge rather than conventional monomers to

modify a surface. Each cluster averages ~1500 atoms. For example, an acceleration of 10,000kV on a 1,000 atom cluster with a single charge yields an energy per atom of 10eV upon impact on a material surface. This single atom impact energy, one of 1,000 within the cluster, is sufficient to break several lattice bonds of GaSb or other target material during a GCIB smoothing process. The lower charge to mass ratio of GCIB ions as compared with conventional monomers significantly reduces the kinetic energy and momentum of the individual atoms as they strike the wafer surface. On the other hand, the impact of the large clusters also creates locally very-short pulses of increased temperature and pressure that have the potential to anneal out sub-surface polish damage. The effect is to smooth the surface while eliminating further substrate disorder [5.2,5.3,5.6].

In addition to lateral sputtering to improve surface roughness and sub-surface damage annealing, the incorporation of a reactive gas in the GCIB cluster source enhances the sputtering rate due to chemical reactions with the surface atoms. Upon impact on the surface, the reactive components are initially absorbed on the surface, followed by the formation of volatile compounds that are either ejected or evaporated from the surface. One of the consequences of incorporating reactive components in the gas source is the increase in etch rate and a reduction in the threshold energy required for physical sputtering. For chemically active semiconductors, the inclusion of oxygen as a gas source results in the formation of a thin surface oxide layer under moderate vacuum conditions [5.4]. Here, the surface elements from the damaged layer, due to GCIB processing are readily consumed by the oxygen gas clusters into the formation of an amorphous surface oxide layer. For instance, in the case of GaSb surfaces, the O_2 molecules compete to form volatile compounds with the liberated Ga- and Sb-atoms which are pumped out of the system

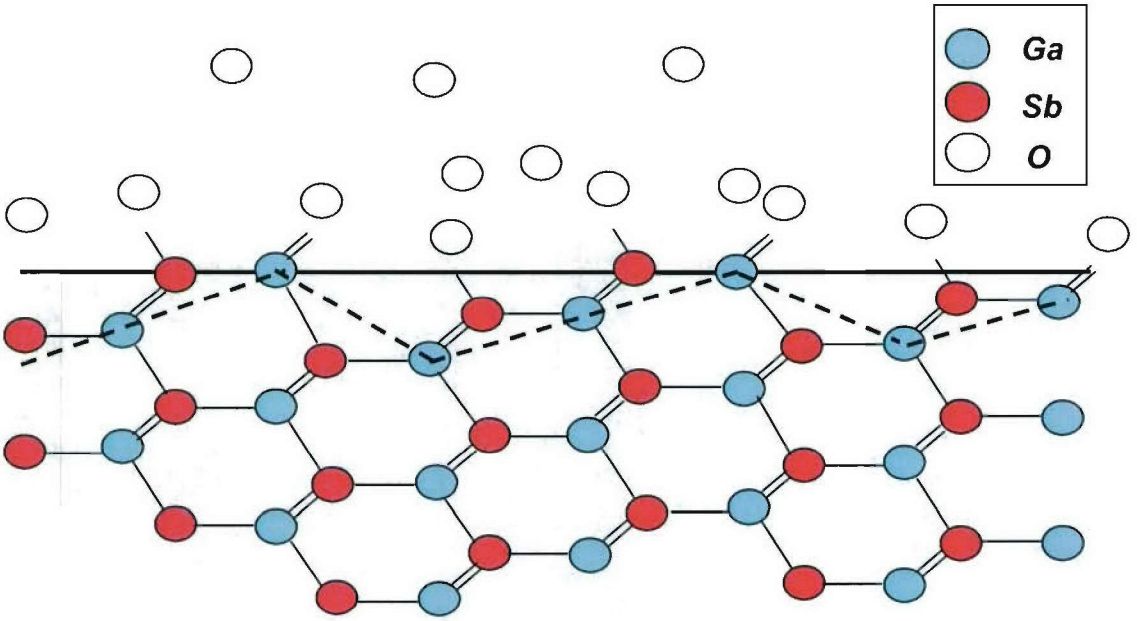

Figure 5.1. Side view of a GaSb crystal surface with the presence of single and double dangling bond sites where O_2 molecules attach themselves. The dashed line is indicative of the 100 terrace structure while the solid line is indicative of the surface.

while also simultaneously attaching themselves to the single and double dangling bonds along the surface [5.8] as shown in Fig. 5.1. The availability of the dangling bonds depends on the crystallographic nature of the step-terrace formation on a 100 surface. Here, the O_2 molecules often bind themselves to one or more Ga and/or Sb sites forming an amorphous oxide with binding energies similar to Ga_2O_3, Sb_2O_3, and Sb_2O_5.
The compounds found in the oxide layer strongly depend on the change in the Gibbs free energy (ΔG) of the reaction expressed as:

$$\Delta G = \Delta H - T\Delta S \tag{5.1}$$

where ΔH is the change in enthalpy, ΔS is the change in entropy, and T is the temperature of the reaction [5.9]. The ΔG values, often termed as the heat of formation, for several compounds have been routinely reported in the literature and compiled in data books [5.10]. In general, for exogenic reactions ($\Delta G < 0$) the probability of forming a specific compound increases with decreasing values of ΔG, though the possibility of its formation is still dependent on the valency, bond-sharing and energies of the individual atoms.

For instance, when energetic O_2 clusters impinge on a GaSb substrate, they break the lattice bonds of the surface atoms forming several intermediate compounds (GaO, Ga_2O, Sb_2O_4, etc.) before forming energetically favorable compounds. XPS signatures of O_2-GCIB processed GaSb surfaces have shown binding energies corresponding to Ga_2O_3, Sb_2O_3, and Sb_2O_5, besides identifying the GaSb host material. Thus, it is possible that the oxide layer formed on GaSb substrates due to O_2-GCIB processing follows the reaction:

$$2GaSb^{(s)} + 3O_2^{(g)} \longrightarrow Ga_2O_3^{(s)} + Sb_2O_3^{(s)} \tag{5.2}$$

along with the simultaneous conversion of Sb_2O_3 to the more stable Sb_2O_5 with the reaction

$$Sb_2O_3^{(s)} + O_2^{(g)} \longrightarrow Sb_2O_5^{(s)} \tag{5.3}$$

resulting in a mixed oxide layer that contains both Ga- and Sb-oxides distributed through its thickness. The superscripts indicate either the solid (s) or gaseous (g) phase of the compound. It is also possible that the reaction takes the form

$$2GaSb^{(s)} + 5O_2^{(g)} \longrightarrow Ga_2O_3^{(s)} + Sb_2O_5^{(s)} \tag{5.4}$$

thus, by-passing the intermediate Sb_2O_3 formation.

The Gibbs free energy for the above reactions (ΔG_r) are calculated using:

$$\Delta G_r = \sum \Delta G_{products} - \sum \Delta G_{reactants}\,. \tag{5.5}$$

where the published ΔG values, shown in Table 5.1, are inserted [5.10,5.11]. For example, using Equation 5.5 the Gibbs free energy for the chemical reaction described in Equation 2 was calculated as follows:

$$\Delta G_r = (-998.3) + (-712.4) - 2(-38.9) - 3(0) = -1632.9\ kJmol^{-1}\,. \tag{5.6}$$

Similarly conversion of Sb_2O_3 to the more stable Sb_2O_5 (based on Equation 3) resulted in a value of ΔG_r = -117kJmol^{-1}, while the reaction of Equation 5.4 results in ΔG_r = -1749.9kJmol^{-1}. These values are only an indication that all three reactions are thermodynamically viable. But, in order to ascertain the presence of an individual compound using XPS, it is standard practice to crush the sample into a powdered form such that energy states due to crystallographic orientation are eliminated, yielding only compositional information.

Table 5.1. Gibbs free energy (ΔG) values for GaSb, its oxides, and its fluorides. Note: C_g is graphite.

Compound	Δ G (kJ/mol)
GaSb (s)	-38.9
O_2 (g)	0
Ga_2O_3 (s)	-998.3
Sb_2O_3 (s)	-712.4
Sb_2O_5 (s)	-829.4
GaF_3 (s)	-1085.3
SbF_3 (s)	-915.5*
GaF (g)	-251.9*
GaO (g)	253.5
Ga_2O (s)	-356*
C_g (s)	671.3
CF_4 (g)	-933.6*
CO_2 (g)	-394.4

**Enthalpy values are quated and used as ΔG values were unavailable for these compounds. Enthalpy value are usually comparable to ΔG*

The introduction of a halogen component (such as Fluorine) into the gas clusters, to enhance the etch rate, significantly alters the composition of the surface oxide. One of the GCIB processes used during this research incorporated 5% of CF_4 in the gas clusters mixed in with O_2 gas. XPS spectra of the surface layer due to CF_4/O_2-GCIB processing showed the presence of Ga- and Sb-oxides, similar to the O_2-GICB process, as well as the presence of Ga- and Sb-fluorides (GaF_3 and SbF_3) on the surface of the superficial layer. Thus we can postulate that the superficial layer on the GaSb substrate due to CF_4/O_2-GCIB follows the chemical reactions described in Equations 5.2, 5.3, and 5.4 for O_2 molecules in addition to a reaction with CF_4 molecules, described by:

$$2GaSb^{(s)} + 3CF_4^{(g)} \longrightarrow 2GaF_3^{(s)} + 2SbF_3^{(s)} + 3C_g^{(s)} \tag{5.7}$$

where C_g is the formation of graphite. The Gibbs free energy for Equation 5.7 was calculated to be $\Delta G_r = 543.8 \text{kJmol}^{-1}$, rendering it unlikely to occur. Hence, it is also possible that during the CF_4/O_2-GCIB processing that the interaction of O_2 molecules with GaSb to form Ga_2O_3, Sb_2O_3, and Sb_2O_5 occur first which in turn react with the CF_4 gas. These reactions can be written as

$$2Ga_2O_3^{(s)} + 3CF_4^{(g)} \longrightarrow 4GaF_3^{(s)} + 3CO_2^{(g)} \qquad (\Delta G_r = -547 \text{kJmol}^{-1}) \tag{5.8}$$

$$2Sb_2O_3^{(s)} + 3CF_4^{(g)} \longrightarrow 4SbF_3^{(s)} + 3CO_2^{(g)} \qquad (\Delta G_r = -620 \text{kJmol}^{-1}) \tag{5.9}$$

Here, it should be noted that the chemical reactions described by Equation 5.2 – 5.4, and 5.7 – 5.9 are not occurring independent of each other. Hence, besides the formation of Ga- and Sb-oxides mentioned earlier, cross-products (oxy-fluorides) and volatile gases (GaF and SbF) may also be formed, though they were not detected in the XPS measurement.

In general, the composition of the surface oxide layer is entirely dependent on the gas species used in the gas clusters. However, since the GCIB process has the ability to sputter off

the surface, in a multi-step (with choice of either/or both energy and gas) GCIB process the composition of the oxide layer is highly dependent on the final step. For instance, if a CF_4/O_2-GCIB process step is followed by a O_2-GCIB step, then the composition of the surface layer will be mostly dominated by the second step as it sputters through the surface layer formed by the first step. Hence, depending on the initial surface condition of a GaSb substrate the process chemistry can be modified to include gas components, such as CF_4 and SF_6 that are known etchants for III-V compounds in the semiconductor industry, along with O_2 gas to remove the CMP produced oxide and damage layers followed by a second process that contains O_2 gas only to smooth the surface and form the oxide layer. Thus, with the choice of appropriate gases in combination with an oxygen gas source, the composition of the surface layer on a GaSb substrate can be suitably altered for applications to MBE and the formation of ohmic contacts, thereby presenting the possibility of engineering the surface oxide layers.

5.2.2 Oxide/Substrate Interface Characterization Method

The roughness of a semiconductor substrate is always measured on the surface of the oxide. This measurement is not necessarily an indication of the roughness of the oxide/substrate interface. The measured surface roughness is usually the product of two factors: a) roughness due to the substrate smoothing process and b) the oxide produced by the final polish.

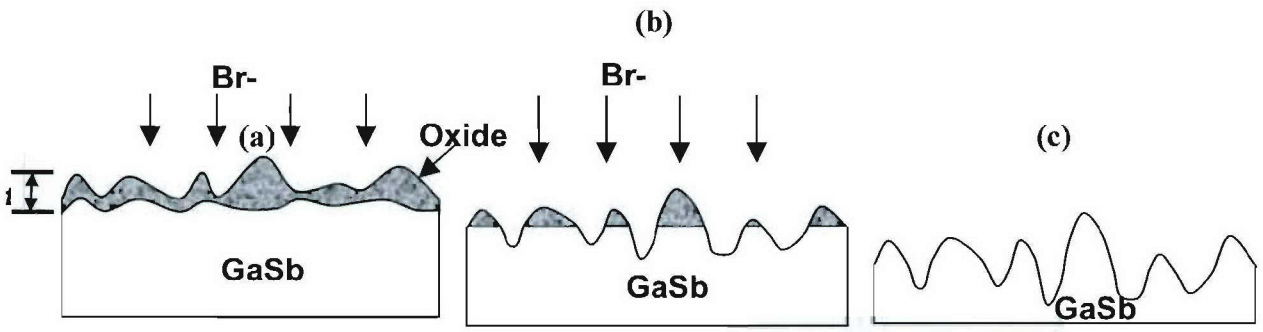

Figure 5.2. Schematic of: a) variations on the oxide surface, b) micro-masking due to Br-IBAE processing, and c) amplification in surface roughness as a result of Br-IBAE processing.

From earlier Br-IBAE etch experiments performed on GaSb, it was shown that the oxides have a significantly slower etch rate than the semiconductor crystal [5.12]. Effectively, as the oxide etches away, thickness variations in the surface oxide result in the creation of micro-masks at the substrate/oxide interface, shown in Fig. 5.2 a) and b) respectively. Here, due to the difference in etch rates of the crystal and oxide, thickness variations in the surface oxide are amplified as a result of Br-IBAE etching, shown in Fig. 5.3 c), resulting in an increased roughness of the post-etched surface. Note: Once the oxide is completely etched off, there is no further change in roughness with continued etching.

Qualitatively, the oxide formation on the surface of a final polished GaSb surface may take one or more combinations of the surface oxides sketched in Fig. 5.3. In Fig. 5.3 a) the top surface of the oxide is flat but the oxide/substrate surface is rough; In Fig 5.3 b) the top surface is rough and the interface is flat and in Fig 5.3 c) the top surface is flat and the interface is flat. Once the oxide is thermally desorbed in an MBE system the true surface of the wafer is revealed as depicted in sketches Fig 5.3 d)-f).

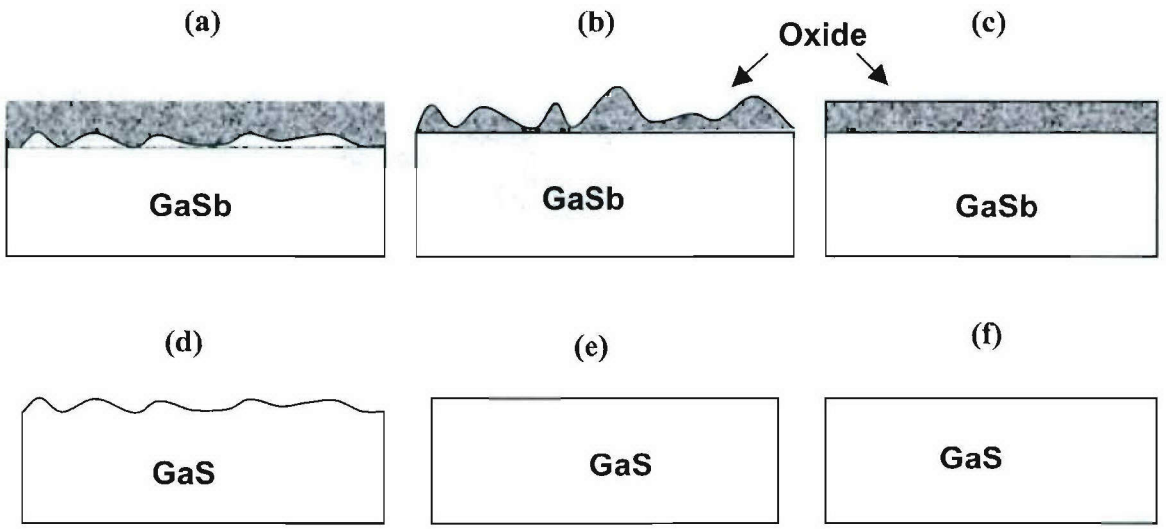

Figure 5.3. Sketches a)-c) show possible crossesction of an oxide layer on a GaSb wafer. Sketches d) – f) show what the wafer surface may look like after the oxide is thermally desorbed in an MBE system.

Fortunately, Br-IBAE etching of the wafer surface followed by AFM analysis can qualitatively reveal the GaSb oxide/wafer interface since after etching, the Br-IBAE replacement oxide has been found in this work to be very thin at 6 to 8 nm and conformal. Thus Br-IBAE together with AFM has been used in this work to qualitatively characterize the oxides/substrate interface as a function of the final polish. Obviously, polishing processes that produce both flat oxides surfaces and smooth Br-IBAE etched surfaces, Fig 5.3 c) are preferred over those that produce the results of Fig. 5.3 a).

5.2.3 Fractile Analysis Method

AFM images were analyzed from: 1) CMP finished wafers; 2) GCIB-finished, Br-IBAE finished, and ICP-finished wafers; and 3) epilayers grown on CMP, GCIB, Br-IBAE, and ICP finished surfaces. Due to the non-linear scan of the probe, a second order flattening routine was applied to correct the images. Surface analysis yielded roughness parameters, i.e. the average roughness $R_a = \langle h-\langle h\rangle\rangle$, the root mean square roughness $R_{rms} = [\langle(h-\langle h\rangle)^2\rangle]^{1/2}$, and the maximum height range $Z = h_{max} - h_{min}$, where h is the measured height relative to an arbitrary plane. The pixelated height data in an $N \times N$ array form was exported to a Mathcad routine for further statistical analysis using Fenner's approach [5.13], described in the following paragraphs.

Let $h_i = h(x_i)$ and $h_j = h(x_j)$ be the height vectors of N elements consisting of pixels from the i^{th} row and j^{th} column of the acquired AFM image. Hence the topography is represented as individual height cross-sections for the individual line scans of the AFM. Hence, the individual pixel locations are (x_i,y_j) where $i,j = 0,1,\ldots N-1$ defining a square image. If the length of the image is L then each pixel is assumed to have dimensions N/L along its edges.

If we define the term $S_l = (L/N)/l$ for $l = 0,1\ldots M$ and $M < N-1$ to be an incremental length, often called the lag length, describing the displacement from any location (x_i,y_j) on the surface, then the autocorrelation function for height is given by

$$C_A(l) = \frac{1}{2N(N-l)C_0}\left[\left\langle \sum_0^{N-l-1} h(x_i)h(x_i+s_l)\right\rangle_y + \left\langle \sum_o^{N-l-1} h(y_j)h(y_j+s_l)\right\rangle_x\right] \tag{5.10}$$

where $C_0 = C_A(l=0) = (R_{rms})^2$ and where the angel brackets imply averaging over all N line scans in the x and y directions. Similarly, the height-height difference correlation is given by

$$C_D(l) = \left\{\frac{1}{2N(N-l)C_0}\left[\left\langle \sum_0^{N-l-1}\left[h(x_i)-h(x_i+s_l)\right]^2\right\rangle_y + \left\langle \sum_o^{N-l-1}\left[h(y_j)-h(y_j+s_l)\right]^2\right\rangle_x\right]\right\}^{1/2} \tag{5.11}$$

where the root mean square form has been adopted [5.14,5.15].

PSD plots are another method to analyze image heights. Here, if $k_n = n$ and $k_m = m$ for $n,m = 0,1,\ldots N-1$ are the spatial frequencies of the fast Fourier transform (FFT) between the real and reciprocal space provides the PSD described by

$$P(n) = \frac{2L'}{N}\left[\left\langle \sum_{i=1}^{N/2} FFT(h(x_i))^2\right\rangle_y + \left\langle \sum_{i=1}^{N/2} FFT(h(y_i))^2\right\rangle_x\right] \tag{5.12}$$

where the averaging results in equivalent indices n and m for P. For convenience we have chosen $L' = L/1\mu m$ such that P has the units of nm^2. The Equations 5.10 – 5.12 provide summations that are one dimensional evaluations of cross-sectional profiles averaged over both x and y directions. Here, isotropic surfaces with random in-plane orientations of features are assumed.

All three functions C_A, C_D, and P have particular characteristics when the surface exhibits random fractal properties. If H is the Hurst parameter and d the Euclidean dimensions, then $D = d + 1 - H$ is the fractal dimension. Here, $H = 1$ implies Gaussian roughness while smaller values ($D>d$) describe jagged and highly rough surfaces. The autocorrelation functions for random fractal surfaces is best described by a two part exponential given by

$$C_{Af}(s) = (1-p)C_0 \exp\left[-(s/\varsigma_1)^{2H}\right] + pC_0 \exp\left[-(s/\varsigma_2)^{2H}\right] \quad (5.13)$$

where $C_0 = (R_{rms})^2$, ζ_1 and ζ_2 are correlation lengths for the two parts, s is the lag length, and p

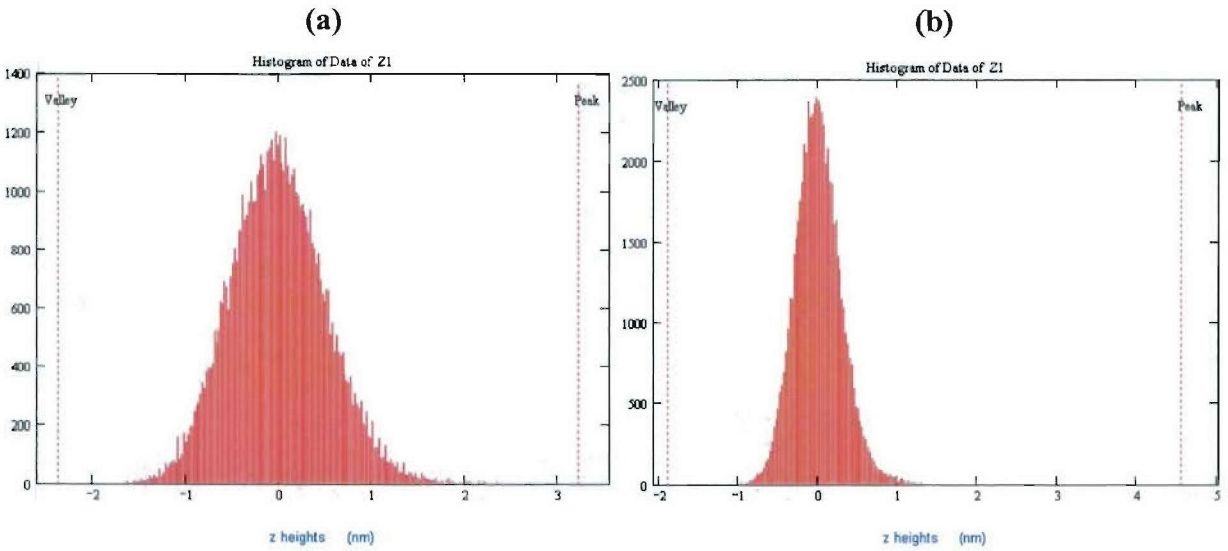

Figure 5.4. Histogram of height distributions on: a) CMP and b) GCIB processed GaSb surface with marked peak and valley extremities.

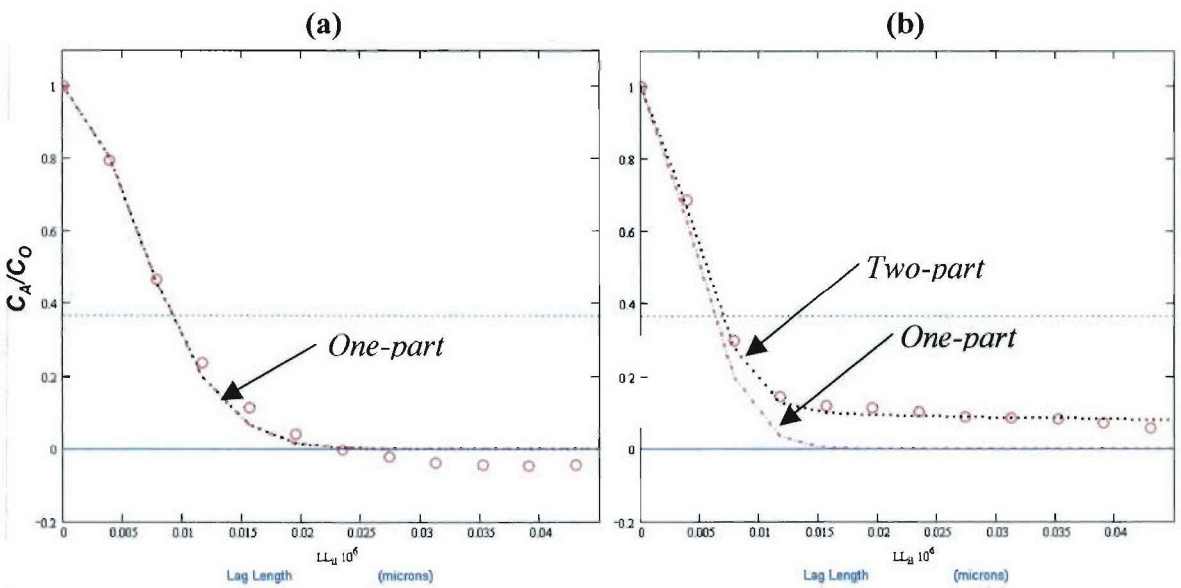

Figure 5.5. Autocorrelation function for the AFM data (circles) fit with the two-part random-Gaussian correlation decay model (dashed line) for: a) CMP and b) GCIB-S009 processed GaSb surfaces.

is the fraction of the second part, though it is not necessary to use the second part when a good fit is obtained with the first. The height-difference correlation for a fractal surface is given by

$$C_{Df}(s) = 2C_0\left[1 - \exp(-s/\varsigma)^H\right] \tag{5.14}$$

where the exponent H is used instead of $2H$ for consistency with the *rms* form of C_D. Since the value of $C_D(s)$ asymptotically approaches a constant value for large lag lengths, it is convenient to define a normalized height-correlation $C_D(s)' = C_D(s)/LimC_D(s)$ where the value of $s \rightarrow \infty$.

PSDs plotted as *Log(P) vs. Log(k)* for fractal surfaces show a power law behavior, i.e. $P(k) \sim k^{-\alpha}$, where α is the slope. However, real surfaces with fractal characteristics are bandwidth limited to white noise above and below. Hence, an expression for $P(k)$ in the form of a Lorentzian function, sometimes referred to as k-correlation model, is best described as

$$P_f(k) \sim \frac{A}{\left[1 + (Bk)^2\right]^{1+H}} + P_f(\infty) \tag{5.15}$$

where the second term in the equation is added to account for background white noise.

Using the statistical expressions described above, the procedure for obtaining the roughness exponents and correlation lengths from AFM images was the following:

1. AFM images of pre-and post-GCIB processed surfaces were first analyzed statistically using Equations 5.10 – 5.12 to obtain the distributions for $C_A(l)$, $C_D(l)$ and $P(n)$.
2. The phenomenological expressions for fractal surfaces, equations 5.13 – 5.15, were fitted to the distributions of Equations 5.10 – 5.12 by adjusting the free parameters within $C_{Af}(s)$, $C_{Df}(s)$, and $P_f(k)$ to obtain the roughness exponents and correlation lengths.

A Mathcad code (developed by Fenner) used for statistically analyzing surface roughness was used in this work. The following paragraphs outline the fitting process used to obtain the roughness exponents and correlation lengths for representative pre- and post-GCIB surfaces. Note: the two surfaces were analyzed in two separate code executions.

AFM images in data form, consisting of a 256 x 256 array of height distributions, were exported out of the Digital Instruments Nanoscope III and used as raw input to the Mathcad code along with its Z-range. In order to check the validity of the input data, the code first generates a histogram of the of the height distributions and calculates R_a, R_{rms}, and Z values that can be correlated to the AFM image. Figure 5.4 a) and b) shows a histogram of typical height distributions on a CMP and GCIB-S009 processed GaSb surfaces respectively, with marked peak and valley extremities for 1 x 1μm^2 images.

Upon data validation, the code proceeds to generate the matrices for auto-correlation (also known as height-height correlation or auto-covariance of surface heights) using Equation 5.10. Simultaneously, a plot for the two-part random-Gaussian correlation-decay model for random fractals, described in Equation 5.13, is plotted. Initially only the correlation length (ς) and the Hurst exponent (H) in Equation 5.10 were varied to fit Equation 5.13. In addition, the parameter p can also be varied to obtain a better fit. Figure 5.5 a) and (b) show the normalized auto-correlation data for CMP and GCIB processed GaSb surfaces respectively. CMP surface exhibited $H_a = 0.9$ and $\varsigma_a = 9$nm, where the subscript a represents data fitting to the auto-correlation function. The GCIB surface, on the other hand, required a 10% fraction for the second part of the random-Gaussian correlation-decay to obtain a good fit, exhibiting $H_a = 0.9$ and $\varsigma_a = 6$nm. Thus, this process provides the roughness exponent, correlation length, and fraction for the two-part fit to the correlation-decay model.

Next, height-difference correlation function was evaluated using Equation 5.11 for the AFM images and fitted to the fractal model of Equation 5.14 by varying H_d and ζ_d. Here the subscript d denotes the difference-correlation data. It was also necessary to choose an asymptotic value for long lag lengths which only changed the amplitude of the fit but not the characteristic or shape of difference-correlation model. Figure 5.6 a) and (b) show the height difference correlation functions for the CMP and GCIB-S-009 surfaces respectively. The CMP surface exhibited $H_d = 1$ and $\zeta_d = 6.5$nm while the GCIB-S009 surface showed $H_d = 1$ and $\zeta_d =$ 5nm with an asymptotic lag length adjustment value of 0.42.

Next, the one dimensional isotropic power spectrum density (1D-PSD) function for the surface roughness of the AFM images were plotted using Equation 5.12 and subsequently fitted to k-correlation model for fractals, described by Equation 5.15, by varying the fractal roughness exponent (H_p), and cross-over point (B_p). The power-law slope (ζ_p) for this function

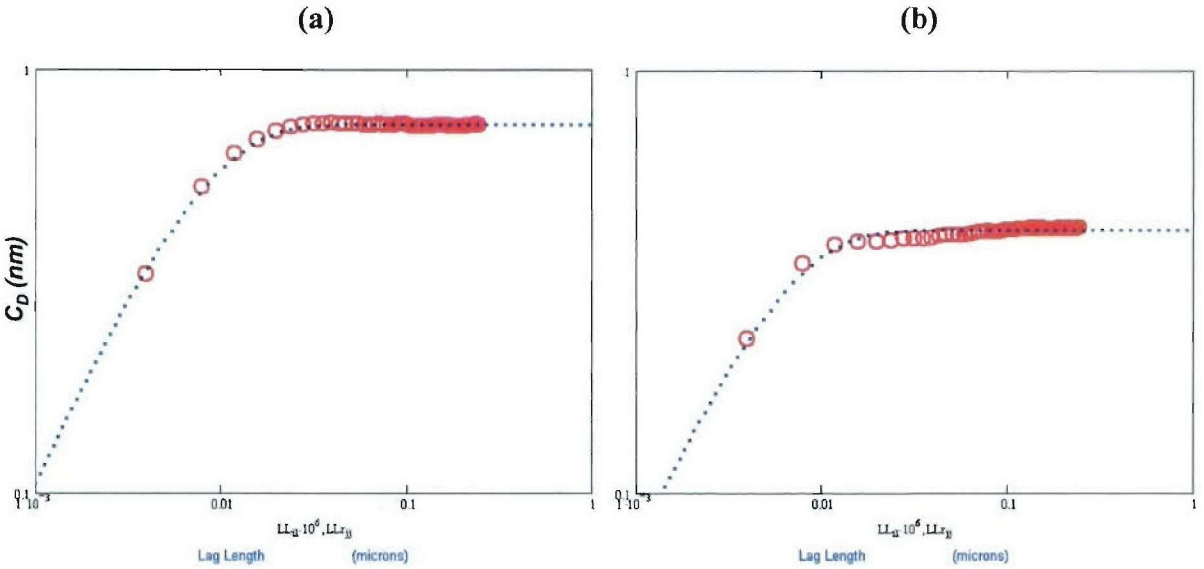

Figure 5.6. Height-difference correlation functions of the AFM data (circles) fitted to the phenomenological equation (dashed line) for: a) CMP and b) GCIB-S009 processed GaSb surfaces.

is also calculated. Here, the subscript p indicates a fit to the 1D-PSD model. Figure 5.7 a) and (b) show the 1-D PSD curves and k-correlation fits for CMP and GCIB-S009 surfaces respectively. The CMP surface showed $H_p = 1$, $B_p = 30$nm, and $\zeta_p = -3$, while the GCIB-S009 surface showed $H_p = 1$, $B_p = 22$nm, and $\zeta_p = -3$.

Finally, a single line scan of the AFM data showing typical height cross-sections is shown in Figure 5.8 a) and (b) for the CMP and GCIB-S009 processed surfaces respectively. The cross-sectional plots of the post-GCIB processed surfaces clearly show a reduction in the Z range as compared to pre-GCIB, or CMP, processed surfaces.

The data from Figs. 5.5 – 5.7 clearly showed a reduction in amplitude for C_A, C_D, and P due to GCIB processing, i.e. the surface is smoothed over a range of about three orders of magnitude in spatial dimensions for 1 x 1μm^2 image sizes. Fractal analysis of the 10 x 10 μm^2 images exhibited mostly white noise. The parameters H and ζ can be independently obtained by statistically analyzing each of the three correlation functions and hence all three methods

are provided. However, when fitting the data for each of the three methods described above, particular attention was paid towards maintaining self-consistency for values of H and ζ across Equations 5.13 – 5.15. For data exhibiting smaller values of the parameter H the functions $C_{Df}(s)$ and $P_f(k)$ were relatively insensitive to the choice of the parameter H as compared to surfaces exhibiting large values of H. Also, when the value of H is small, fitting $C_{Af}(s)$ for small values of s provides a better fit and thus is more reliable. The overall fit quality on these surfaces resulted in an uncertainty of ± 0.1 for the H parameter and an uncertainty of 10% or ± 2nm, whichever is larger, for the correlation lengths (ζ).

For example, using the analytical method described above, pre- and post-GCIB processed GaSb surfaces were analyzed, to obtain the fractal (roughness) parameters of the individual surfaces using auto-correlation, height-difference correlation, and spectral density plots. Statistical analysis was performed for representative AFM images for 1 x 1μm^2 and 10 x 10μm^2 sizes. The results of pre- and post-GCIB surfaces for various preparation techniques [11] is provided in Table 5.2. The 10 x10μm^2 images did not show any fractal properties yielding mostly white noise. (Note: pre-GCIB surfaces are the CMP processed surfaces.) Due to the kinetics and chemically active nature of the GCIB process, along with the various process parameters involved, it is essential for purposes of consistency that only results of similarly processed samples be compared.

AFM measurements clearly indicated that the first batch of CMP finished GaSb surfaces (CMP-1) were rougher than the second batch (CMP-2) of surfaces used in this work. Also, it could be seen that within the batch itself, the roughness parameters (R_{rms}, R_a, and Z) of CMP-2 were far more consistent that those of CMP-1.

Auto-correlation results for CMP-1 surfaces showed that the post-GCIB surfaces resulted in a two-part auto-correlation with $p = 0.3$ and $p = 0.1$ for surfaces S-008 and S-009 respectively. GCIB processing left the short correlation component of C_A unchanged, within the limits of uncertainty, for all surfaces adding a long range component to S-008 and S-009 surfaces. It is usually the short range correlation component in C_A that leads to fractal like behavior of the *PSD* function for large values of k. Post-GCIB surfaces for CMP-2 surfaces were successfully fit by a one-part correlation. These results indicate that the extent of smoothing is highly dependent on the initial surface condition. In addition, surfaces S-009, S-010, S-012, S-013, and S-014 all showed a reduction in correlation lengths (ζ_a) while surfaces S-008 and S-011 showed an increase. These results are consistent with PSDs obtained from the AFM images.

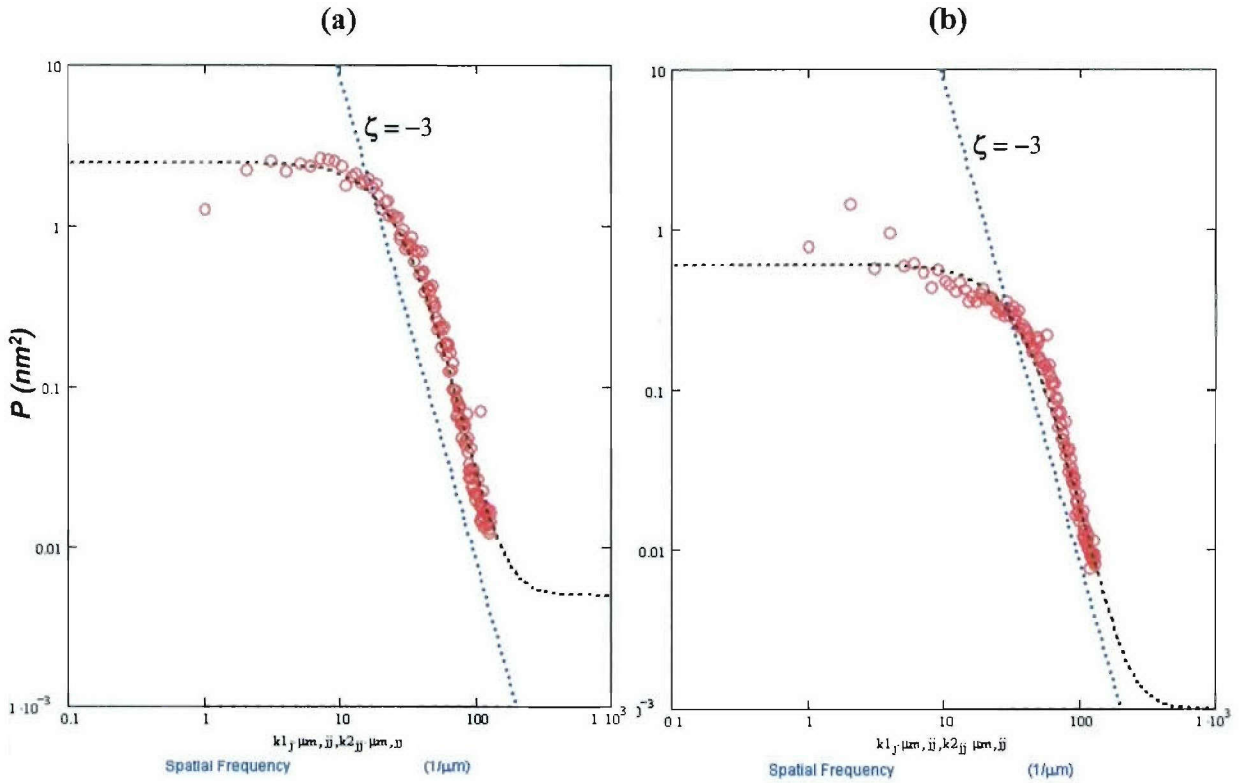

Figure 5.7. One dimensional PSD distribution of the AFM data (circles) and its fit to the k-correlation model (dashed lines) for: a) CMP and b) GCIB processed GaSb surfaces.

At the dimensions of a cluster impact, it is not feasible to simply consider the impact event singularly as point-like with an associated surface disturbance that propagates radially outwards, i.e. similar to surface diffusion and relaxation. Based on the success of Fenner's model, it was suggested that the cluster impacts also give rise to a high pressure gas that laterally escapes the immediate region of impact [5.13]. Thus, the resultant surface is formed as a result of the two processes, fine scale impact roughening and large scale gas smoothing, both of which are occurring simultaneously. As a consequence, the surfaces exhibit fractal roughness over length scales of a few radii of the impact crater, as observed for all GCIB processed surfaces, which is an intrinsic consequence of cumulative overlapping cluster impacts.

The surface disturbance due to a cluster impact travels some radial distance from the impact site before hydro-dynamically stalling and dissipating, while removing long range non-planar surface material in its path, i.e smoothing the surface. The consequence of the propagating surface disturbance due to GCIB is better understood by analyzing the height difference correlations.

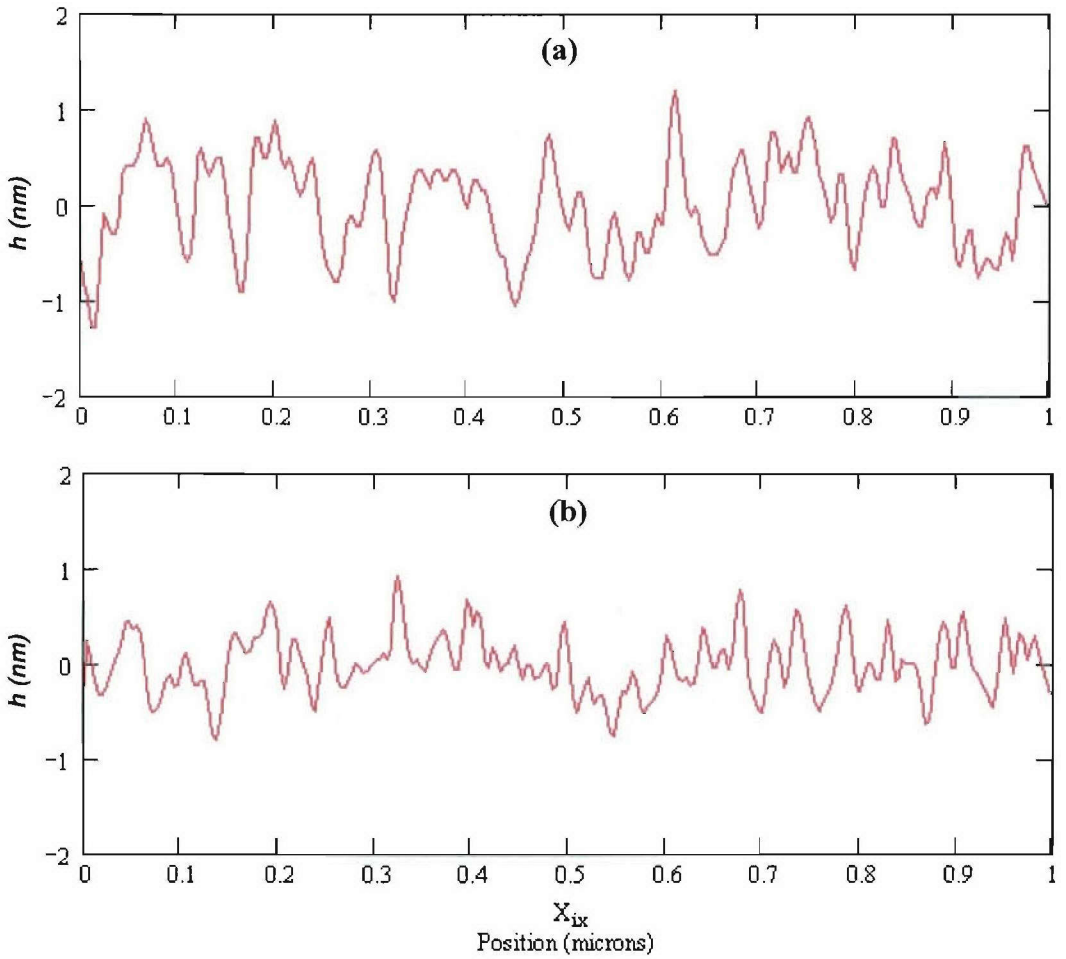

Figure 5.8. Typical height cross-sections of: a) CMP and b) GCIB-S009 processed GaSb surfaces. This data clearly shows a reduction of the total Z range due to GCIB processing as a result of smoothing.

Comparison of the height-difference correlation data showed that O_2-GCIB surface S-008 which underwent a 5kV final smoothing step had a correlation length ζ_d ~8.5nm as compared to the other O_2-GCIB surfaces S-010, S-012, and S-014 which underwent a 3kV final smoothing step which exhibited an avearge correlation length of ζ_d ~6.0nm. This reduction in correlation distance is a direct consequence of the fact that higher energy clusters cause atoms to flow along the surface for a larger lateral distance as compared to lower energy clusters. Thus, it is common practice to process substrates with two or more energy steps with reducing energies, where the first high energy step actually increases the roughness but reduces the overall *Z*- range while the second and/or third lower energy steps result in actually smoothing the surface.

Comparing the correlation lengths (ζ_d) of the three O_2-GCIB produced surfaces from the second batch of substrates, it can be seen that the dual-energy step GCIB processes S-010 and S-012 exhibited ζ_d = 6.5nm and 6.0nm respectively, while the triple-energy step GCIB process S-014 showed the lowest correlation distance ζ_d = 5.5nm.

So far we have only compared the results of the process parameters for the single-gas O_2-GCIB processed GaSb surfaces. When halogen components are included in the gas, there are chemical reactions taking place on the substrate surface that modify the properties and characteristics of the surface oxide and interface on GaSb. For instance, when analyzing surfaces with identical GCIB process parameters but different gases, such as O_2-GCIB (S-010), SF_6/O_2-GCIB (S-011), and $CF_4/O_2 + O_2$-GCIB (S-013), it was found that both the F_x-GCIB processed substrates were less fractal than the O_2-GCIB processed substrates. This could be due to the nature of the oxide layer formed on the GaSb substrate after GCIB processing. (XPS measurements on F_x-GCIB processed surfaces have shown the presence of a Ga- and Sb-fluoride film on the surface along with Ga- and Sb-oxides.) The correlation length (ζ_d) data also showed that the SF_6/O_2-GCIB process had $\zeta_d = 8.5$nm which was the highest followed by the $CF_4/O_2 + O_2$-GCIB surface which showed $\zeta_d = 7.5$nm, while the O_2-GCIB surfaces showed $5.5 < \zeta_d < 6.5$nm. This suggests that the surface disturbance due to a cluster impact, where the cluster contains a halogen component, tends to traverse a somewhat larger distance as compared to impacts due to pure oxygen gas clusters.

Roughness analysis of the GCIB produced surfaces showed characteristics of random fractals over at least some ranges of k for all 1 x 1μm^2 surfaces while the 10 x 10μm^2 surfaces exhibited mostly white noise. The impact of GCIB smoothing happens only over a limited bandwidth of k, i.e. from ~50nm to ~5μm. In general, cluster impacts dominate the roughness for small dimensions with its effect diminishing over larger dimensions where the post-GCIB topography is governed almost entirely by the initial conditions. Thus, for wafers with highly polished surfaces, such as surfaces S-010 to S-014, GCIB processing shows fractal properties for small dimensions and mostly white noise for larger dimensions.

Statistical analysis of surfaces to determine fractal properties is a powerful technique to ascertain the effects of the GCIB process and can be used as a method to develop and determine an ideal process strategy in terms of reactive gas, energy steps, and fluence. The process strategy and its parameters are, of course, dependent on the initial surface conditions of the substrate.

However, it is important to remember that AFM measurements usually provide information of the surface topology of the oxide which under ideal conditions replicate the substrate surface beneath. Thus, for applications such as epitaxial growth where the oxide layer is desorbed or ohmic contact formation that requires thickness uniformity, it is important to characterize the substrate-oxide interface, as discussed earlier.

Table 5.2. Results of the statistical analysis performed on 1 x 1μm^2 AFM images of CMP and GCIB processed GaSb substrates exhibiting random fractal properties. The 10 x 10μm^2 images of the same surfaces showed mostly white noise and no fractal properties.

Sample#	Surface Preparation Method (Gas, Acceleration & Fluence)	*AFM Measurement*		*Auto-Correlation*				*Height Correlation*		*k-Correlation*		
		ΔZ (nm)	R_{rms} (nm)	H_a	ξ_a (nm)	Double Exponent	Mound Rough	H_d	ξ_d (nm)	ζ_p Slope	H_p	B_p (nm)
S-008	CMP-1	7.61	0.60	0.8	8.5	0 %	No	1.0	5.5	-3	1.0	**25**
+ GCIB	O_2: 10kV, 1E15 + O_2: 5kV, 3E15	5.32	0.48	0.8	10.0 40.0	70% 30%	No	1.0	8.5	-3	1.0	**40**
S-009	CMP-1	5.6	0.54	0.9	9.0	0 %	No	1.0	6.5	-3	1.0	**30**
+ GCIB	5% CF_4/O_2: 10kV, 1E15 + 5% CF_4/O_2: 3kV, 3E15	6.45	0.33	0.9	6.0 10.0	90% 10%	No	1.0	5.0	-3	1.0	**22**
S-010	CMP-2	3.39	0.37	0.9	9.5	0 %	No	1.0	6.3	-3	1.0	**33**
+ GCIB	O_2: 10kV, 1E16 + O_2: 3kV, 3E16	5.47	0.32	0.9	9.5	0 %	No	1.0	6.5	-3	1.0	**33**
S-011	CMP-2	3.09	0.35	0.8	11.0	0 %	No	1.0	7.5	-3	1.0	**33**
+ GCIB	1% SF_6/O_2: 10kV, 1E16 + 1% SF_6/O_2: 3kV, 1E16	6.05	0.58	1.0	12.5	0 %	No	1.0	8.5	-3	1.0	**41**
S-012	CMP-2	3.59	0.38	0.9	10.0	0 %	No	1.0	7.0	-3	1.0	**30**
+ GCIB	O_2: 10kV, 1E16 + O_2: 3kV, 3E15	3.45	0.34	1.0	8.2	0 %	No	1.0	6.0	-3	1.0	**28**
S-013	CMP-2	4.48	0.43	0.9	12.0	0 %	No	1.0	8.5	-3	1.0	**37**
+ GCIB	5% CF_4/O_2: 10kV, 1E16 + O_2: 3kV, 1E16	5.93	0.45	1.0	10.0	0 %	No	1.0	7.5	-3	1.0	**35**
S-014	CMP-2	3.25	0.33	0.9	10.0	0 %	No	1.0	7.0	-3	1.0	**33**
+ GCIB	O_2: 30kV, 1E16 + O_2: 10kV, 1E16 + O_2: 3kV, 1E16	3.88	0.29	0.9	8.2	0 %	No	1.0	5.5	-3	1.0	**27**

5.2.4 Thermal X-Ray Photoelelectron Spectroscopy Analysis

To quantitatively measure the thermal properties of the oxide produced on GaSb substrates the group was fortunate to have access to Hanscom/AFRL's X-ray photoelectron spectrometer and surface scientist, Helen Dauplais. Helen's instrument is unique in that spectra can be taken before and after a wafer is heated to a specific temperature. Furthermore, since the background pressure of the instrument is in the low 10^{-10} Torr range, no reoxidation occurs between temperature cycles. Thus a sample can be cycled so that each temperature step is hotter than the next and a sequence of spectra can be taken to determine at what temperature the oxide thermally desorbs from the sample. This is a critical piece of information that can be directly used to set up oxide desorption heating cycles for MBE epitaxial overgrowth. Figure 5.9 show the typical spectra generated by the thermal X-ray photoelectron spectrometer (TXPS). As one sees in the sequence, this particular antimony oxide was fully removed at 500° C.

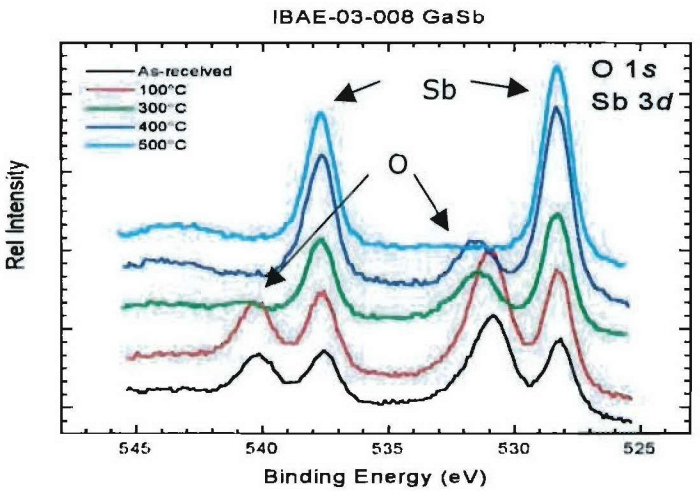

Figure 5.9 Thermal X-ray photoelectron spectra showing the evolution of the surface oxide in an ultra-high vacuum system as a function of substrate temperature. As one sees in the figure the antimony oxides have thermally desorbed by the time the temperature reaches 500° C.

5.3 Gas Cluster Ion Beam Smoothing

5.3.1 GCIB System Overview

GCIB is a recent technology that modifies sample surfaces by heating and laterally sputtering the surface with large clusters of slow moving, weakly bonded atoms. As first mentioned in the fractile analysis method section, GCIB smoothing techniques were applied here to GaSb substrates and shown to further smooth a high-quality CMP GaSb wafer. Specifically, we have added a chemically active fluoride component to the beam. The resulting enhanced etch of the GaSb surface provided reduced sub-surface CMP damage in a slightly damaged GaSb wafer and maintained or improved the surface smoothness.

GCIB systems and the GCIB process have been described extensively in the literature with perhaps the most complete review on the subject by Yamada et al [5.2]. In a brief synopsis, GCIB equipment consists of three chambers: the nozzle chamber (nozzle, skimmer), the ionizing chamber (ionizer, accelerator, lens assembly) and the processing chamber (scanning plates). Figure 5.10 shows a schematic of the GCIB system. In the nozzle chamber, the small-orifice supersonic nozzle generates a collimated neutral cluster beam from a pressured compartment of several atmospheres into a vacuumed section. A skimmer then collects the primary jet core of gas clusters. The beam aligns itself with the axis of expansion so that a fraction of the beam that moves in the forward direction into the high vacuum ionizing chamber. The ionized clusters are extracted and accelerated typically from 2 kV to 25 kV using a series of electrodes that act as a mass filter. Electrostatic lenses are utilized to focus the cluster ions, and monomers are filtered out through the use of a transverse magnetic field. Ion fluence is measured by a Faraday cup. The sample is mechanically scanned for complete wafer coverage according to total dose requirements and the system is capable of 200mm high wafer throughputs with programmable speeds for wafer uniformity correction (variable dose) processing. The GCIB instrument, trade name Ultra-Smoother^{TM}, used in this work is a commercial model manufactured by Epion Corporation.

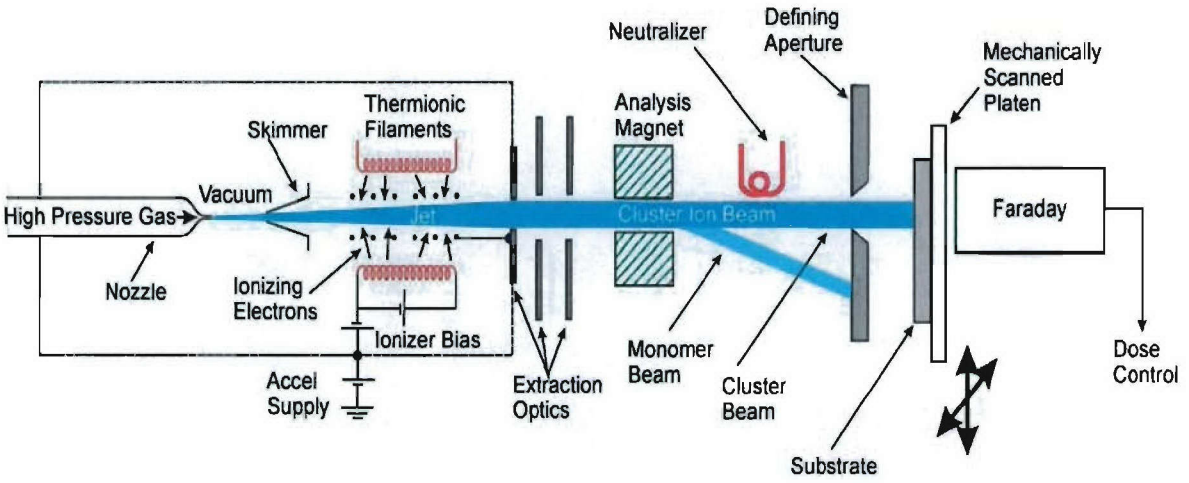

Figure 5.10. Schematic diagram of a gas cluster ion beam system

5.3.2 GCIB Smoothing Experiments

Experiments were designed to examine the effect of GCIB energy and gas source on GaSb surface and sub-surface damage. The experiment used two 50mm GaSb wafers. The first GaSb (100) substrate (sample-A) was divided into four sectors on which four different GCIB processes for etching and smoothing were applied. Process-1 consisted of 10kV oxygen smoothing (no observed etching) step followed by a 3kV low energy oxygen smoothing process. Process-2 was identical to the first, but with argon as the gas cluster source so as to provide etching at 10kV. Process-3 incorporated the same etch and smooth acceleration energies, but with a fluoride source that provided enhanced etching. Process-4 incorporated a 10kV argon etching step and a 3kV oxygen smoothing step. The total ion fluence for the dual energy processes was 4×10^{15} ions/cm^2, where each ion has an associated ~1500 atoms per charge. The second substrate (sample-B), a non-optimally polished (100) GaSb substrate, was subjected to a tri-energy GCIB process consisting of 30, 10 and 3kV fluoride GCIB steps.

Figure 5.11 shows the effects of oxygen GCIB due to process-2 on sample A. This was a dual energy GCIB procedure using higher 10kV oxygen molecule clusters followed by lower 3keV for smoothing with a total dose of 5×10^{15} ions/cm^2. Figure 5.11 a) and b) show 1μm x 1μm AFM images of the GaSb wafer surface before and after GCIB. A comparison between the two images shows a decrease in surface roughness. In this particular example, the RMS value of roughness dropped from the original 0.65nm down to 0.18nm. The z (peak-to-valley) value decreased from 6.3nm to ~ 2.3nm. Figure 5.11 c) shows the comparison of the Power Spectrum Density (PSD) or spatial frequency content of the surface roughness before and after the O_2 molecule GCIB procedure. It can be observed that the high frequency roughness decreases dramatically within the range of 32.8-100cycle/μm across the surface of the GaSb sample area. This is observed by the reduced intensity curve that represents actual distributions of the surface feature shape frequencies as observed after the PSD Fourier transformation process. This range is important for surface "spike" or high frequency surface anomaly

reduction to ensure a higher quality of molecular beam or other type of epitaxial growth in subsequent device processing.

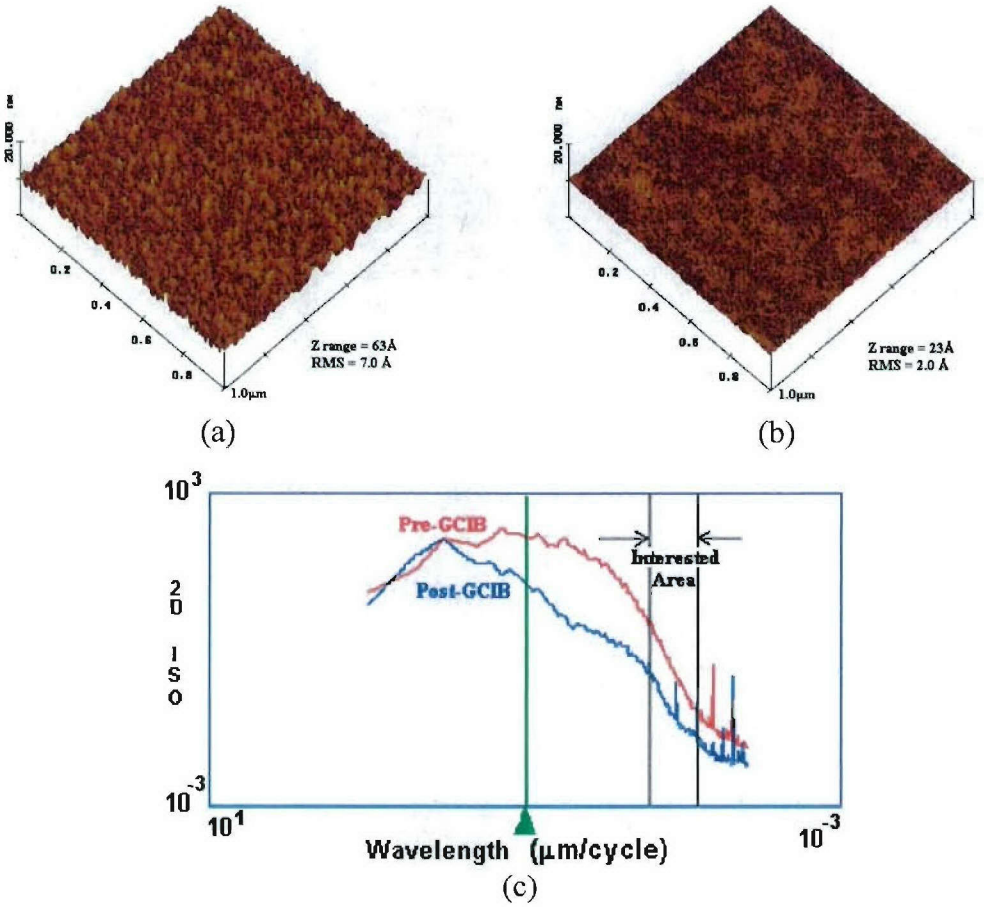

Figure 5.11. 1x 1μm AFM images of sample A before (a) and after (b) oxygen gas cluster processing. A comparison of the AFM power spectrum densities shown indicates a reduction of the higher spatial frequency roughness.

Figure 5.12 consists of a set of AFM surface images taken on each section of the total GaSb substrate, with the gas cluster processes as indicated in Table 5.3. The material characteristics produced by the processes are tabulated. The kinetics and chemistry of the surface interaction of the cluster beam are strongly dependent upon the beam energy and the gas composition of the clusters [5.4]. When using a reactive oxygen molecule GCIB species at high cluster acceleration voltages, deeper cluster impact pits (etching) along with a thicker stoichiometric oxide surface is achieved [5.4,5.5]. Using the same gas species at low cluster acceleration voltages, negligible etching (~1 nm shallow impact pits) and a smoother surface with an associated thinner saturated-oxide surface is achieved. For Ar gas cluster impacts accelerated at 30kV, for example, the surface craters created from impact into semiconductor material has been shown to be as deep as 20 nm [5.5]. As shown in Table 5.3, the various combinations of gases had distinguishable kinetic and chemical lateral sputtering effects resulting in measured differences in etching speeds, surface smoothness, and oxide thickness.

The data shows that use of the oxygen gas cluster gave the smoothest surface, the fluorine gas cluster etched the fastest, and the non-reactive argon gas cluster prevented a thick oxide from forming. The fluoride process, in particular, with its excellent smoothing and relatively thin oxide production may be useful in molecular beam epitaxy, providing a smooth substrate to epilayer interface and a reasonable temperature of oxide desorption.

Figure 5.13 a) shows the AFM of the as-received substrate (sample-B), a slightly damaged CMP polished GaSb wafer with a number of extended near-surface defects, presumably formed during the wafer polishing and/or chemical etching. The triple energy, single fluoride gas species process used here was designed to rapidly remove surface material through the subsurface damage layer in the 30kV step and provide a smoothing process without underlying material damage in the 10kV and 3kV steps. Ion sputtering can preferentially remove atoms from dislocated regions compared to those in defect-free crystal. Such preferential sputtering could therefore account for the initial roughing of the surface as the GCIB sputters through this defect layer, as seen in Fig. 5.13 b). The stochastic overlay of the larger impact craters from a higher energy sputtering process would result in a surface that is substantially different in appearance and frequency from the initial substrate [5.4,5.5]. In this case, the surface scratches are obliterated in favor of a uniform, overlapping crater terrain. Figure 5.13 c) illustrates the final result of a triple energy fluoride GCIB process after etching 200nm GaSb. The RMS roughness of the surface dropped from the as-received value of 0.41 nm to a processed value of 0.35 nm. The smoothing effects observed here are typical for the GCIB process and well explained in Reference 5.2. The x-ray rocking-curve (111) peaks for sample-B dropped from an initial FWHM of 76 to 52 arc-seconds after undergoing the triple energy process. The x-ray rocking curve FWHM data for sample-A was constant throughout the entire experiment yielding a FWHM of around 15 and 20 arc-seconds for the (400) and (111) peaks respectively, both values near the theoretical limit. Thus, GCIB processing did not introduce damage to sample-A and decreased the damage to sample-B. The reduction in the FWHM of the (111) x-ray peaks of sample B suggests that the GCIB procedure etched away or possibly self-annealed part of the surface and subsurface damage. Through a series of wet etching steps followed by X-ray characterization, it was found that sample-B was damaged through its entire thickness. The fact that only 200nm of surface removal using a CGIB schedule was able

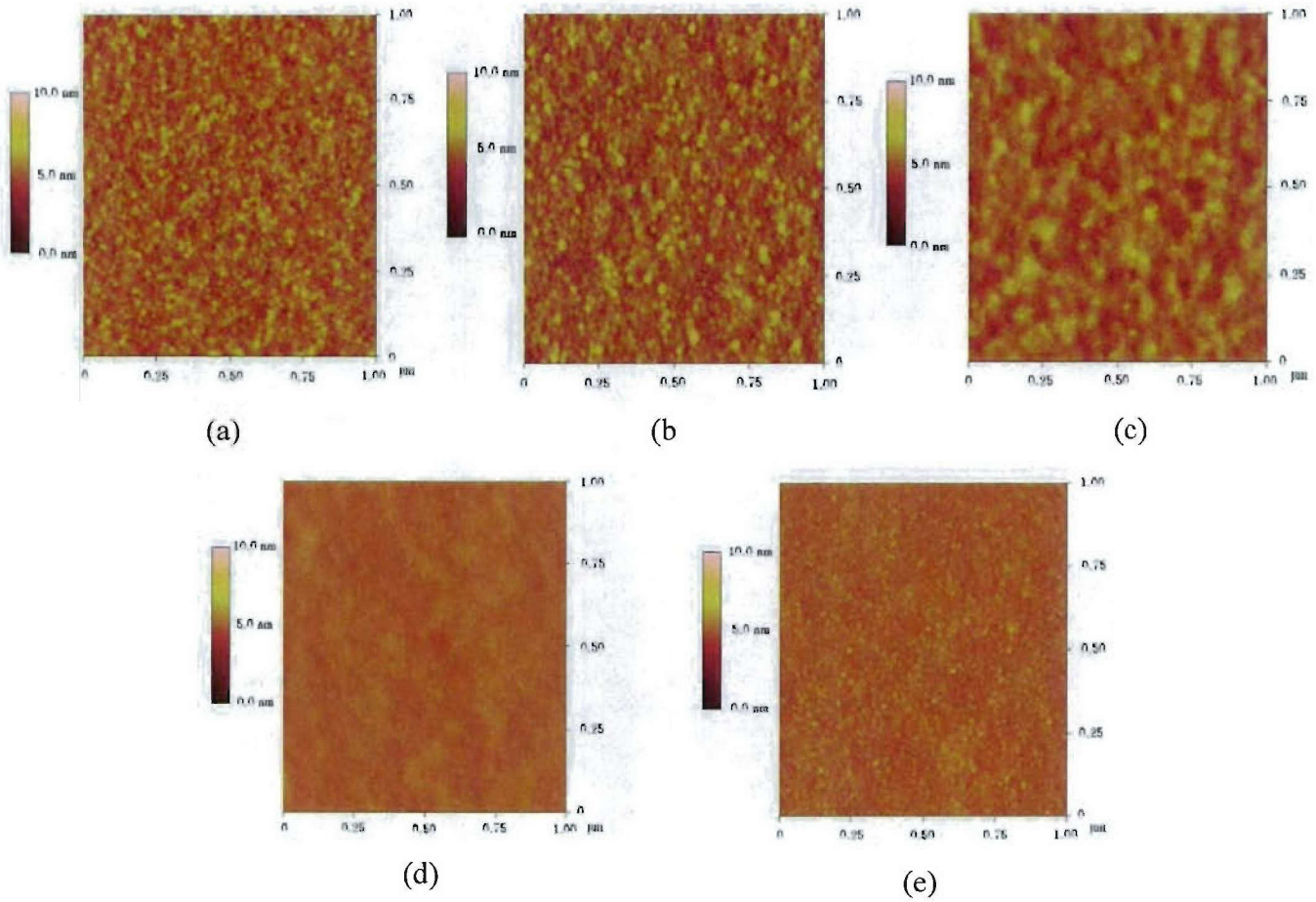

Figure 5.12. AFM images of the surfaces of sections of sample A processed with the various GCIB processes discussed in the text. The initial surface is shown in (a). The results of the argon, argon/oxygen, oxygen and fluoride GCIB processes are shown in b), c), d) and e) respectively.

Table 5.3 Result obtained using the various GCIB processes on sample A

	Z range (nm)	RMS (nm)	PSD (nm^2)	Oxide thickness (nm)
Before GCIB	6.3	0.65	0.128	4.40
Oxygen GCIB	2.3	0.18	0.00744	10.22
Argon GCIB	7.0	0.75	0.124	4.23
Fluoride GCIB	3.3	0.32	0.0503	6.53
Ar GCIB + O_2 GCIB	51.6	0.62	0.0335	9.44

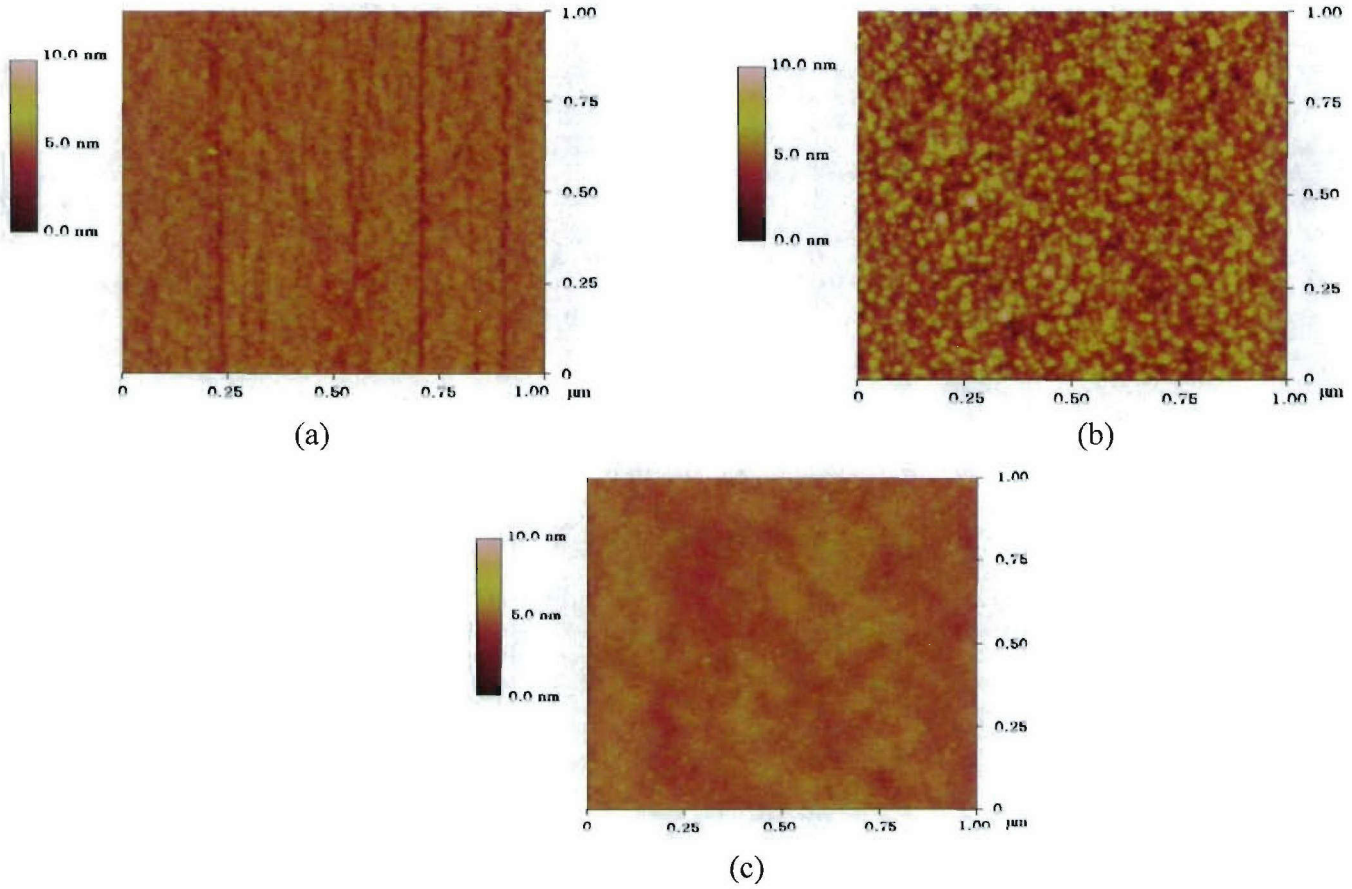

Figure 5.13. AFM images taken during the triple energy GCIB process used for sample B. Part (a) shows the initial surface image with an RMS value of 0.410 nm. The RMS roughness increased to 1.083 nm after the 30 kV etch / sub-surface anneal step (b) and was shown to decrease to 0.354 nm after the 10 kV and 3 kV smoothing step (c). SE measurements and modeling confirm that the lower energy GCIB processes do not contribute to the GaSb etching process but substantially influence the surface RMS roughness.

to significantly improve the rocking curve half-widths may indicate that the GCIB process is also able to anneal out a portion of the surface and subsurface polish damage produced with a non-optimal CMP. The three-step GCIB schedule may be important here. The higher voltage first step not only removes material but generates short bursts of very-high temperatures at the surface, of the order of several thousands of degrees for only several picoseconds [6], which while inducing some surface damage may also anneal the material much deeper than the surface damaged region. Subsequent lower-voltage processing steps remove the damage from the initial steps while preserving an annealed subsurface layer.

With the use of specific energies and chemistry, GCIB has been shown to improve the surface smoothness and reduce sub-surface damage for CMP GaSb substrates. The process also

is able to produce controlled oxide thicknesses on the wafer surfaces (Section 5.3.1). GCIB smoothing appears to be viable for improving GaSb wafer surfaces without inducing damage. Argon processing gave the thinnest oxide with the least smoothing effect. The oxygen process gave the smoothest surface, yielding a thicker post-GCIB oxide layer. The fluoride GCIB process resulted in both a faster etch and a thin oxide layer with a smooth final surface, indicating only a slight compromise on the final surface roughness. Although we found that the triple energy GCIB process held no advantage over a dual-energy GCIB process in decreasing surface roughness, the tri-energy process may reduce a significant amount of subsurface damage through the 30kV instantaneous temperature and pressure delivered with the gas cluster ion impact.

5.3.3 Oxide Control with GCIB

Nine GCIB processes were investigated in this work as candidates for the final polishing processes. These processes are listed in Table 5.4 below along with a list of wet etch and directly out of the box CMP samples that were overgrown with MBE. MBE growth run numbers are in the left column of the table and will be referred to instead of the GCIB process number. The goal as stated initially, was to find a GCIB or IBAE process that produced "epi-ready wafers."

The oxygen process, MBE 03-077, was a dual-energy single-gas GCIB process that included a moderate energy (10kV) oxygen based etch step followed by a low energy (3kV) oxygen based smoothing step with a relatively low total GCIB dose of 4 $x10^{15}$ ions/cm^2. Half the wafer was masked so that the same substrate contained both CMP and GCIB polished surfaces. AFM images with a resolution of $10x10\mu m^2$ show that the surface roughness was not significantly altered by the GCIB process. However, X-Ray Photon Spectroscopy (XPS) measurements made on the two surface regions showed that the composition of surface oxides were significantly different. Figure 5.14 shows the XPS profile data through the oxides of the CMP region that received no GCIB processing and Fig. 5.15 shows the XPS profile data through the GCIB processed region. Figure 5.16 shows the XPS profile through the oxide layer of a GCIB CF_4/O_2 processed sample. Each GCIB process produced its own unique oxide in the sense that the combination of the thickness of the oxide and the composition of the oxide was process dependent.

As one sees in the figures, assuming the same profile sputter rates, both the thickness and nature of the oxides on the two wafers are different. The question is which oxide should be designed for the surface? The antimony oxides desorb earlier with temperature, and the gallium oxides desorb near the melting point of the wafer. The antimony oxides may be well suited for MBE while the gallium oxides may be better suited for metal-organic chemical vapor deposition (MOCVD).

All GCIB processes were applied to CMP (100) GaSb wafers that were then used for MBE growth experiments. Although current results are preliminary, MBE sample 03-077, and the CF_4 process, MBE sample 03-078 are more promising than the others.

MBE Run	GCIBProcess ID	Reactive Gas	Energy	Dosage
03-91	F780-S010	Oxygen	10kV	1×10^{16}
		Oxygen	3kV	1×10^{16}
03-93	F780-S011	1% SF_6/O_2	10kV	1×10^{16}
		Oxygen	3kV	1×10^{16}
03-92	F780-S012	Oxygen	30kV	1×10^{16}
		Oxygen	10kV	1×10^{16}
		Oxygen	3kV	1×10^{16}
TBD	F780-S013	Oxygen	10kV	1×10^{16}
		Oxygen	3kV	1×10^{15}
03-94	F780-S014	5% CF_4	10kV	1×10^{16}
		Oxygen	3kV	1×10^{16}
03-78	F780-S009	5% CF_4	10kV	1×10^{15}
		Oxygen	3kV	3×10^{15}
03-82	F780-S007	2% SF_6/O_2	10kV	1×10^{15}
		Oxygen	3Kv	3×10^{15}
03-81	F780-S006	Oxygen	10kV	1×10^{16}
		Oxygen	5kV	5×10^{15}
03-77	F780-S008	Oxygen	10kV	1×10^{15}
		Oxygen	3kV	3×10^{15}
03-75	CMP			
03-76	CMP			
03-72	Br wet etch			
03-73	CMP			
03-74	Br wet etch			

Table 5.4. A list of Epion GCIB processed samples along with a list of CMP samples and wet etched CMP samples all of which were overgrown using MBE. Note that the dosage data for the GCIB processes are the faraday cup current readings and each cluster contains many more atoms that counted by its singley charged state.

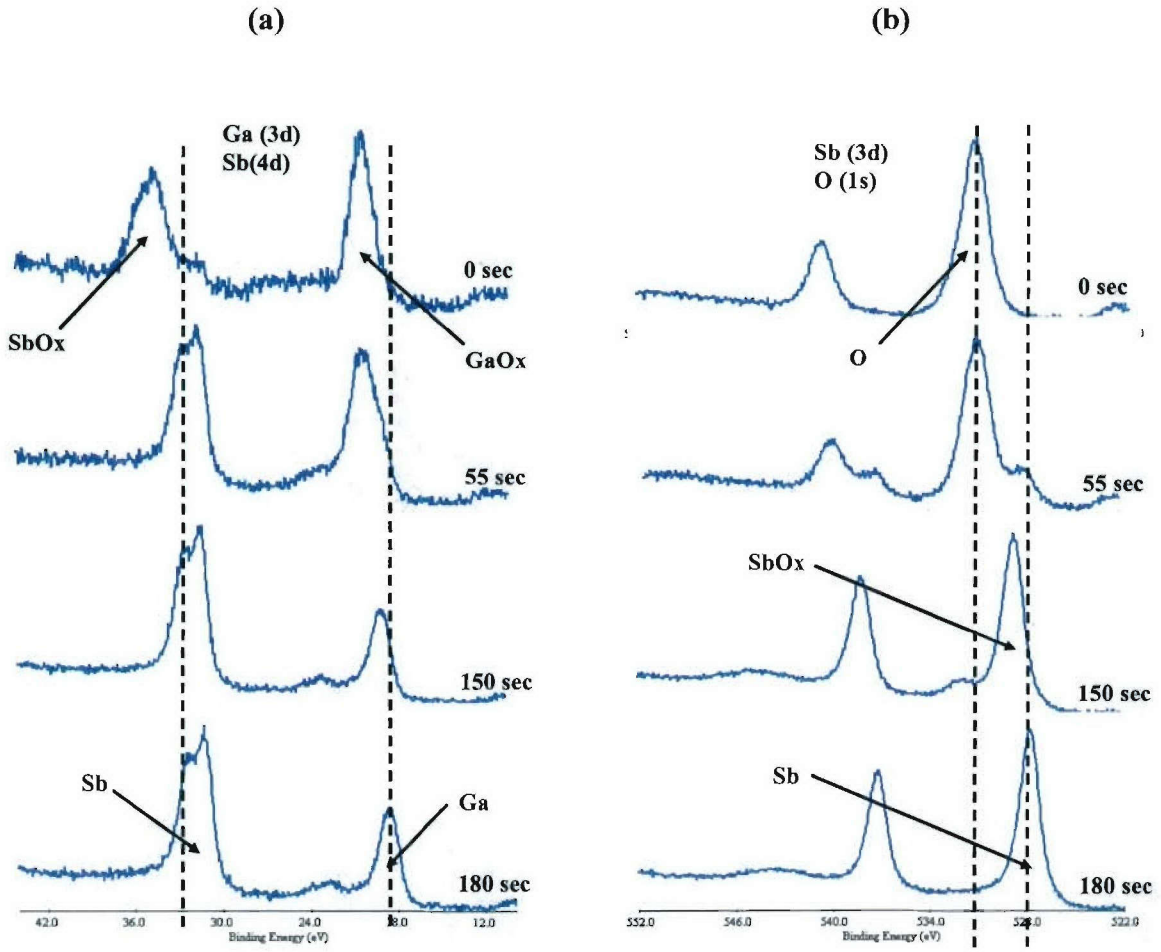

Figure 5.14. XPS spectra and depth profile of a CMP finished GaSb substrate as a function of sputtering time. The surface initially contains both Ga and Sb oxides which decrease with increasing sputtering time to yield metallic Ga and Sb after 180 s.

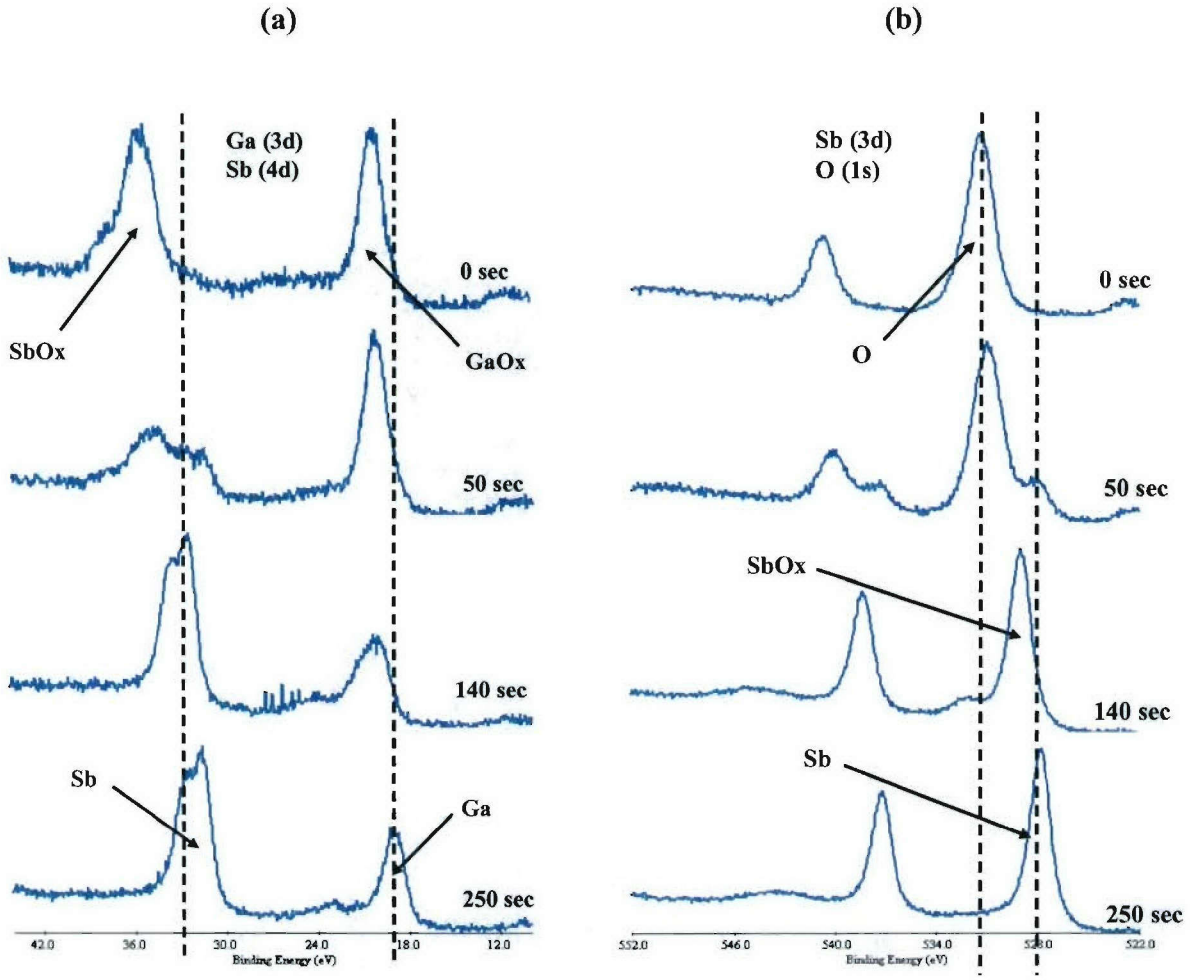

Figure 5.15. XPS spectra and depth profile of an O_2 based GCIB processed GaSb substrate as a function of sputtering time. The surface initially contains both Ga and Sb oxides which decrease with increasing sputtering time to yield metallic Ga and Sb after 250 s.

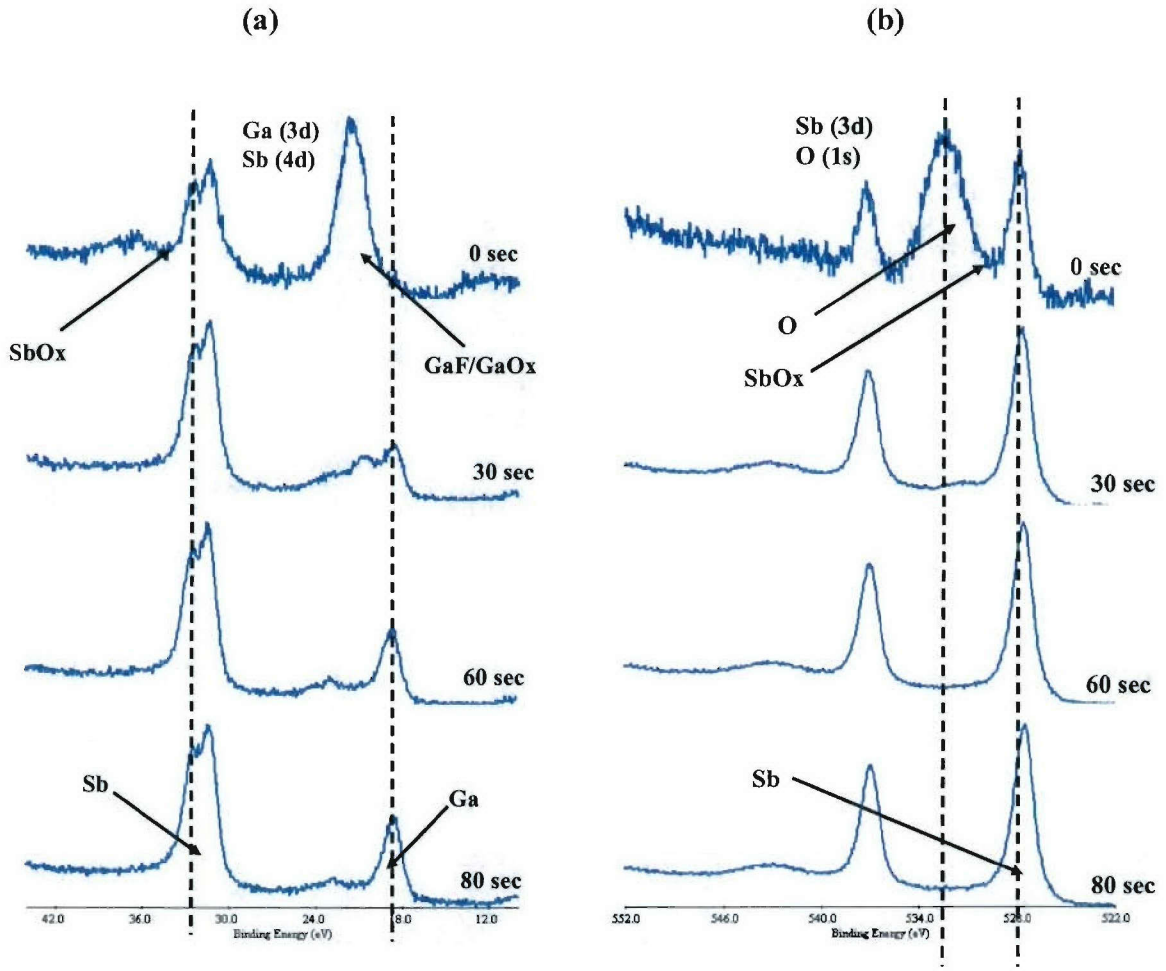

Figure 5.16. XPS spectra and depth profile of the CF_4/O_2 based GCIB processed GaSb substrate as a function of sputtering time. This surface comprised mostly of Ga oxides and fluorides with minimal Sb oxides, all of which decreased with increasing sputtering time to yield metallic Ga and Sb after 80secs.

5.3.4 MBE Overgrowth Experiments

Before discussing the overgrowth of the GCIB samples, baseline overgrown CMP sample and overgrown wet-etched CMP sample data is given for comparison to the GCIB data that follows. Cross-sectional transmission electron micrographs (XTEM's) of the epitaxial and epi/substrate interface portions of two wet-etched CMP samples is shown in Fig. 5.17. The XTEM in part a) shows no defined interface which we interpret as meaning there are no structural problems at the interface. The XTEM of part b) shows a thin layer of dark contrast at the interface that may be due to the incorporation of impurities which dope the interface.

Overgrown CMP samples show micro-voids, other defects and faults at the epilayer/substrate interface. Typical results are shown in Fig. 5.18, XTEM's of the interfaces. In part a) a stacking fault and other defects are shown emanating from the interface and in b) two micro-voids are shown at the interface. We suspect that incomplete desorption of the surface oxide and CMP damage are main causes of the problem.

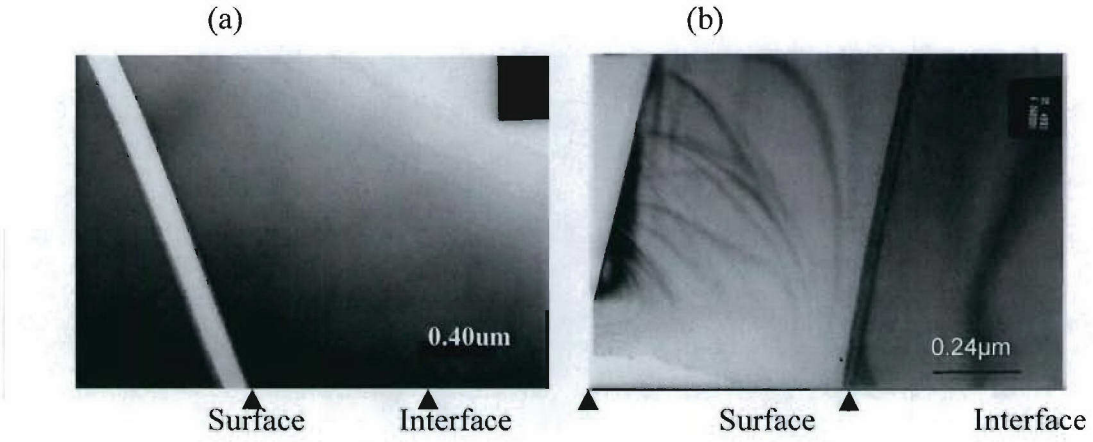

Figure 5.17. Part a) XTEM of an overgrown wet-etched sample where the interface was not observable. Part b) XTEM image of an overgrown wet-etched sample with a thin high contrast layer at the interface (MBE 03-072).

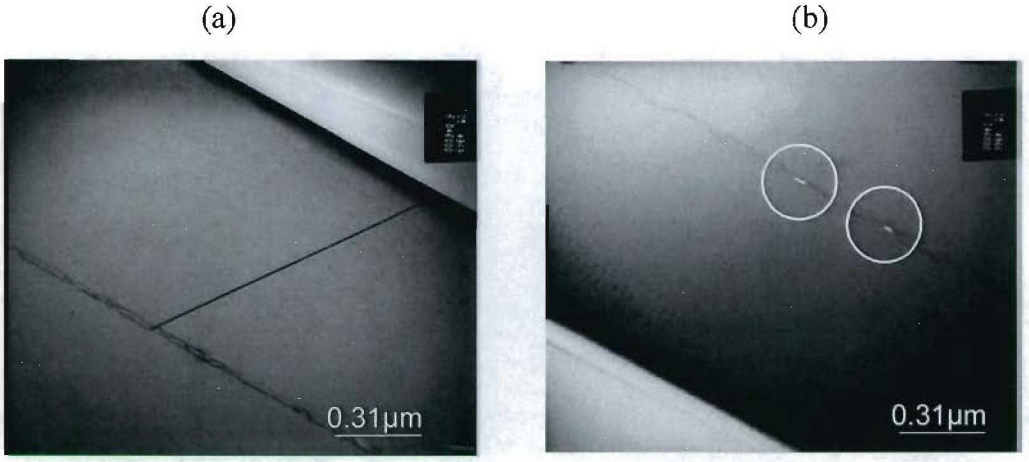

Figure 5.18. XTEM images of epi-growth CMP finished GaSb substrates indicating the presence of: a) a stacking fault and b) voids.

With the wet and CMP baselines established, 2" CMP processed GaSb wafers were masked and one side GCIB processed. The oxide layers on the two regions of a half O_2 GCIB substrate were simultaneously and successfully desorbed in the MBE growth chamber (monitored by observing the RHEED patterns from the surface) by raising the substrate temperature to 560°C. Starting with a homoepitaxial layer of GaSb, five periods of GaSb/AlGaSb layers were grown on both surfaces simultaneously in an Sb rich environment with a substrate temperature of 470°C. XTEM images, Fig. 5.19, of the substrate/epi interface show that the CMP finished region contained defects that propagated to the first AlGaSb barrier layer while the GCIB finished region showed no such defects.

We find our technique of marking the growing epilayer with thin AlGaSb layers very useful in determining the evolution of the growing surface. For example the dip in Fig 5.19 a) would not be noticed if the epilayer was not marked since the dip is corrected with another 100 nm of growth.

The fluorine process, MBE 03-078, was a dual energy, dual gas species GCIB process that included a 10 kV CF_4/O_2 etch step followed by a 3kV O_2 smoothing step with a total charge fluency of 4×10^{15} ions/cm^2. Again half the wafer was masked so that the same substrate contained both CMP and GCIB polished surfaces. Figure 5.20 shows XPS profile data through the oxides of the GCIB region of this sample prior to MBE growth. Here one sees a strong surface signal from fluorine and an oxide layer primarily composed of gallium oxides. Also the oxide layer is significantly thinner than that formed with the oxygen process (03-077).

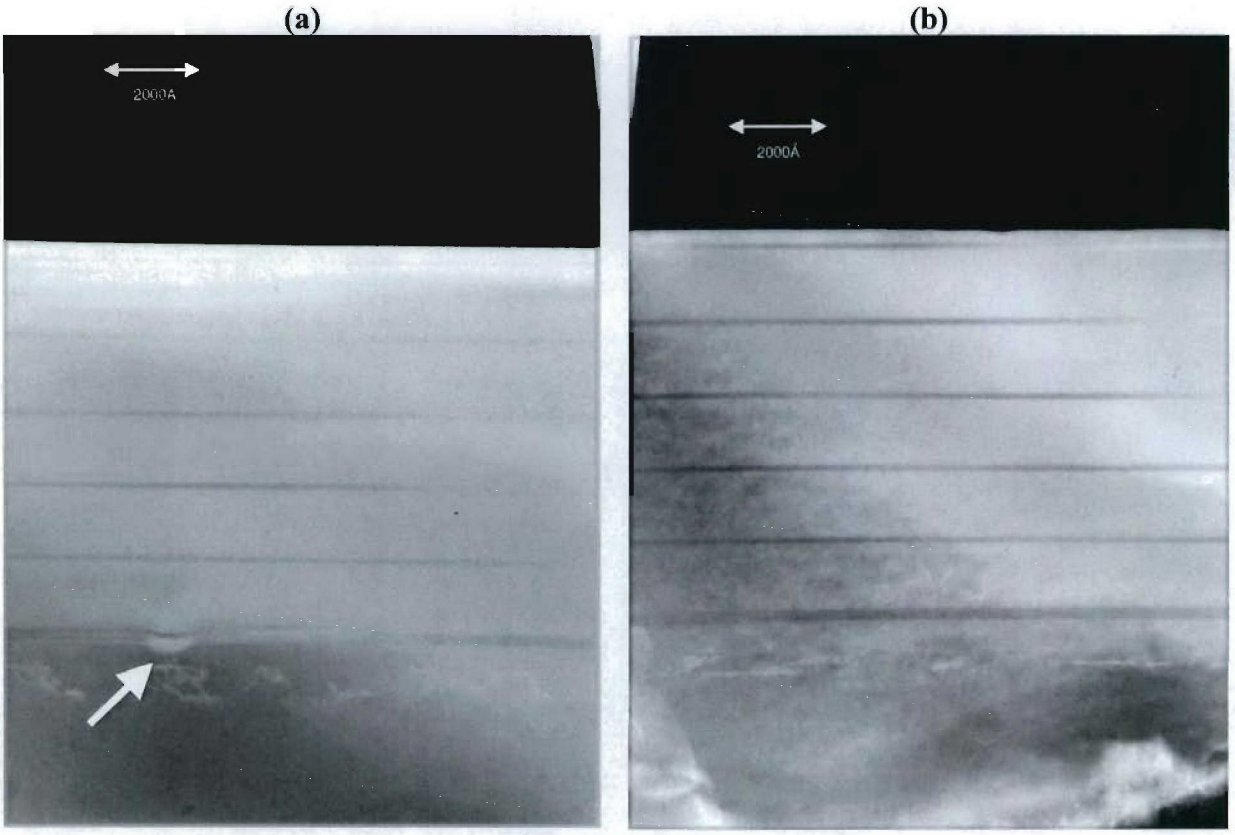

Figure 5.19. XTEM images of epi-growth GaSb/AlGaSb on: a) CMP and b) O_2-GCIB finished surfaces. These low magnification images of the entire substrate clearly shows pitting in the CMP finished surface as compared to the GCIB finished surface. However, this defect does not propagate and disappears by the second marker layer.

This wafer was also overgrown. One peculiarity was noted during outgassing in the preparation chamber. This fluorine based GCIB substrate showed heavy outgassing which could be attributed to the presence of unstable fluorine based polymers on the substrate surface. Once outgassed the wafer behaved well in the growth chamber and the AlGaAs marked GaSb epilayer applied. Figure 5.21 show an XTEM of the GCIB processed side of the overgrown wafer.

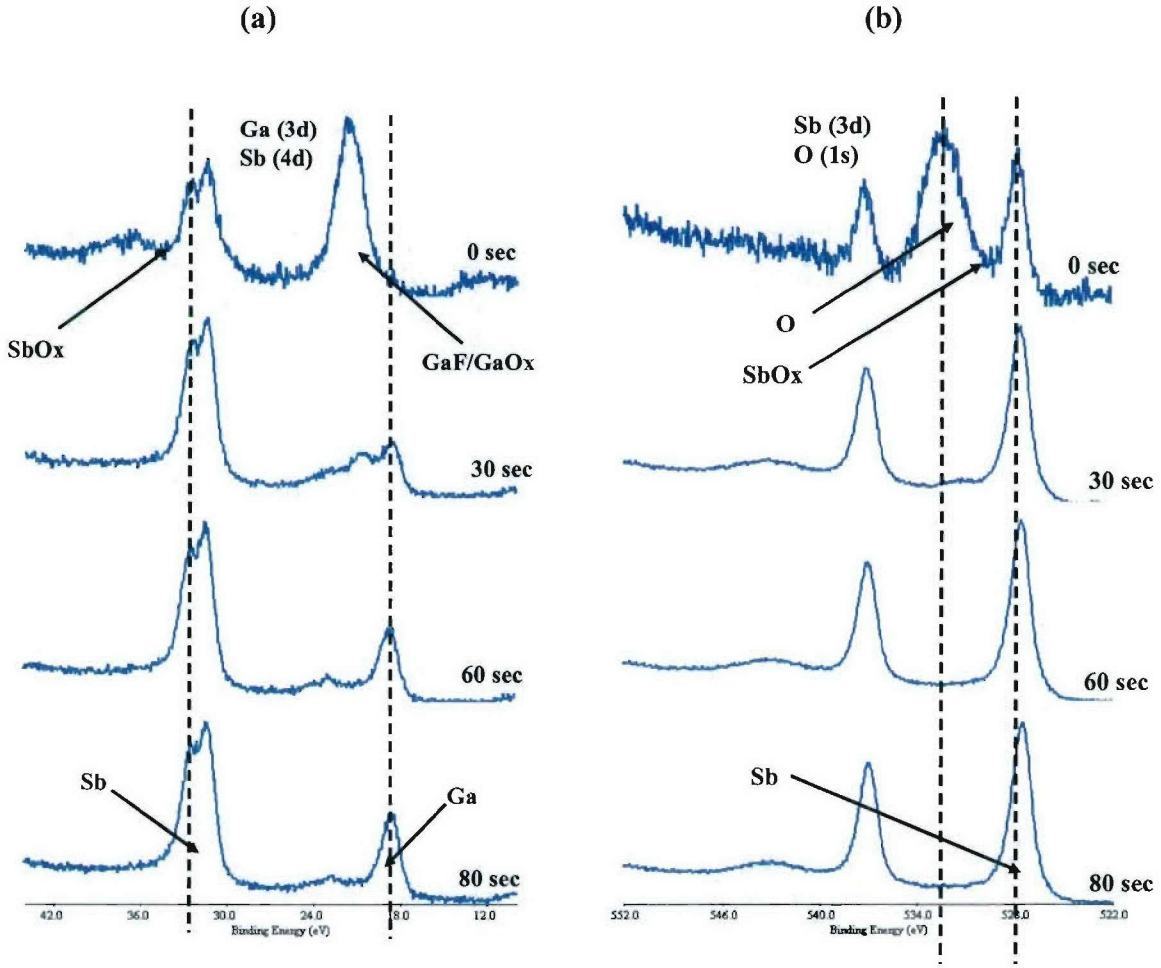

Figure 5.20. XPS spectra and depth profile of the CF_4/O_2 based GCIB processed GaSb substrate as a function of sputtering time. This surface comprised mostly of Ga oxides and fluorides with minimal Sb oxides, all of which decreased with increasing sputtering time to yield metallic Ga and Sb after 80secs.

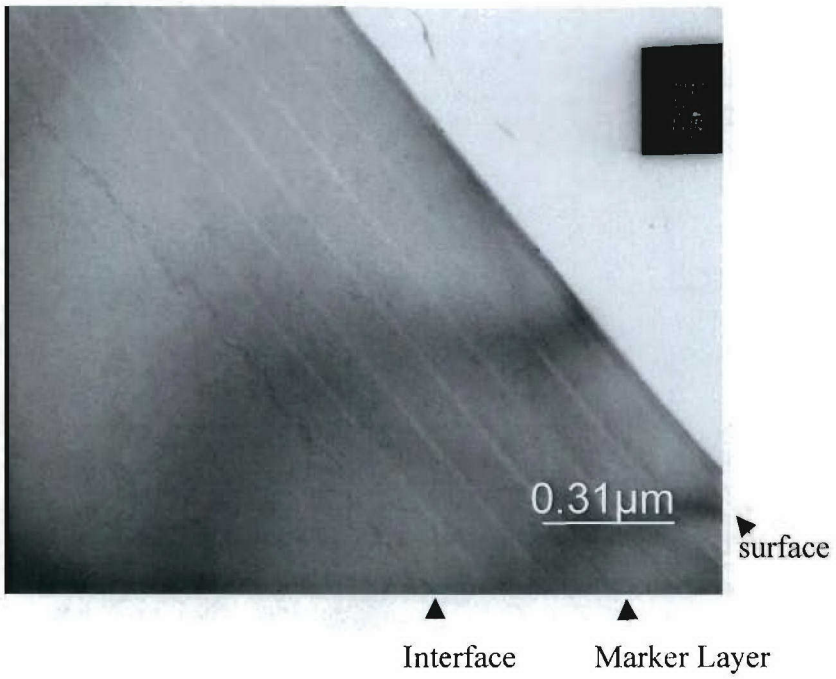

Figure 5.21. XTEM image of the epilayer and interface of the fluorine processed GCIB sample (MBE 03-078).

Photoluminescence data was taken at 77K with a new spectrometer system set up for the task. Figure 5.22 shows the spectra from the epilayers of the oxygen and fluorine processes. Although more work need to be done in this area, both samples showed 77K PL with the flourine sample (03-078) being a bit stronger than the oxygen sample (03-77) (scales in figure are arbitrary, 078 was stronger with better signal to noise ratio).

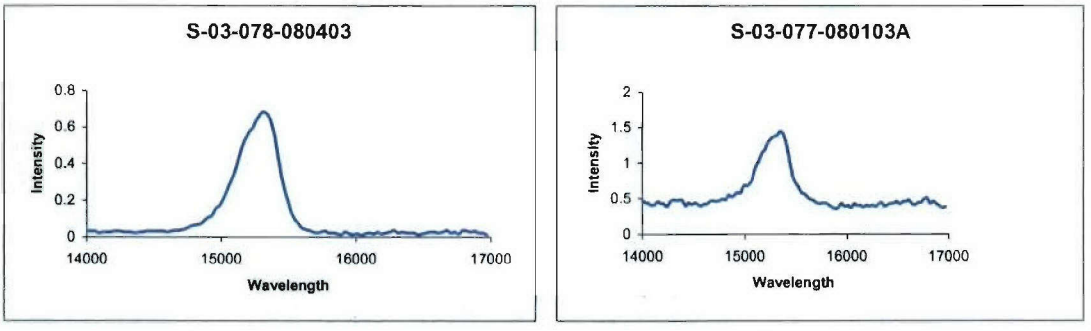

(a) (b)

Figure 5.22. Photoluminescence spectra at 77 K from a) the fluorine processed sample and b) the oxygen processed sample.

5.3.5 Fractal Analysis of GCIB Surfaces and Episurfaces

Epitaxial layers using MBE were grown on CMP and GCIB finished surfaces. The surface topology of MBE grown episurfaces were obtained using an AFM for scan sizes of 1x $1\mu m^2$ and 10 x10 μm^2. Inspection of the surface topology of the episurfaces showed the typical step-terrace pattern for 1 x $1\mu m^2$ images, indicative of good quality epitaxial growth, while the 10 x 10 μm^2 images showed long range mound roughness. These images were then statistically analyzed, once again using Fenner's approach, to obtain fractal parameters. Results of the statistical analysis of these images, i.e. auto-correlation, height correlation, and k-correlation, are summarized in Table 5.5.

Auto-correlation data and AFM images for 1 x $1\mu m^2$ and 10 x $10\mu m^2$ scan sizes of a typical episurface grown on a CMP finished surface are shown in the height and amplitude images of Fig. 5.23 a) and (b) respectively. (Note: The AFM generates a 'height' and an 'amplitude' image for each surface and some features are better discernable using amplitudes.) Figure 5.23 a) shows unevenly spaced steps and terraces that are not well formed while Fig. 15.23 b) shows larger steps and terraces with abrupt breaks. The auto-correlation fit for the 1 x $1\mu m^2$ image showed fractal behavior at short distances with $H_a = 0.85$ with correlation lengths $\xi_a = 5$ and 20nm for the short and long components respectively, in a two part correlation fit. Due to the unevenly spaced steps the autocorrelation function becomes noisy at larger dimensions. The 10 x 10 μm^2 image showed $H_a = 0.95$ and $\xi a = 850nm$ with a clear presence of mound roughness, fit to a first order Bessel Function [5.15], with an undulating surface exhibiting a mound roughness with a wavelength of ~3.5μm. Only the zero-order Bessel function was modeled, though using higher orders may improve the fit. The auto-correlation fit showed random fractal behavior at small dimensions and mound behavior for larger dimensions.

Table 5.5. Results of the statistical analysis performed on episurfaces grown on CMP and GCIB processed GaSb substrates.

MBE Run/ Sample #	*Surface Preparation Method*	*AFM Measurements*			*Auto-correlation*				*Height Correlation*		*k-correlation*		
		Image Size (μm^2)	*ΔZ (nm)*	*R_{rms} (nm)*	*H_a*	*ζ_a (nm)*	*Double Exponent*	*Mound Rough*	*H_d*	*ζ_d (nm)*	*Slope*	*H_p*	*B_p (nm)*
76-3	CMP	10 x10	5.06	0.80	0.95	820	0%	Yes	0.95	1000	-3.4	0.85	**2800**
76-1	CMP	1 x 1	0.86	0.10	0.85	8 50	80% 20%	Little	0.8	5	-2.3	0.85	**30**
77-4	GCIB S-008	10 x 10	2.68	0.35	1.0	850 40	88% 12%	Yes	1.0	680	-3.0	1.0	**1800**
77-2	GCIB S-008	1 x 1	0.95	0.12	0.55	15 30	75% 25%	Yes	0.7	11	-2.5	0.7	**65**
78-4	GCIB S-009	10 x 10	18.29	0.32	0.65	80 800	65% 35%	Yes	0.7	60	-2.3	0.65	**380**
78-6	GCIB S-009	1 x 1	1.39	0.18	0.35	3.5 9.0	40% 60%	Yes	0.2	11	-1.0	0.25	**45**
91-3-4	GCIB S-010	10 x 10	8.19	0.91	0.9	1200	0%	Yes	1.0	900	-2.2	0.25	**4500**
91-3-2	GCIB S-010	1 x 1	1.28	0.10	0.65	15	0%	Yes	0.6	17	-2.3	0.5	**80**
92-5-4	CMP S-012	10 x 10	9.07	0.86	1.0	750	0%	Yes	0.95	800	-2.8	0.65	**2900**
92-5-3	CMP S-012	1 x 1	0.9	0.11	0.6	12	0%	Yes	0.55	11	-1.7	0.25	**70**
92-6-1	GCIB S-012	10 x 10	11.48	2.04	0.8	1500	0%	Yes	0.85	1600	-2.8	0.65	**3200**
92-6-3	GCIB S-012	1 x 1	1.93	0.19	0.7	120	0%	No	0.80	70	-2.1	0.5	**500**
93a-3	CMP S-011	10 x 10	448.4	72.52	1.0	1050	0%	Yes	1.0	1110	-2.8	0.5	**3500**
93a-1	CMP S-011	1 x 1	28.56	3.17	0.9	78	0%	Yes	1.0	77	-2.3	0.25	**500**
94-4	GCIB S-014	10 x 10	125.7	10.25	0.6	1100	0%	No	1.0	1300	-2.0	0.2	**4400**
94-5	GCIB S-014	1 x 1	0.77	0.10	0.5	8.5	0%	No	0.45	8	-2.1	0.5	**60**
93b-1	GCIB S-011	10 x 10	167.6	21.72	1.0	480	0%	Yes	1.0	400	-3.4	0.9	**1500**
93b-2	GCIB S-011	10 x 10	163.6	23.40	0.95	730 400	50% 50%	No	1.0	390	-3.5	0.95	**1500**
93b-3	GCIB S-011	10 x 10	234.4	32.87	1.0	500 1350	60% 40%	Yes	1.0	500	-3.4	0.9	**2000**
93b-4	GCIB S-011	10 x 10	104.0	12.34	0.9	450	0%	Yes	1.0	330	-3.2	0.95	**1300**
93b-5	GCIB S-011	10 x 10	10.54	1.06	0.9	850	0%	Yes	0.95	900	-3.2	0.85	**2400**
93b-6	GCIB S-011	10 x 10	5.34	0.73	0.9	850	0%	Yes	0.95	800	-3.2	0.9	**2800**

A sectional cut diagonally across the AFM image of the CMP episurface, shown in Fig. 5.23 (a), was obtained such that the cross-section is perpendicular to the steps and terraces. The sectional cut is shown in Fig. 5.24 where the markers are located across eight subsequent terraces. The horizontal distance across twelve terraces was measured to be ~935nm ± 10nm, implying an average distance of ~117 ± 2nm between terraces. Also, the heights of the steps were observed to range between 2Å and 5Å with an average of ~3.5Å. Using simple trigonometry, the angle of the slice relative to the 100 plane was calculated to be ~0.17° ± 0.05°. As observed from the AFM image and the cross-sectional plot, the steps and terraces are not well formed, hence making them noisy. Figure 5.25 a) and (b) show the 1 x 1μm^2 and 10 x 10μm^2 AFM images respectively along with their auto-correlation data for epilayers grown on GCIB finished surface, sample #91-3. (Note: Refer to Table 5.4 for details on surface preparation method.)

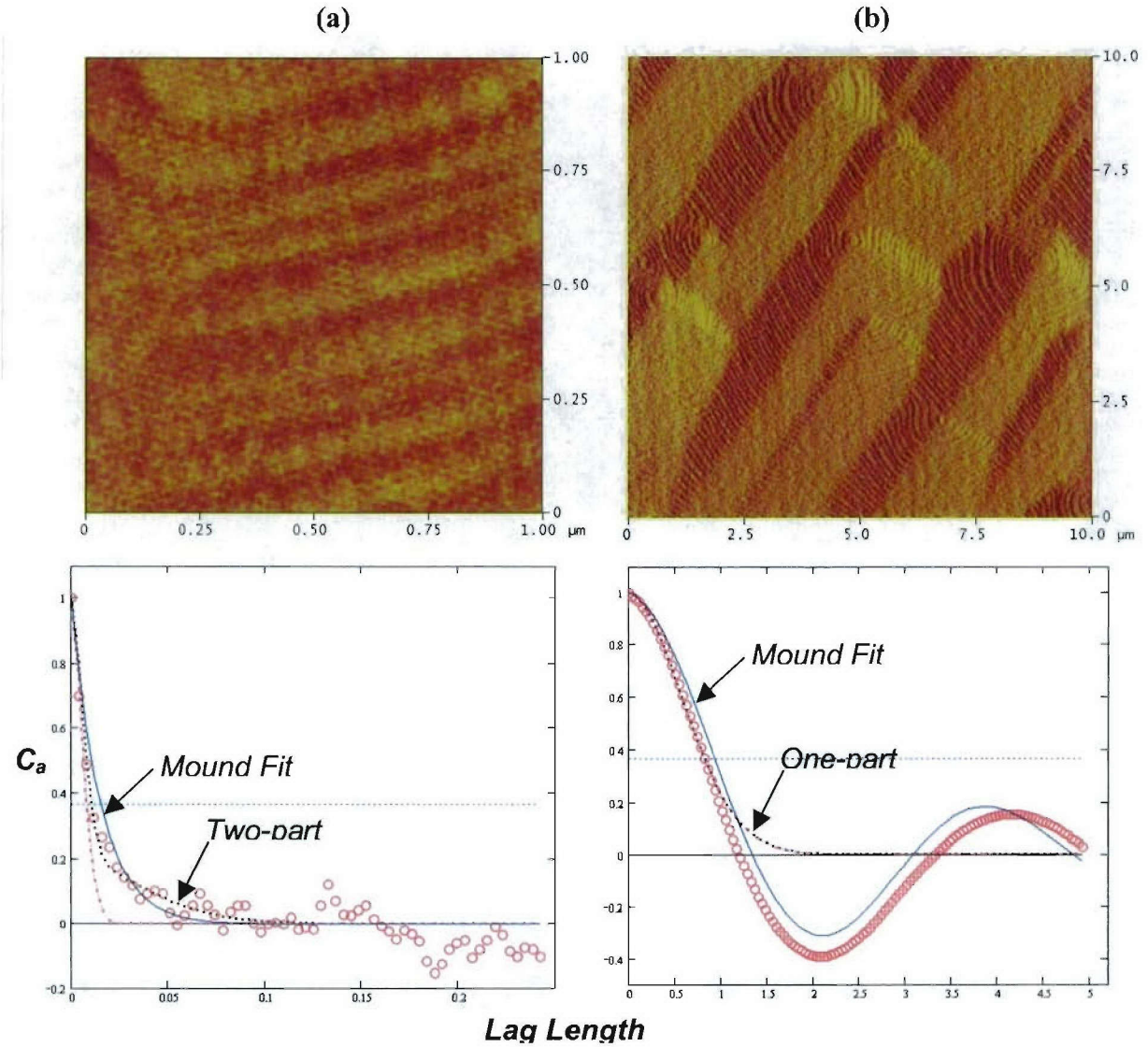

Figure 5.23. AFM images and auto-correlation fits for an episurface grown on a CMP (sample76) finished surface for: a) 1 x 1μm^2 and b) 10 x 10μm^2 scan images.

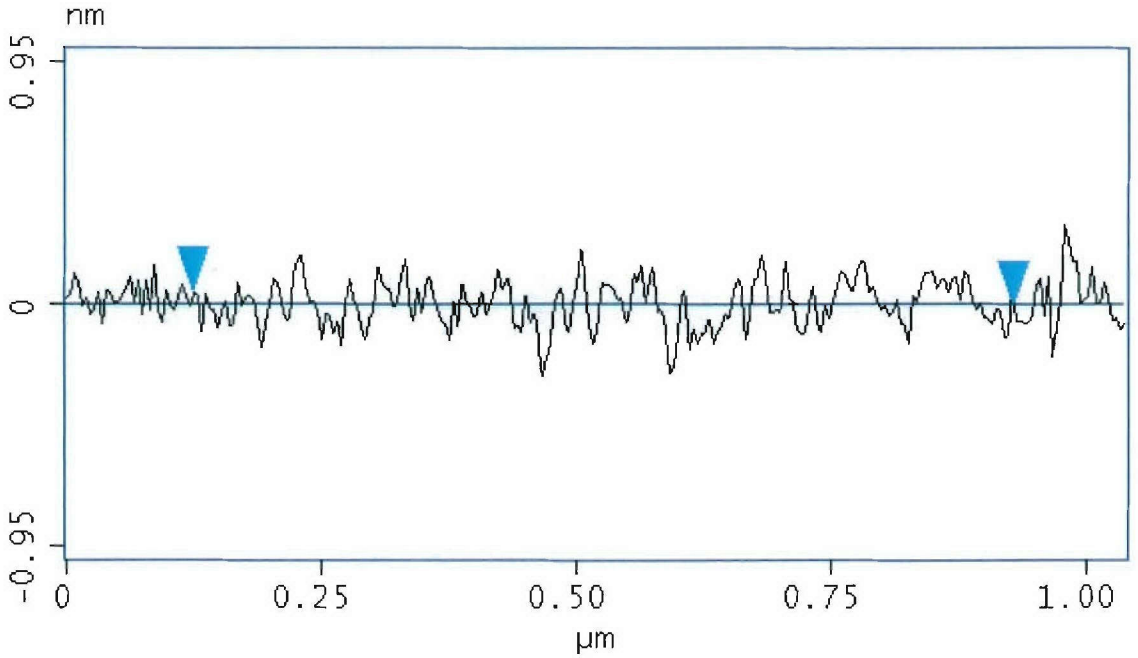

Figure 5.24. Height cross-section of an episurface grown on a CMP finished surface, shown in Figure 5.23 (a). The cross-sectional cut acquired was oriented perpendicular to the steps and terraces in the AFM image.

The 1 x 1μm^2 image showed a fractal parameter $H = 0.65$ with $\zeta_a = 5$nm while the 10 x 10μm^2 image showed $H = 0.9$ and $\zeta_a = 1200$nm. The auto-correlation data here clearly showed sharp fractal behavior over short dimensions as a consequence of cluster ion impacts with mound roughness over longer ranges due to the formation of steps and terraces. The steps and terraces are formed due to surface diffusion of atoms until they find an energetically favorable location. Thus the steps and terraces tend to wander due to the non-flatness or mound like behavior at larger scales during epitaxial growth. It was interesting to note that the periodic arrangement of the steps and terraces observed on the smaller scale images were all perpendicular to the mounds observed in the larger image. Also, it was observed that the larger scale image showed a slowly undulating surface with no abrupt edges.

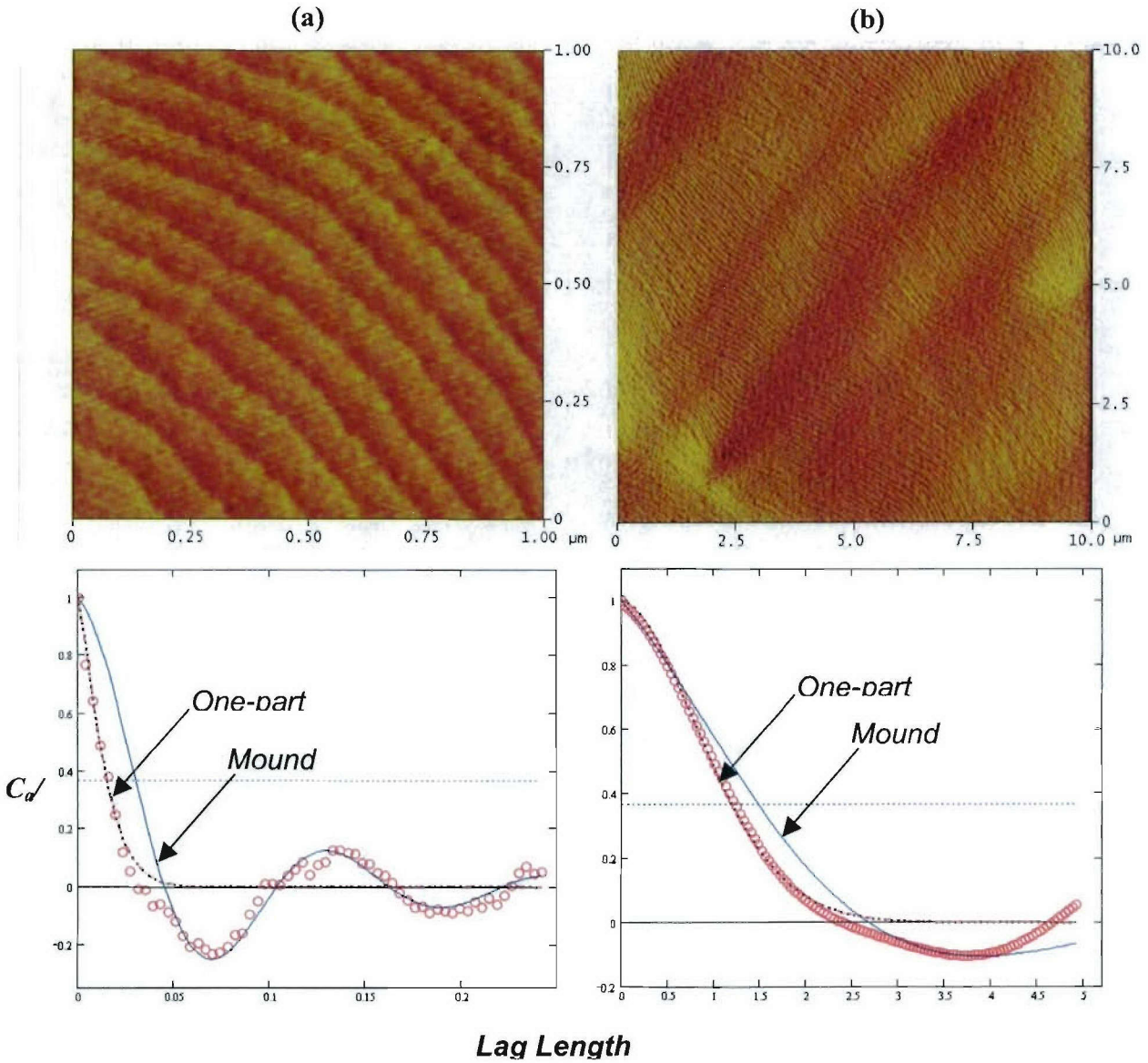

Figure 5.25. AFM images and auto-correlation fits for an episurface grown on a GCIB (sample 91-3) finished surface for: a) 1 x 1μm^2 and b) 10 x 10μm^2 scan images.

Epilayers grown on other GCIB surfaces showed similar characteristics, though their fractal parameters differed form each other, as shown in Table 5.5. Statistical analysis of epigrown surfaces on GCIB finished substrates showed the fractal parameter to be $0.35 < H_a < 0.7$ for 1 x1μm^2 scan size, i.e sharp fractals, while CMP surfaces showed less sharp fractal characteristics with $0.6 < H < 0.85$. In general, there is a good agreement between the auto-correlation and height-difference correlation data. The presence of mound roughness limits the fit quality of the *k*-correlation model data and hence these results are not reliable.

A sectional cut diagonally across the AFM image of the GCIB episurface, shown in Fig. 5.25, was obtained such that the cross-section is perpendicular to the steps and terraces. The sectional cut is shown in Fig. 5.26 where the markers are located across twelve subsequent terraces that were almost equidistant from each other. The horizontal distance across twelve terraces was measured to be ~1.2μm ± 0.1μm, implying an average distance of ~93 ± 2nm between terraces. Also, the heights of the individual steps were all between 3.4Å and 3.8Å. Using simple trigonometry, the angle of the slice relative to the 100 plane was calculated to be ~0.22° ± 0.01°. In general wider terraces with mono-atomic step heights are closer replications of the 100 surface as compared to surfaces that display narrower terraces and/or multi-atomic step heights. Comparing cross-sectional plots shown in Figs. 5.24 and 5.26, it can be seen that the steps and terraces are better formed, or at least less random, for episurfaces grown on GCIB as compared to CMP finished surfaces.

Since the quality of epi is a direct consequence of the initial surface condition, it is worthwhile to note that the all epitaxial layers grown on GCIB processed surfaces showed sharp fractal behavior over short-range roughness while exhibiting mound

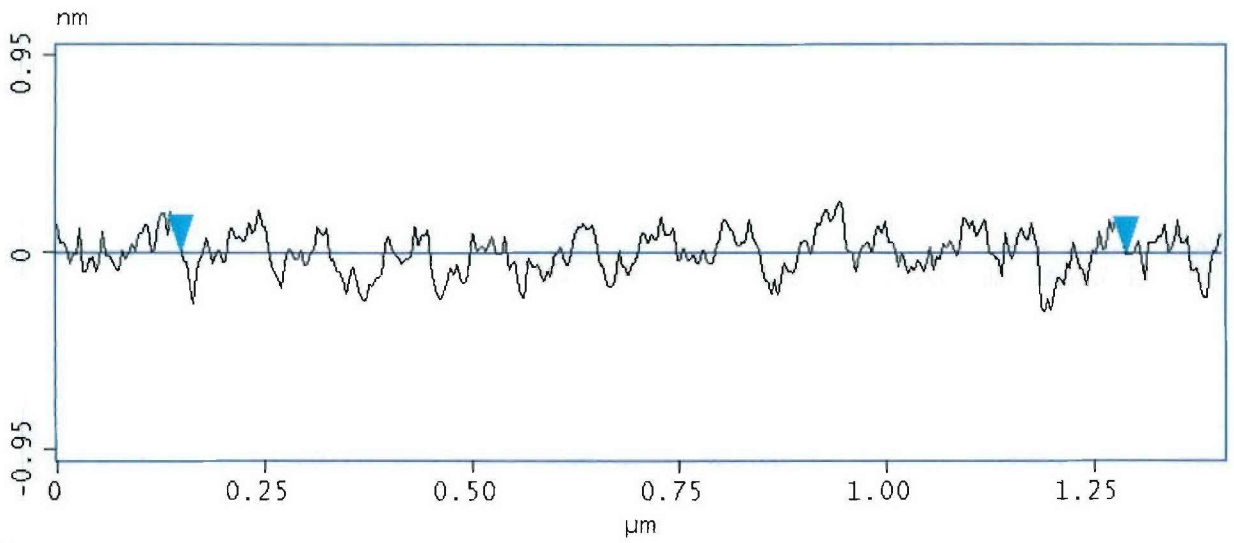

Figure 5.26. Height cross-section of an episurface grown on a GCIB finished surface, shown in Figure 5.25 (a), where the cross-section was acquired diagonally across the image with the steps and terraces perpendicular to the cut.

behavior over larger dimensions. The sharp fractal roughness is usually found on the terraces as a result of the cluster ion impacts (from GCIB processing) during surface preparation. The mound roughness is due to the formation of steps and terraces as the growth progresses on a substrate that is cut slightly off the 100 direction, which is usually an angle less than 0.5°. An analysis on episurfaces grown on CMP surfaces was inconclusive, sometimes showing the presence of steps and terraces in some areas while not in other areas. Comparing the initial substrate roughness parameters to those of the final episurfaces, it could be seen that samples 77 and 78 showed two-part correlation fit while samples 91 – 94 showed a single-part correlation fit. Here too, the short range correlation component in C_a usually leads to fractal like behavior.

The substrate surface for sample 93(a) and (b) was lost during epitaxial growth yielding an extremely pitted surface with small patches that appeared to be defect free. The sequence of AFM images on a 10 x 10μm^2 scale, samples 93b-1 to 93b-6, were obtained sequentially from the pitted region to the defect free region showing a decrease in pit density as well as a decrease in the magnitude of the pits. However, due to the damaged nature of the surface, statistical analysis of this sequence of images did not show any particular trend in fractal parameters and correlation lengths. Similarly, due to the damaged nature of the surface, 1 x 1μm^2 AFM images showed severe inconsistencies during acquisition and hence were not statistically analyzed.

Based on the current analysis, the auto-correlation with exponential and Bessel functions for quantifying fractal and mound roughness respectively, may be good methods of determining the quality of crystal growth. In addition, cross sectional plots of the steps and terraces provide dimensions. Wider terraces with mono-atomic step heights are closer replications of the 100 surface as compared to surfaces that display narrower terraces and/or multi-atomic step heights. Also, based on the dimensions of the steps and terraces the orientation of the growing surface, i.e. angle of miss-cut from the 100 orientation, can be ascertained.

To summarize the GCIb fractile section, the fractal parameters H and ζ can be independently obtained by statistically analyzing each of the three correlation functions – auto-correlation, height-correlation, and power spectral density distribution. Each of these functions provide insight into different aspects of the surface. Statistical analysis showed that all CMP and GCIB surfaces exhibited random fractal behavior with $0.8 < H_a < 1.0$ obtained by fitting data to the he auto-correlation function. A simplified auto-correlation fit to a first order Bessel function provides information on the mound roughness, though the use of higher orders could improve the overall fit. In addition, it also showed that two-part fits were required on surfaces that were initial rougher, where the short range component provided the fractal information. The height-difference correlation showed that smaller energy smoothing steps resulted in smaller correlation lengths (ζ_d), corresponding to larger residual roughness. This confirmed the need for multi-energy GCIB process with sequentially lower energies for smoothing.

Data fit to the PSD function showed that the GCIB smoothing was effective over a range of spatial frequencies, corresponding to wavelengths of 50nm to 5μm. The effect of GCIB processing rapidly diminishes for lower frequencies while it is limited on the higher end by the roughness caused by cluster ion impacts

.

Analysis of the episurfaces showed a good fit for the first order Bessel function for all epilayers grown on GCIB finished surfaces due to the presence of uniform step-terrace patterns. Data fits to the auto-correlation function also showed fractal behavior over small ranges, i.e. on the terraces, essentially due to overgrowth on cluster impacted surfaces. Epilayers grown on CMP finished surfaces did not show uniform step-terrace patterns resulting in extremely poor fits to the first order Bessel function.

5.3.6 SIMS Analysis of Epilayer/Substrate Interface

With the help of Dr. G. Turner's group at MIT Lincoln Laboratory secondary ion mass spectrometry (SIMS) profile measurements were made on an overgrown CMP polished sample (03-076) and the oxygen GCIB sample (03-077) discussed above. As shown in Table 5.6, a number of impurities at the epi/substrate interface were tracked besides the crystal constituents. As shown in the table impurities are measured at levels up to $10^{20}/cm^3$ for oxygen at the epilayer substrate interface.. The oxygen level indicates that the oxide layer did not fully desorb, a fact corroborated by the XTEM results. Also note carbon was found at the interface with a level of about $3 \times 10^{19}/cm^3$.

Element	CMP (Atoms/cm3)	O2-GCIB (Atoms/cm3)	Detection Limit in GaSb (Atoms/cm3)
C	1.9 x 1020	3.6 x 1016	3.0 x 1014
O	1.3 x 1019	7.6 x 1019	9.0 x 1016
Be	2.8 x 1020	1.2 x 1019	5.0 x 1016
S	8.3 x 1016	1.6 x 1018	4.0 x 1015
Si	1.7 x 1018	1.2 x 1019	1.0 x 1015
Cl	9.0 x 1017	5.9 x 1016	3.0 x 1015
W	2.7 x 1018	2.0 x 1019	3.0 x 1017
In	2.4 x 1017	1.8 x 1017	- NA -
Fe	1.8 x 1016	2.2 x 1016	1.0 x 1015
Ni	1.6 x 1016	3.8 x 1016	6.0 x 1015

Table 5.6. Elements with their concentration levels found at the Epilayer/substrate interface. CMP is compared to O_2 GCIB processed surfaces. Note that the detection limits for each element is also given in the table.

Of the impurities shown in Table 5.6, we suspect that the tungsten at the interface is real and probably introduced in the GCIB process (due to the filament). New components for the GCIB instrument can be developed to eliminate this problem.

SIMS profiles of the CMP overgrown sample are similar to those of the GCIB sample with several exceptions. The level of carbon at the interface of the CMP sample is about an order of magnitude greater that of the GCIB sample. The GCIB sample, however has more oxygen at the interface. Other impurities such as sulfur are also a bit higher in the GCIB sample as compared to the CMP sample. Our interpretation of the SIMS observations are two-fold. First, the high oxygen content of the GCIB sample leads us to believe that the current GCIB recipes have not fully produced the appropriate oxide on the surface for MBE. Second, since a multiuse, research GCIB instrument was used in these experiments, cross-contamination is an issue. This problem can be solved with dedicated equipment.

5.3.7 HBr GCIB Results

Although a number of GCIB processes look promising, all the work done under this contract show interface defects by XTEM. From the Br-IBAE experiments that will be discussed below we have found that a surface layer of Bromine seems to promote a high-mechanical-quality interface. Under a Phase I SBIR spin-off of this work with Galaxy in the lead (AFOSR contract number FA8650-04-19-5426) a subset of the team, Galaxy, Epion, and UMass was able to HBr-GCIB process several GaSb wafers in one of Epion's research GCIB systems. Subsequent overgrowth experiments demonstrated that GCIB could produce a defect free epi/substrate interface. The reader is advised to obtain a copy of the Phase I final report for the details of these experiments.

5.3.8 GCIB Polish Summary

Amongst the various GCIB processes, investigated as a final polish for producing epiready GaSb surfaces, the dual energy step GCIB processes incorporating a high energy (10keV) etch step followed by a low energy smoothing step (3keV) with ion fluences in the range of ~10^{15} and 10^{16} ion/cm^2, resulted in the production of surfaces with the least amount of residual roughness. When these processes were evaluated by growing epitaxial layers over the surfaces, some of the processes showed significant reductions of the defects at the epi/substrate interface as compared to the overgrowth of CMP surfaces. Using the ABCS work as a starting point an SBIR Phase I effort lead by Galaxy Compound Semiconductors, Inc. demonstrated that the HBr-GCIB recipe produced a final polish with no defects at the epi/substrate interface.

In summary, a method of post processing CMP finished GaSb wafers has been developed, advancing the state-of-the-art one step closer to being able to produce "epi-ready" GaSb wafers. As part of this work, chemical and thermal models were proposed to understand the formation of oxides and to understand the observed improvement in sub-surface crystallinity. In addition, a new method for characterizing the roughness of the substrate/oxide interface was demonstrated. Oxide desorption and epitaxial growth on GCIB finished GaSb surfaces was demonstrated for the first time showing improvement over CMP finished surfaces. Finally, fractal analysis of surfaces and interfaces, in conjunction with other surface and interface measurements, provided valuable insight into the physical and chemical reactions occurring on the surface during GCIB modification, leading to the formation of a surface oxide layer.

5.3.9 Reference

5.1 Kannan Krishnaswami, Preparation of epiready GaSb substrates with gas cluster ion beams," Ph. D. Thesis , University of Massachusetts Lowell (Prof. Goodhue Advisor) 2004.

5.2 Yamada, J. Matsuo, N. Toyoda, A. Kirkpatrick, "Materials processing by gas cluster ion beams," Materials Science and Engineering, Vol. R 34(6), 231 (2001).

5.3 L.P. Allen, D.B. Fenner, C. Santeufemio, W. Brooks, E. Degenkolb, V. Difilippo, J. Hautala, A. Kirkpatrick, "Substrate smoothing using gas cluster ion beam processing," Journal of Electronic Materials, Vol. 30(7), 829-833 (2001).

5.4 L.P. Allen, D.B. Fenner, C. Santeufemio, W. Brooks, J. Hautala, Y. Shao, "Nano-scale surface texture by impact of accelerated condensed-gas nanoparticles", Proceedings of SPIE, Vol. 4806, 225-232 (2002).

5.5 L.P. Allen, Z. Insepov, D.B. Fenner, C. Santeufemio, W. Brooks, K.S. Jones, I. Yamada. "Craters on Si surfaces created by gas cluster ion impacts," J. Appl. Phys., Vol. 92(7), 3671(2002).

5.6 D. Fathy, O.W. Holland, R. Liu, J. Wosik, W.K. Chu, "Cluster ion beam smoothing of SiC and YBCO surfaces," Materials Letters, Vol. 44(3-4), 248-252 (2000).

5.7 N. Toyoda, "Nano-processing with gas cluster ion beams", 1999 Ph.D. Thesis, Department of Nuclear Engineering, Kyoto University, Kyoto, Japan.

5.8 W.D. Goodhue, Y. Royter, D.E. Mull, S.S. Choi, and C.G. Fonstad, "Bromine Ion-Beam Assisted Etching of III-V Semiconductors," *Journ. Electron. Mater.* **28**, 364 (1999).

5.9 K.F. Longenbach and W.I. Wang, "Molecular beam epitaxy of GaSb," Appl. Phys. Lett., Vol. 59(19), 2427-2429 (1991).

5.10 P. Atkins and J. de Paula, Physical Chemistry, Seventh Edition, W.H. Freeman and Company, New York, NY (2002)

5.11 Standard thermodynamic properties of chemical substances, CRC Press (2000)

5.12 R. Lowery, C. Mallika, and T.J. Anderson, "Potentiometric Determination of the thermodynamic stability of SB2O3," Annual Meeting of the Minerals, Metals, and Materials Society (1997); http://www.tms.org/Meetings/Annual-97/Program/Sessions/WP240A.html.

5.13 D.B. Fenner, "Fractal topography of surfaces exposed to gas cluster ion beams and modeling simulations," J. Appl. Phys., Vol. 95(10), 5408-5418 (2004).

5.14 K. Krishnaswami, D.B. Fenner, S.R. Vangala, C. Santeufemio, M. Grzesik, and W.D. Goodhue, "Roughness analysis of ion beam processed GaSb and InSb surfaces," Materials Research Society Conference, Boston, Massachusetts (2004).

5.15 G. Palasantzas and J.T.M. De Hosson, "Mound surface roughness effects on the thermal capacitance of thin films," J. Appl. Phys., Vol. 89, pp. 6130-6134 (2001).

5.4 Bromine Ion-Beam Assisted Etching as a Final GaSb Polish

5.4.1 Bromine Ion Beam Assisted Etching Overview

Over the last ten years Goodhue has developed a bromine ion-beam etching (Br-IBAE) system capable of etching most III-V compound semiconductor materials [5.8]. His original work was done at MIT Lincoln Laboratory. About two years ago one of Goodhue's Lincoln IBAE systems was offered to the UMass Lowell Photonics Center. The system was refurbished at the Photonics Center and began operation about 6 months into this contract. Bromine IBAE, shown schematically in Fig. 5.27, consists of a bromine jet and a Kauffman ion gun housed in a high vacuum system. The UMass Lowell implementation also has a load lock for sample insertion. The Kauffman gun produces an argon ion beam that impinges on the non-masked portion of the sample, causing very shallow damage that breaks surface bonds. Bromine, from the jet reacts on the surface with the material forming volatile bromides. The bromides evaporate from the surface, thereby removing material from the sample. The process is extremely anisotropic with a number of parameters that can be varied to produce optimal etching. These parameters include substrate temperature, bromine flow, and argon beam energy and current.

Typically the etching of GaSb, GaAs and InP require an argon ion beam energy of about 600 V with a current density of 20 $\mu A/cm^2$. The UMass system had a gun beam diameter of 2.5 cm. Bromine flow is measured by swinging a baratron tube in front of one of the two bromine jets and reading the pressure. About 0.6 to 0.9 mTorr of bromine at the jet is sufficient. Although GaSb is currently etched at room temperature, a stage is being developed to etch the material at temperatures down to 77K. GaAs is etched at between 50° and 70° C while InP is etched at 180° C. Typical etch rates are 400 nm/min, 80 nm/min and 50 nm/min for GaSb, GaAs and InP respectively at their various substrate temperatures.

As shown in Fig. 5.28, Br-IBAE is capable of anisotropically etching GaSb. Furthermore, the quality of the etched surface is a strong function of the initial surface. The material used to etch the wafer in Fig. 5.28 was polished too aggressively, and the polish damage is easily seen in the etched surface. High-quality GaSb surfaces have also been etched and yield high-quality mirror-like surfaces. For more details on this work see S. Vangala's M.S. thesis [5.16].

As part of the first year effort both high quality and poor quality CMP surfaces were Br-IBAE etched and X-ray analysis performed to determine the surface and subsurface damage caused by the etching. Figure 5.29 a) shows a phase-contrast optical micrograph of the surface of an etched high quality CMP polished GaSb substrate and b) the (400) and (111) X-ray rocking curve full-widths at half-maximum data for the surface at various etch depths. The data remains near the theoretical limits of about 14 arc-seconds for the (400) full-width at half maximum and 20 arc-seconds for the (111) full-width at half-maximum. On the other hand, a poorly CMP polished wafer was also etched with the results shown in Fig. 5.30. As one sees in the optical phase-contrast micrograph, Fig. 5.30 a) polish damage is clearly evident. The X-ray data also shows that

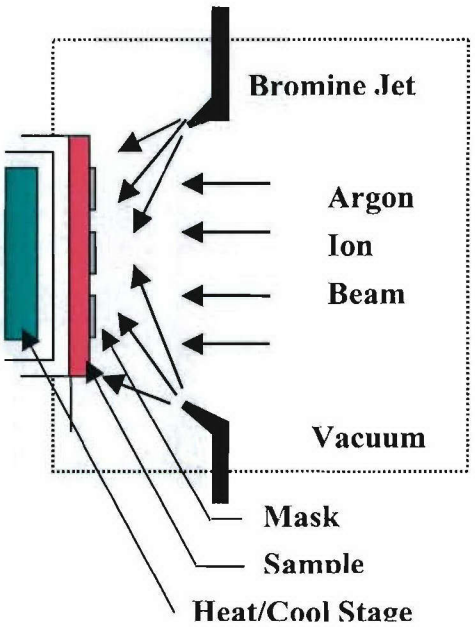

Figure 5.27. Schematic diagram depicting a bromine ion-beam-etching system.

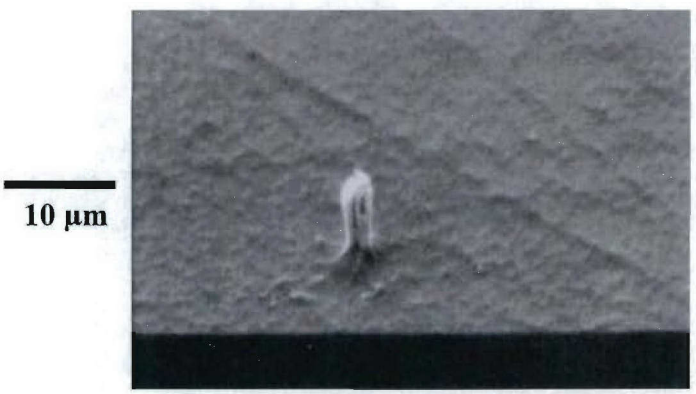

Figure 5.28. Scanning electron micrograph of a Br-IBAE etched GaSb wafer. This wafer was poorly polished and the etching has reveled polishing scratches and damage. Note that the micro-masked mesa shows the etching to be very anisotropic.

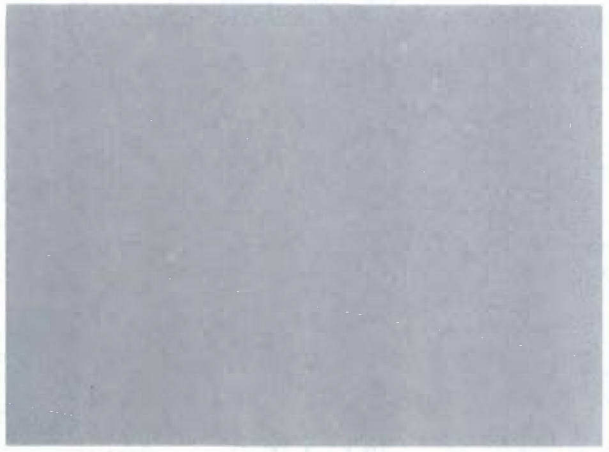

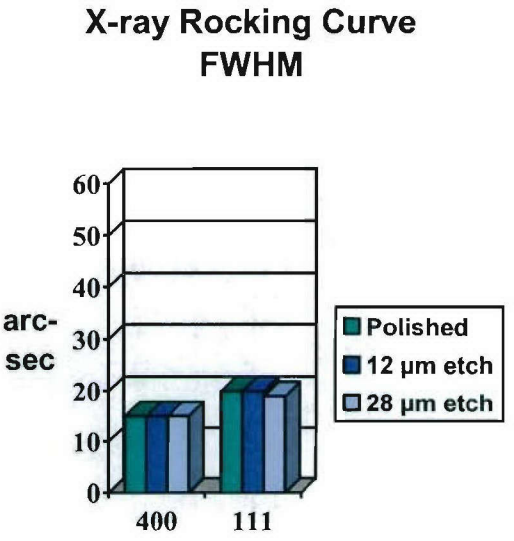

(a) (b)

Figure 5.29. Part a) is an optical phase-contrast micrograph of a high quality CMP GaSb surface which has been Br-IBAE etched 12 micrometers deep. The X-ray rocking curve full-width at half-maximum data b) for the (400) and (111) orientations show that the crystal remains undamaged after etching.

the damage is extensive, Fig. 5.30 b). On the other hand, Br-IBAE was able to remove a significant amount of the surface damage. One sees that the (111) rocking curve data is more sensitive to wafer problems. This is due to the fact that the X-ray probe for the (111) direction is incident on the surface with an angle of 83.5 degrees with respect to the normal, and therefore samples a large area of the surface. In this particular case, the large half-widths are attributable to the surface. The (111) probe is also sensitive to wafer stress and to back surface problems which induce stress in the front surface. In fact the techniques makes a good wafer qualification technique. Wafers with large (111) full-widths at half-maximum should be avoided as epitaxial growth substrates.

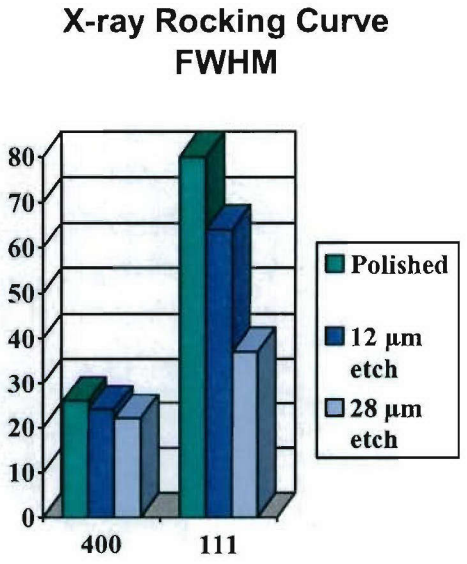

(a) (b)

Figure 5.30. Part a) is an optical phase-contrast micrograph of a poor-quality CMP GaSb surface which has been Br-IBAE etched 12 micrometers deep. The X-ray rocking curve full-width at half-maximum data b) for the (400) and (111) orientations show that the crystal remains damaged after etching.

5.4.2 Bromine Ion-Beam Assisted Etched Surfaces

Br-IBAE etched GaSb wafers can be inserted directly into a molecular beam epitaxy machine and overgrown with epitaxial GaSb. The epitaxial layers exhibits good photoluminescence at 77K and produce a substrate/epi interface which is not detectable by transmission electron microscopy.

What we consider high quality GaSb wafers with surfaces produced by chemical mechanical polishing [with (400) and (111) X-ray diffraction measurements] were etched with Br-IBAE. Typical surfaces of the pre and post -etched wafers are shown in Fig. 5.31. Note that although the scratches are removed with the Br-IBAE process, the rms

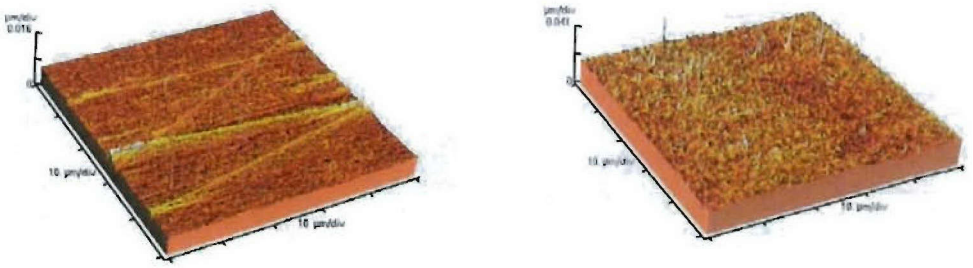

(a) (b)

Figure 5.31. a) AFM of a pre-etched sample with rms roughness of 1.2 nm. b) AFM of the post-etched sample with rms roughness of 2.3 nm.

roughness is increased by about a factor of 2. Although the etched surface is a bit rougher, the method is expected to produce a surface with significantly less damage than the original CMP surface. At this point we thought that the increased roughness would make IBAE final polishing unattractive. We were wrong. The MBE process tends to planarize the surface during the initial phase of epitaxial growth (see Section 5.4.4).

5.4.3 Surface Oxide Formation Using Br-IBAE

To quantitatively measure the thermal properties of the oxide produced with Br-IBAE we were fortunate to have access to Hanscom/AFRL's X-ray photoelectron spectrometer and surface scientist, Helen Dauplais. Figure 5.32 (repeated here) shows the antimony oxide behavior of a typically etched sample as a function of temperature. As one sees from the figure, the antimony oxides are liberated at 500 degrees C. Using Br-IBAE gallium oxides are also formed first with the gallium oxides finally disappearing at about 530 degrees C (Fig. 5.33 tracks gallium up to 500 degrees C). XPS spectra showing the Bromine behavior are given in Fig. 5.34. Note that as shown in Fig. 5.34 a) carbon is very tenacious at the surface.

One interesting feature that was found on the surface was a partial layer of bromine. This layer is interesting in that Miller et al [5.17] have shown in GaAs MBE using a carbon tetrabromide doping source that bromine may be beneficial to the GaAs layer. Our feeling is that the bromine may also be beneficial to the interface and first few monolayers of GaSb growth in our samples. Since the temperature desorption profiles seem ideal for MBE growth, samples were mounted on molly blocks with indium and transferred into the MBE for GaSb overgrowth. We have overgrown three samples to date. All were overgrown after IBAE and spending several weeks in plastic dishes. One was rinsed in methanol just prior to growth to try to remove the surface bromine layer.

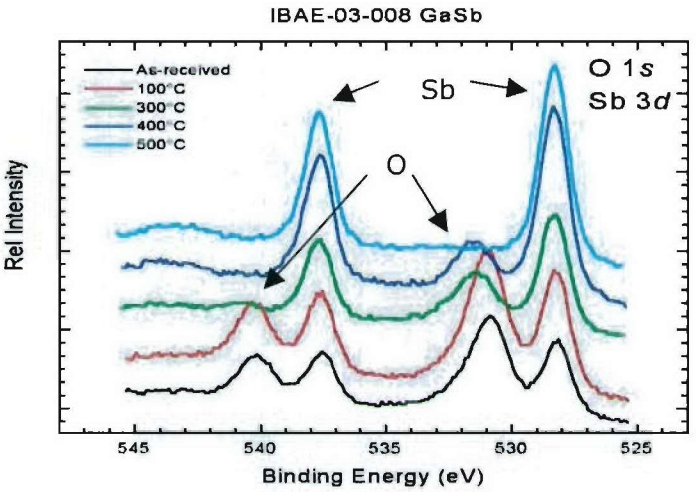

Figure 5.32. XPS spectra of antimonmide and antimonide oxides formed on GaSb during Br-IBAE. Note that as the temperature is raised in this ultra-high vacuum XPS system that the antimony oxides are completely desorbed at 500 degrees C.

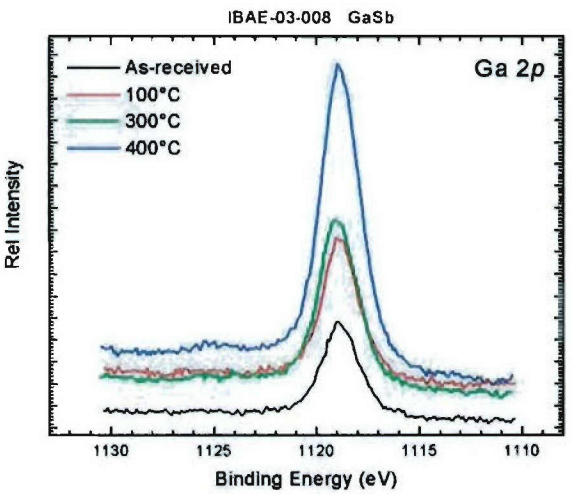

Figure 5.33. XPS spectra showing the evolution of gallium on the surface of a Br-IBAE etched sample as a function of temperature. Note that as the temperature is raised the gallium peak increases.

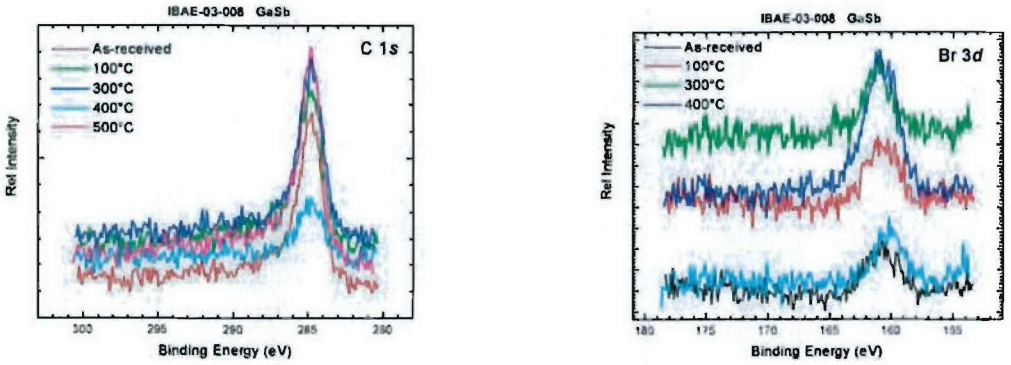

(a) (b)

Figure 5.34. Part a) XPS spectra showing the evolution of surface carbon as a function of substrate temperature. Part b) XPS spectra showing the evolution of residual bromine formed on the GaSb surface during Br-IBAE as a function of temperature. Note that as the temperature is raised in this ultra-high vacuum XPS system that the bromine remains on the surface. The bromine may be helpful in promoting a high-quality interface between the wafer and the epilayer.

5.4.4 MBE Growth over Br-IBAE Surfaces

RHEED observations on the samples while the oxide layers were being thermally desorbed showed that the layers desorbed in a straight-forward manner at 510 to 525 degrees C (on our substrate thermocouple), producing bright, nearly streaky patterns. The patterns were as good as those achieved with bromine based wet-etch surface preparation. As discussed above for the GCIB samples, the epilayers were grown with GaAsSb marker layers to track anomalies in the grown and to demark the interface. An XTEM of one of the samples (03-080) is shown in Fig. 5.35. Note that unlike the GCIB samples and CMP samples no discernable interface is present. Furthermore, the interface at the first GaAlSb marker layer appears to be very smooth.

Photoluminescence was also performed on a methanol rinsed (03-079) and unrinsed sample (03-080). Photoluminescence spectra at 77K was only obtainable for the unrinsed sample, 03-080. The 77K PL spectrum of 03-080 is shown in Fig. 5.36. Typical epitaxial spectra from CMP and IBAE prepared substrates are shown in Fig. 5.37. We suspect that there is some heating of the surface of the sample by our 17 mW helium-neon laser, since the peak position is consistent with a value calculated using a temperature of 80K. From this work we feel that Br-IBAE may play a major role as a final polish to produce "epi-ready" GaSb wafers as well as a preparation technique for producing GaSb based quantum dot and wire structures.

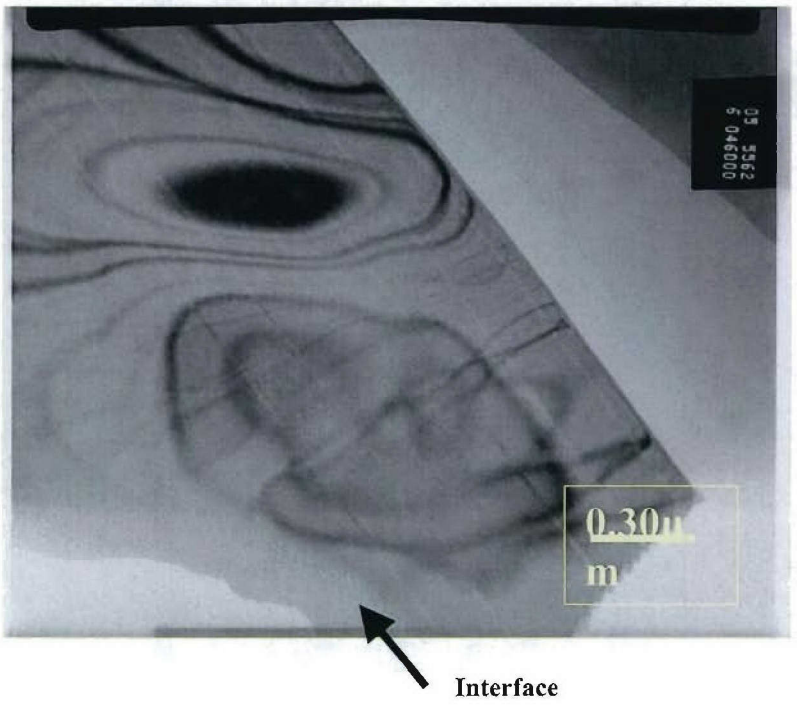

Figure 5.35. TEM micrograph of a Br-IBAE etched sample overgrown in the UMass MBE system. Note that there is no residue at the epi-substrate interface and that the GaSb/AlGaSb interfaces are smooth.

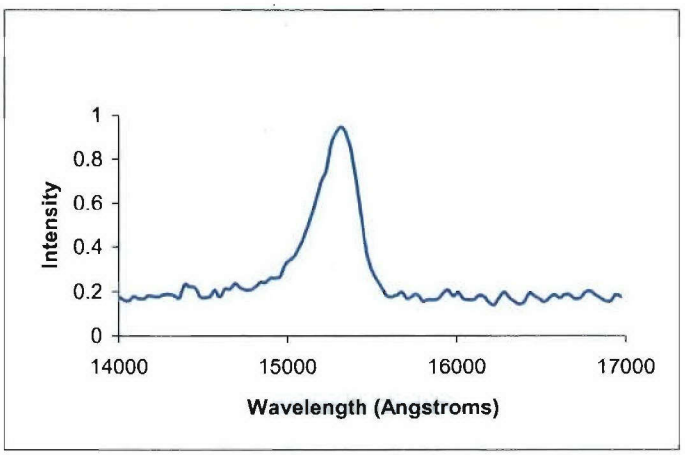

Figure 5.36. Photoluminescence spectrum of GaSb sample 03-080 at 77K. The surface of this sample was not intentionally modified between the time it was removed from the Br-IBAE system and loaded in the MBE system for overgrowth.

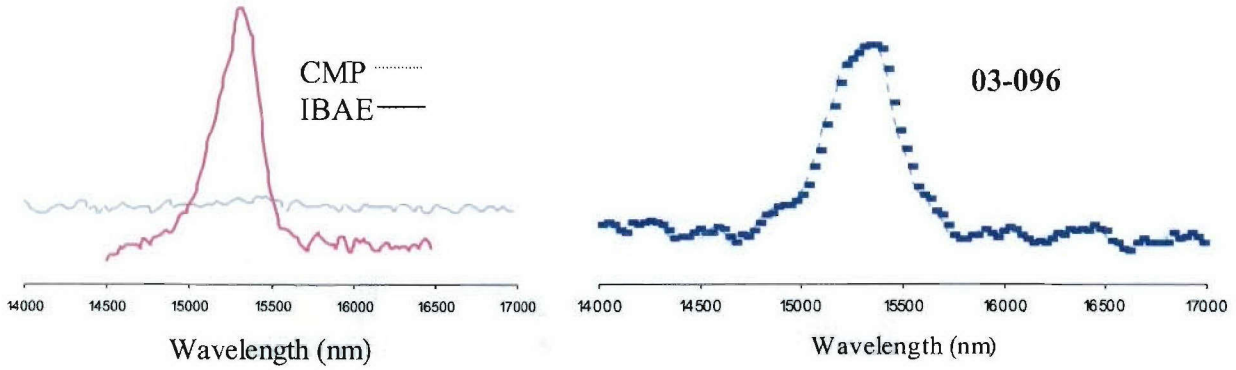

(a) (b)

Figure 5.37. Part a) compares typical 77 K PL spectra from epilayers grown on CMP and Br-IBAE prepared GaSb surfaces. Part b) is the 77 K PL signal from the epitaxial layer grown over a deep IBAE etched GaSb substrate.

AFM images of the epitaxial surfaces were obtained to further evaluate the quality of the epitaxial surfaces and growth characteristics of the GaSb layers on CMP and IBAE processed substrates. For these experiments, samples numbered MBE-03-076, MBE-03-079, and MBE-03-080 were used. The first sample was a CMP, and the rest were IBAE processed GaSb wafers that were used for epigrowth. As seen from the TEM images, CMP epigrown structures had interface defects while post-processed wafers had transition free interfaces. The epilayers on IBAE processed wafers exhibited higher roughness components due to the presence of particle like features referred to as protrusions. Fig. 5.38 shows images from the three surfaces on both 1x1 μm^2 and 10x10 μm^2 scales with respective Ra and Z range values. The AFM image statistics are given in Table 5.7. The evolution of the underlying Br-IBAE processed surface epi surface was unidirectional and one can see the terrace step formation in a single direction, in contrast to the random step terrace formation on a CMP wafer. This clearly indicates that CMP wafers were not suitable for epitaxial growth, though they yielded better surface roughness components. PSD comparisons also showed the reproducibility of surface characteristics on IBAE- processed substrates. Both samples, numbered 03-079 and 03-080 had similar roughness components, and the spectrum distribution was overlapping on both scales.

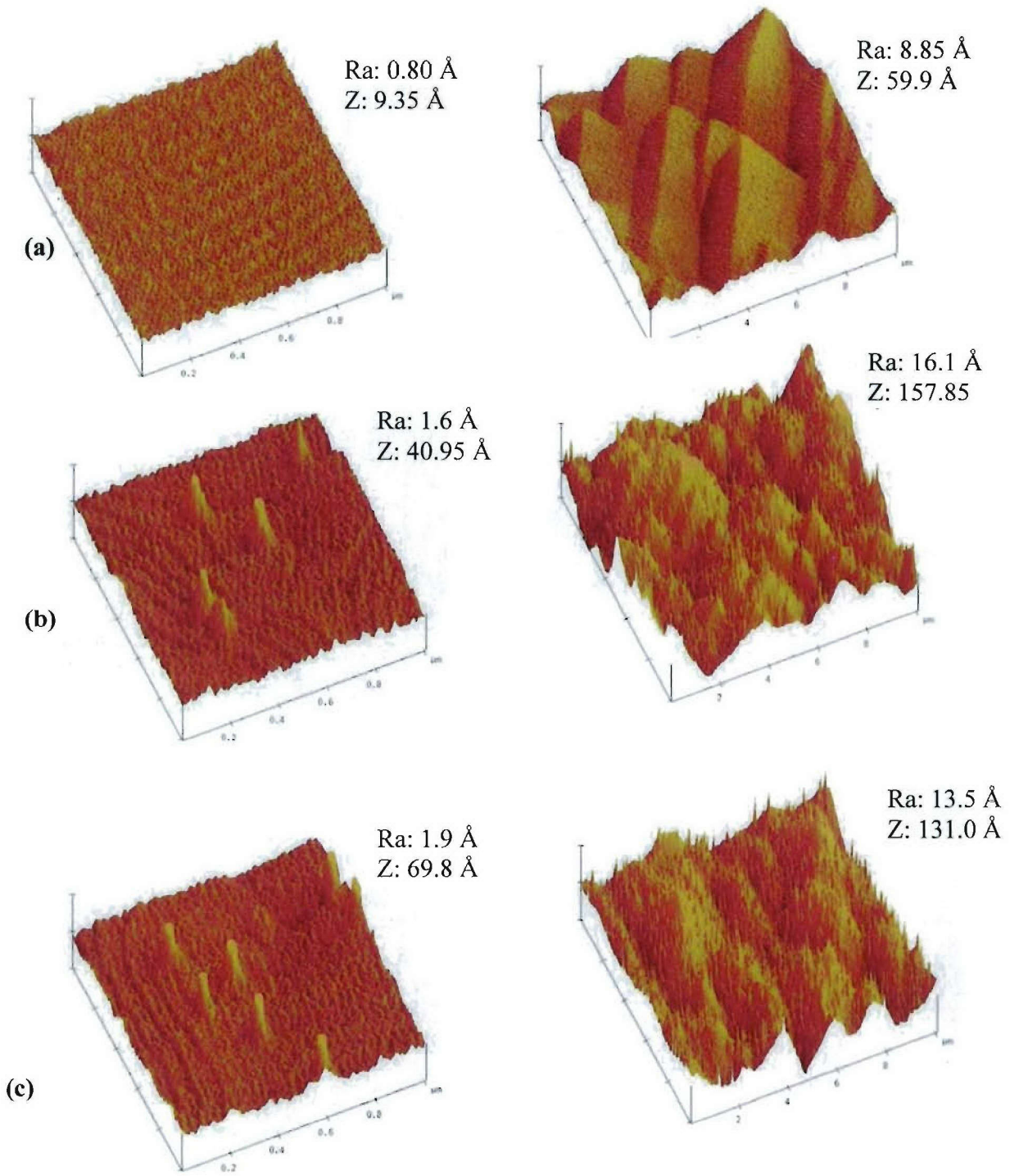

Figure 5.38. AFM images of the epitaxial layers grown on a) CMP [MBE-03-076] b) IBAE processed [MBE-03-079], and c) IBAE processed [MBE-03-080] substrates with their roughness components. Left images are 1x1 μm^2 and right images are 10x10 μm^2 size.

Table 5.7 Roughness measurements of epigrown material on CMP and IBAE processed substrates

Sample #	Process Details	AFM measurements (1x1 μm^2) Å			AFM measurements (10x10μm^2) Å		
		Rms	Ra	Z	Rms	Ra	Z
MBE-03-076	CMP	1.0	0.80	9.35	7.05	8.85	59.9
MBE-03-079	IBAE	3.0	1.60	40.95	20.70	16.10	157.85
MBE-03-080	IBAE	3.35	1.90	69.80	16.8	13.5	131.0

Careful measurements of the surface topology of epilayers grown on Br-IBAE processed GaSb surfaces showed the protrusions to be concentric pyramid-like structures with sharp points at their apexes (shown in Fig. 5.38 (b), viewed on a 1 x 1 μm^2 scale).

5.4.5 Fractal Analysis of Oxide and Overgrown Br-IBAE Surfaces

Autocorrelation data (also known as height-height correlation) obtained using the fractal code was best fitted with the phenomenological expression for both CMP and IBAE surfaces. The Hurst's component for the CMP surfaces was 0.9 with correlation length of 175 nm, while Hurst's component for the IBAE surfaces was 1.0 with correlation length of 340 nm. This increase in correlation length is, as expected, due to identical ions forming similar craters on the surface of GaSb which are distributed throughout as compared to the random nature of the CMP process.

In Fig. 5.39, the dashed line represents a one-part Gaussian correlation fit. A mound correlation decay model was also fitted (solid line in Fig. 5.39) to see the mound roughness nature of the actual data line referred, and it was evident that mound nature was not largely seen for these surfaces.

Height-difference correlation function was evaluated and fitted to the statistical Equation by varying H_d and ζ_d. Fig. 5.40 shows the height-difference correlation function. Hurst's components obtained from the best fit were 1.0 and 0.95 for CMP and IBAE surfaces respectively while the correlation lengths measured 117 nm and 325 nm. respectively. These measurements were in good agreement with the autocorrelation data. Also, it can be seen that the Br-IBAE surface showed an order-of-magnitude increase in

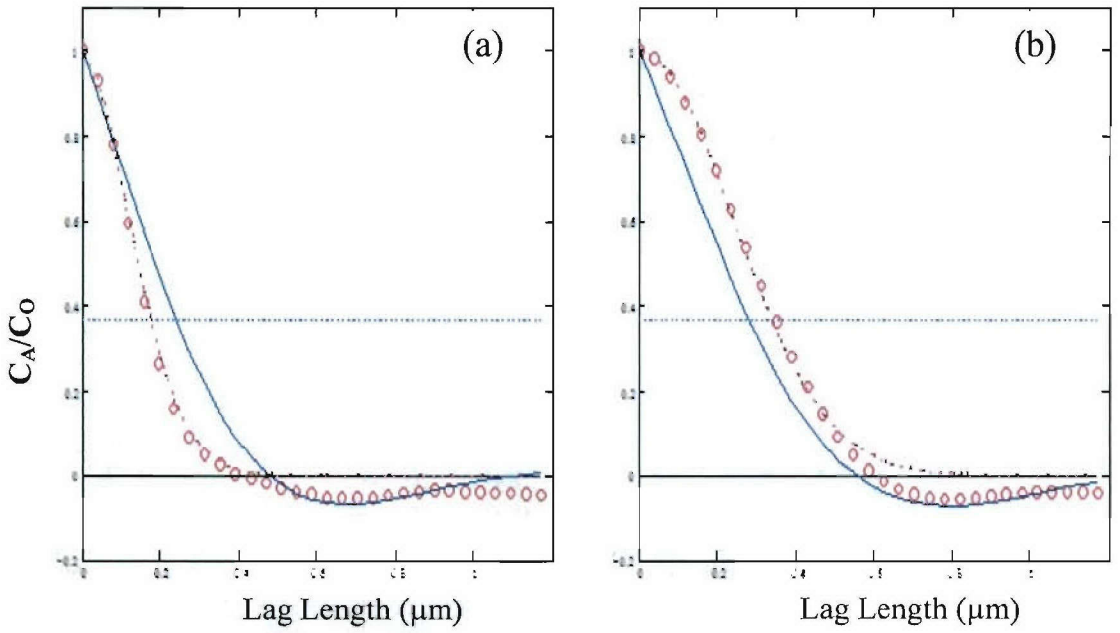

Figure 5.39. Autocorrelation data obtained for (a): CMP and (b): IBAE surfaces; dashed line refers to one-part fit with the actual data shown by circles and the solid line refers the mound nature.

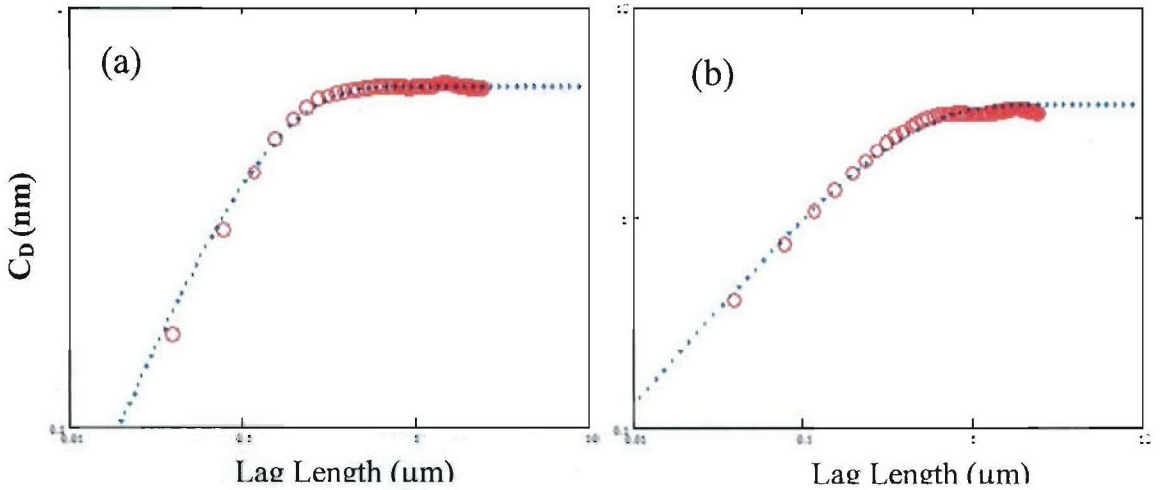

Figure 5.40. Height-difference correlation functions of the AFM data (circles) fitted to the phenomenological equation (dashed line) for a) CMP and b) IBAE processed GaSb surfaces.

amplitude implying an increased overall roughness compared to CMP surface. Next, the one dimensional isotropic power spectral density (1D-PSD) function was obtained for both CMP and IBAE surfaces and best-fitted for ***k***-correlation model for fractals, by adjusting the fractal roughness component (*Hp*), and cross-over point (*Bp*). The power-law slope for this function was also approximated. *Hp* and *Bp* values for the CMP processed surface were 0.90 and 685 nm, respectively while the Br-IBAE processed surface yielded 0.90 and 1350 nm, respectively.

As seen from Fig. 5.41, the one-dimensional power spectral density curves look bit similar with different roll off points. Also the power law slope of –4 was observed for the CMP and –3 for the Br-IBAE surfaces, visualized by the dotted lines in the plot, indicting that the surfaces showed random fractal behavior over four orders of magnitude. The cross sectional plots of the z height variations were also generated using the code and crosschecked with the original AFM image line scan for the consistency.

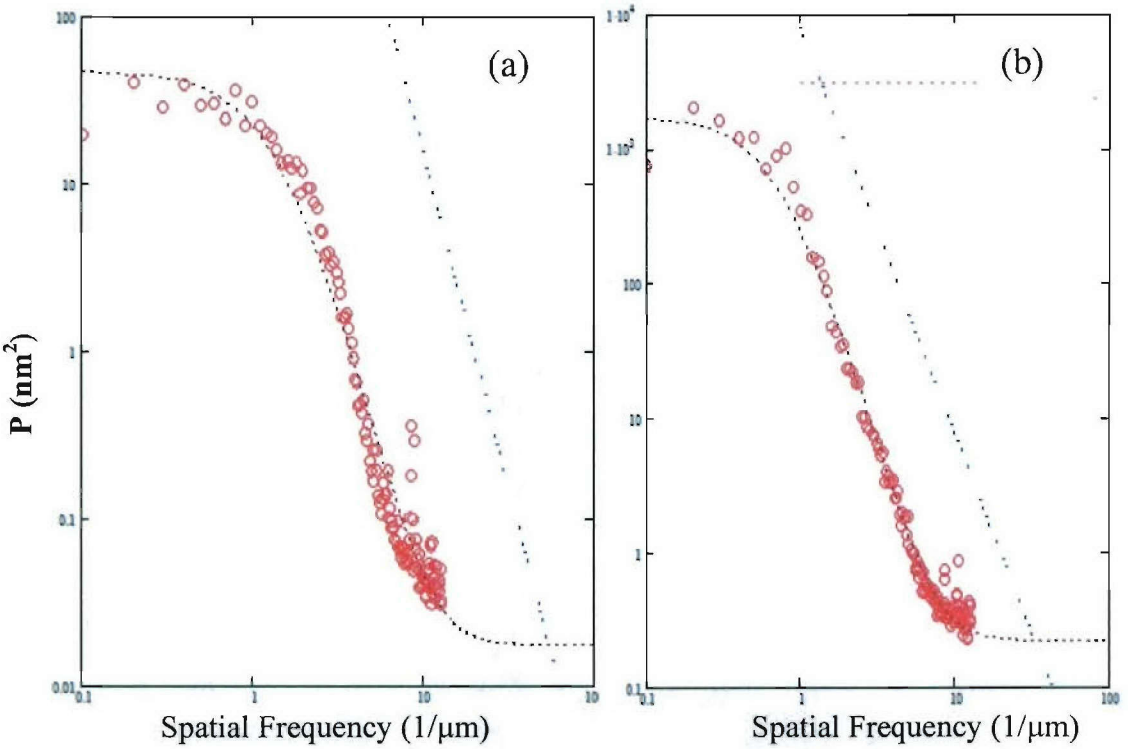

Figure 5.41. The one dimensional PSD distribution of the AFM data (circles) and its fit to the k-correlation model (dashed lines) for a) CMP and b) IBAE processed GaSb surface. Note that the straight dotted line is to indicate the power law slope.

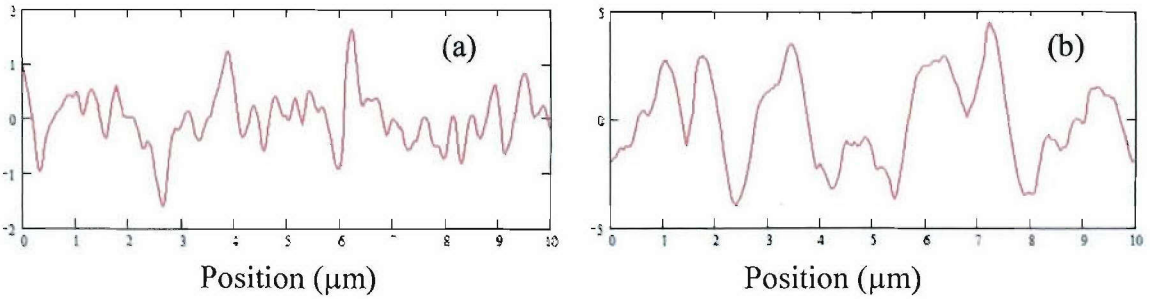

Figure 5.42 Height cross sections of a) CMP and b) IBAE processed GaSb surfaces using the statistical code.

The composite results of the statistical analysis, and its comparison to fractal surfaces for both CMP and Br-IBAE surfaces are provided in Table 5.8. The error in measurements for the Hurst parameter is ±0.1 while the error in the correlation lengths is ~10% or 2nm whichever is smaller. The measurement of the Hurst parameter indicated that CMP and IBAE surfaces were less fractal, i.e. less sharp and jagged, as shown in the height cross-sections in Fig. 5.42.

Table 5.8. Statistical analysis results of CMP and IBAE processed GaSb surfaces

	Auto-correlation		Height-correlation		*k*-correlation		
	H_a	ζ_a *(nm)*	H_d	ζ_d *(nm)*	H_p	B_p *(nm)*	*Slope*
CMP	0.90	175	1.0	117	0.90	900	-4
IBAE	1.00	340	0.95	325	0.90	1350	-3

The CMP finished episurfaces exhibited unevenly spaced steps and terraces with abrupt edges, while the Br-IBAE episurfaces showed the formation of concentric pyramid-like structures, with sharp points at their apexes that were randomly distributed. Autocorrelation data for these images showed Hurst exponent value of 0.945 for the CMP episurfaces and 0.9 for the BR-IBAE episurfaces with correlation lengths on the order of 900 nm for both CMP overgrown and IBAE overgrown surfaces. Higher magnification AFM images of the same surfaces, 1x1 μm^2 scan sizes, are shown in Fig. 5.43, where it can be seen that the CMP episurface exhibits meandering steps and terraces while the Br-

IBAE exhibits a high density of small, sharp protrusions on pyramid-like formations with smooth terrace step formation.

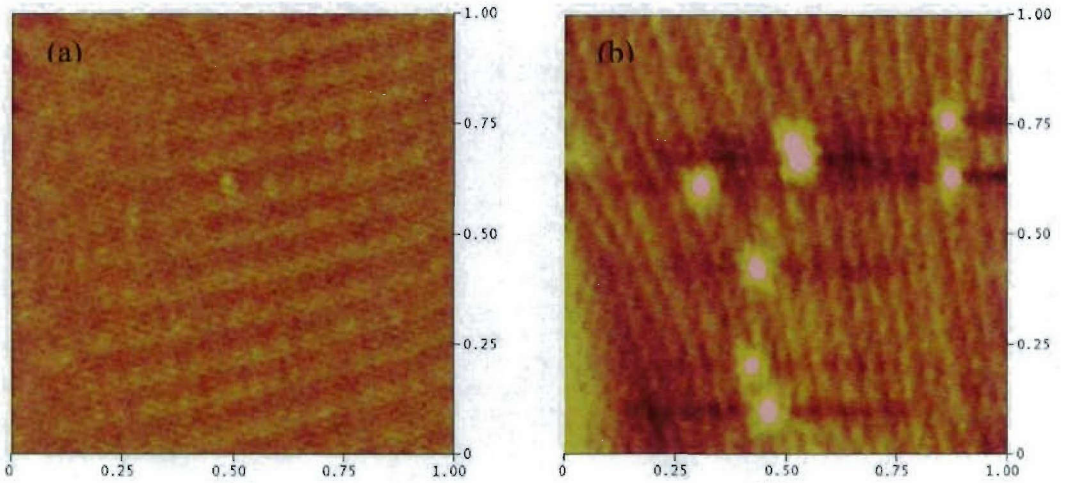

Figure 5.43. 1x1 μm^2 AFM images of overgrown surface of a) CMP and b) IBAE processed GaSb wafers.

When fitted with the first order Bessel function (continuous blue line) the autocorrolation function of CMP episurfaces, Fig. 5.44 a), showed weak oscillations corresponding to the weak step-terrace formations that were formed perpendicular to the y-axis, as shown in Fig. 5.43 (a), while the Br-IBAE episurfaces showed the presence of step and terraces with the presence of sharp protrusions. Autocorrelation data for the 1x1 μm^2 image, shown in Fig. 5.44, yielded a Hurst exponent value of 0.7 for both the CMP and Br-IBAE episurfaces. These images very clearly show the distinctive mound topographies processed. Further analysis on the same surfaces showed the correlation for both CMP and Br-IBAE episurfaces quickly decline at relatively short lag lengths and is nearly uncorrelated beyond ~100 nm. Additionally, the weak correlation peak observed for the Br-IBAE episurfaces at a lag length of ~350 nm is due to the average or isotropic spacing between the sharp point-like protrusions

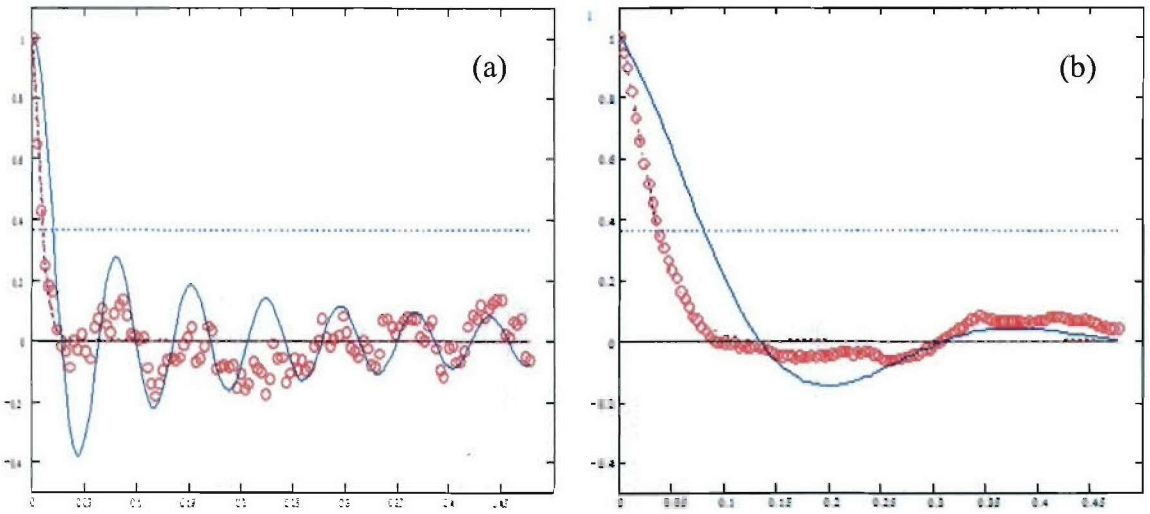

Figure 5.44. Auto correlation functions of the AFM data (circles) fitted to the phenomenological equation (solid line) for epitaxial layers grown on a) CMP and b) IBAE processed GaSb surfaces using 1 x 1 μm^2 size features.

5.4.6 Br-IBAE Polish Summary

Although producing initially rougher surfaces with a thin oxide and Br surface layer, Br-IBAE etched wafers were easy to overgrow with MBE. The MBE process was able to smooth out the initial rough surface and the substrate/epi interfaces showed no defects in most cases and few defects in cases where thermal desorpiton of the oxide was not complete. The technique is well suited for forming patterned substrates for overgrowth and may have advantages as a clean up etch right before ohmic contact metallization. The major problem with the technique is that no commercial systems are available and wafer scaling of the current system for full wafer production is problematic. Under the Center's Galaxy Phase II which is currently active, a Br-IBAE approach using a divergent Kkaufman ion gun will be implemented in order to process 3 inch GaSb wafers.

5.4.7 Br-IBAE References

5.16. Shivashankar R.Vangala, "Development of Epi-ready Bromine ion-Beam-Assisted etched GaSb Substrates for GaSb molecdular Beam Epitaxy," UMass Lowell Department of Physics, M. S. Thesis (W. Goodhue, Advisor) 2005.

5.17 D.I. Lubyshev, M. Micovic, W.Z. Cai, and D.L. Miller, "Molar fraction and substrate orientation effects on carbon doping in InGaAs grown by solid source molecular beam epitaxy using carbon tertrabromide, " Journal of Appl. Phys. 84(8), 1998.

5.5 Inductively Coupled Plasma Etching of GaSb Surfaces

A small effort was undertaken to determine if an inductively coupled plasma (ICP) process could be used as a final GaSb polish. A diagram of a typical system is shown in Fig. 5.45. In this type of system the gas is ionized by creating a plasma away from the sample and then streaming the radicals formed in the plasma to the sample surface through bias voltage conditions. The idea is to keep the hot plasma away from the sample and etch down stream.

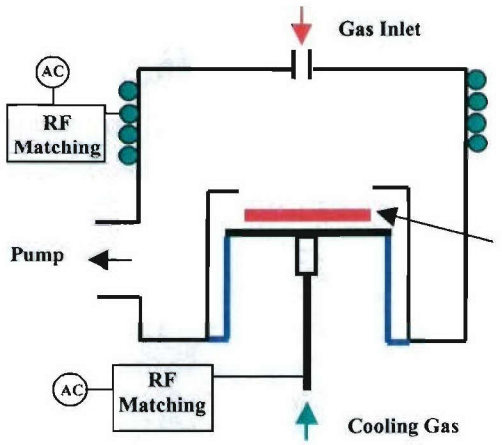

Figure 5.45. Schematic diagram of a typical ICP system.

The problem with these types of systems is that the parameter space is very large. Each gas or mixture of gasses has parameters which need to be optimized for the particular sample being etched and there are many gasses and gas combination that may prove successful. In this work, a proprietary $Cl_2/SiCl_4$ process was used that etched GaSb substrates at a rate of 0.39 micrometers per minute while producing a mirror smooth surface by eye. The exciting aspect of these system is that they can accommodate 6 inch and larger wafers.

Figure 5.46 shows AFM images from the two ICP runs we attempted while Table 5.9 is a compilation of the statistics from the images. As one sees in the images and statistics there appears to be debris on the surface of the wafers left from the process and the statistics indicate a fairly rough surface. Figure 5.47 shows typical AFM images of the surface of one of the epilayers grown over one of the ICP surfaces. Note that the left image shows uniform step behavior in spite of the rough starting surface. The lower magnification image shows that the debris left in the ICP process has left defects on the episurface. The statistics for the episurfaces of Fig. 5.47 are shown in Table 5.10.

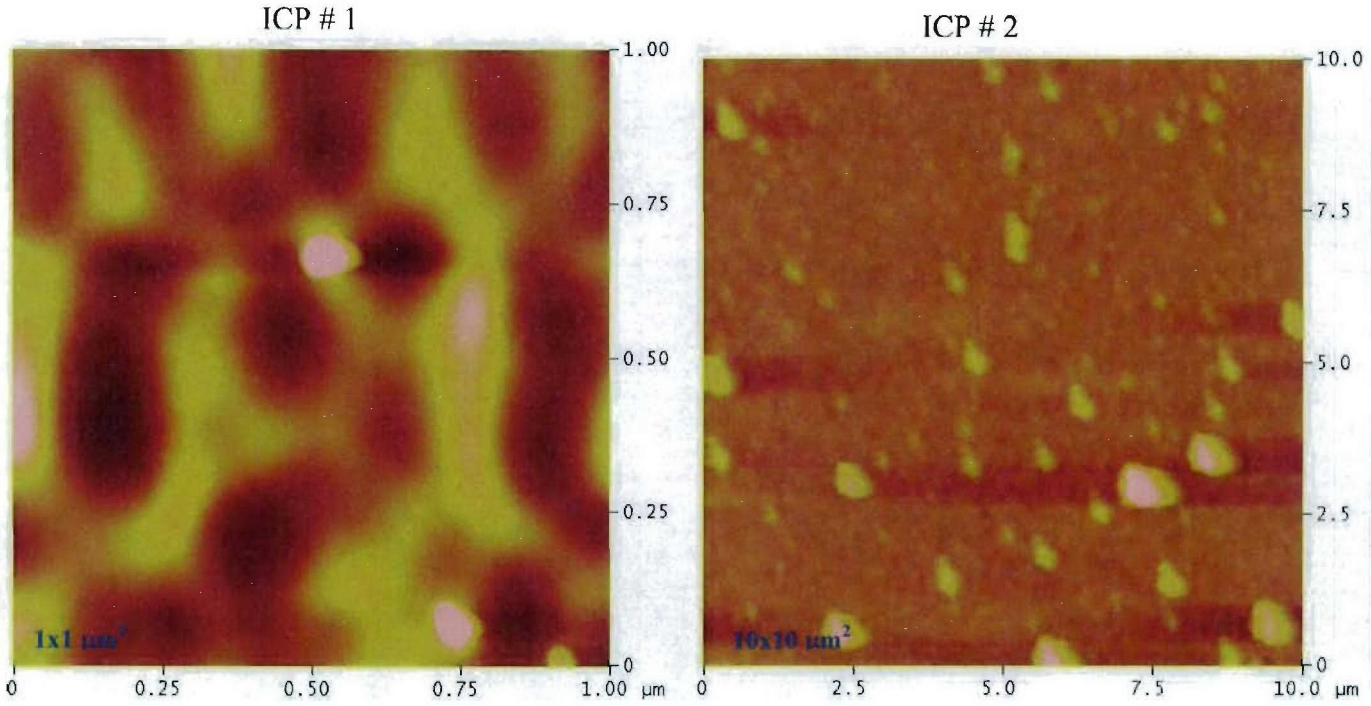

Figure 5.46. AFM images taken from the ICP processed surfaces of two GaSb wafers, ICP #1 and ICP #2.

Process #		RMS (nm)	Ra (nm)	Z-range (nm)
ICP # 1	**1x1 μm²**	4.31	3.35	34.46
	10x10 μm²	17.05	8.92	269.80
ICP # 2	**1x1 μm²**	4.07	3.08	62.94
	10x10 μm²	26.92	13.48	367.62

Table 5.9. Statistics taken from the AFM images of the surfaces of ICP #1 and ICP #2 processed wafers.

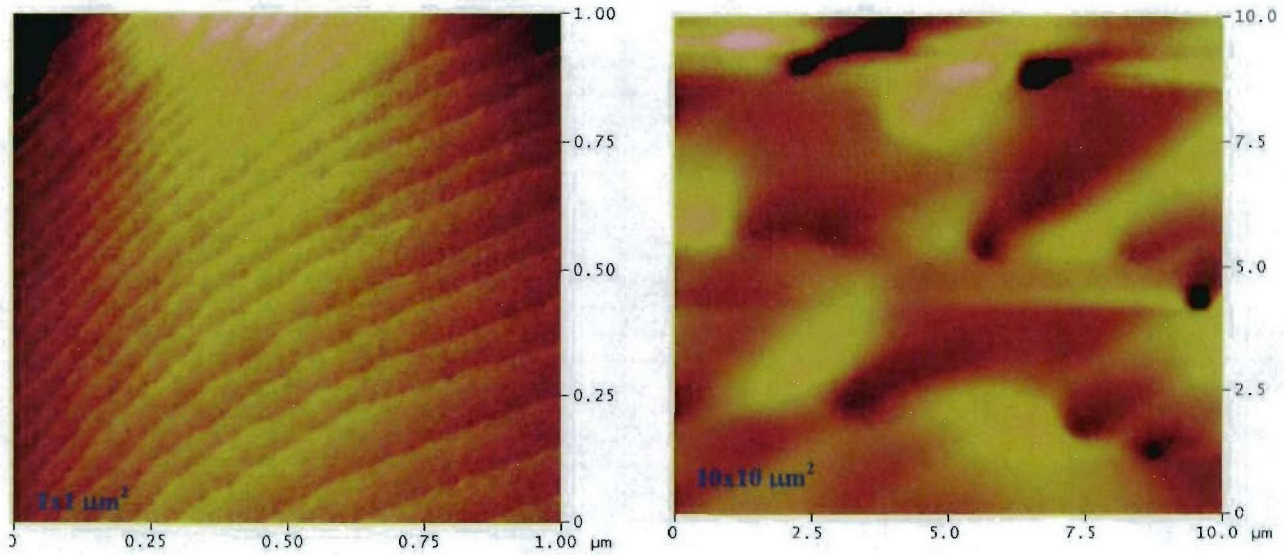

(a) (b)

Figure 5.47. AFM images of the episurface of MBE run 04-118, ICP #2.

MBE-04-118	RMS (nm)	Ra (nm)	Z-range (nm)
1x1 μm^2	0.36	0.27	2.99
10x10 μm^2	1.12	0.89	7.28

Table 5.10. AFM statistics for the images shown in Fig. 5.47.

Since full 2 inch GaSb wafers were etched, pieces were used to grow a GaSb homoepitaxial layer (40-118) and two quantum well structures (04-119 and 04-2=120). The photoluminescence spectra from these samples is shown in Fig. 5.48. As one sees in the figure, the spectra from the two quantum well samples is fairly strong.

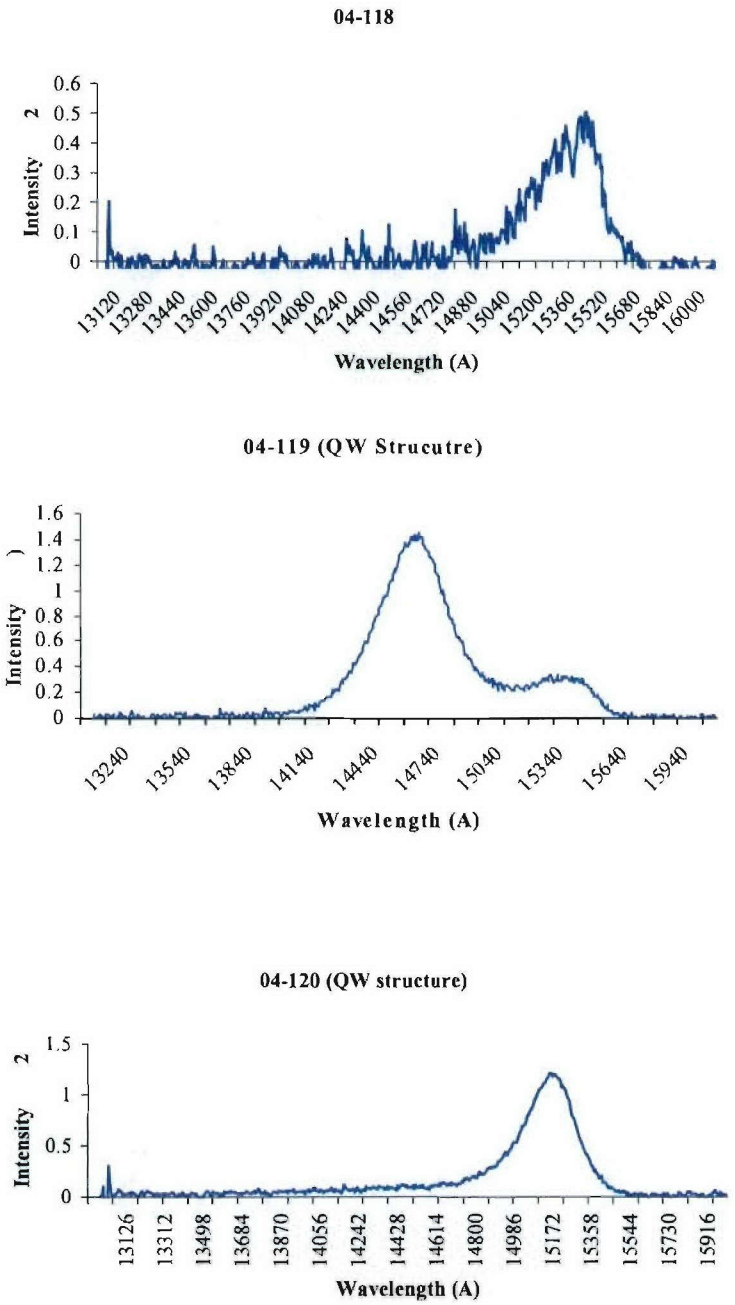

Figure 5.48. Photoluminescence spectra from a GaSb homoepitaxila layer (04-118) and spectra from two quantum well layers (04-119 and 04-120).

From this effort, one sees that the ICP process seems promising as a final polish although new recipes and procedures will need to be devised in order to get rid of the

debris problem. It is interesting to note that as in the BR-IBAE process, the initially rougher substrates can be planarized during the MBE growth process (compare Table 5.9 to that of 5.10) to produce material with good quantum well photoluminescence. Unfortunately the group does not have access to an ICP in house necessitating the termination of the ICP effort.

5.6 Dry Final Polish Summary

All three of the final dry etch polish techniques, GCIB, Br-IBAE and ICP, produced final surfaces that were successfully over grown with MBE. For the purpose of wafer preparation GCIB is currently the most effective since 1) an engineered oxide can be deposited on the surface while removing only 10's of nanometers or actual material, 2) the oxide/substrate interface can be made very planar, 3) with an appropriate recipe, the epi/substrate interface can be made nearly to fully defect free, and 4) the scaling for runs of commercial wafers is already at hand. The technique is expected to be adjustable in order to polish antimonide alloys through recipe manipulation.

The Br-IBAE is currently very useful for patterning GaSb substrates and epitaxial layers for overgrowth and regrowth. This feature can be used to fabricate new types of buried structure devices. The technique is also applicable to general anitmonide all device fabrication. There is currently no system scaled up to the point where three and four inch wafers can be Br-IBAE etched. Our Galaxy Phase II SBIR effort continues to explore this issue.

Since IPC uses chemistries similar to IBAE all that was said about IBAE can be included here. The debris problem found in this work needs to be traced down before the system is useful for wafer polishing. If a solution can be found, the ICP may indeed be a viable polish tool. The ICP instruments are again already scaled to the point where either single large wafers or groups of smaller wafers can be processed in single runs. This technique is also expected to be adjustable in order to polish antimonide alloys through recipe manipulation.

The techniques developed here are also very applicable to ohmic contact formation. They can be used as a surface preparation step just prior to metals deposition. The group suspects that by manipulating the oxide before metals deposition allows one to manipulate both the resistance and depth of the contact.

6. Terahertz Technologies Effort

6.1 Overview

Over the past several years our group has been developing photon-mediated quantum-cascade THz lasers based on the AlGaAs materials system [6.1-6.6]. These devices use a three level scheme employing modules of coupled quantum wells where electrons are injected from the lower level, level 1), of the previous module into the upper level, level 3) of the adjacent module. THz radiation is emitted from the level 3) to level 2) transition and level 2) is rapidly depopulated by interface phonons. In earlier work the engineered interface phonons were observed using far-infrared Fourier transform spectroscopy [2], non-coherent emission was demonstrated in two samples using the step-scan Fourier transform spectroscopy technique [6.2,6.4] and a dual frequency mode of emission was designed and observed in one of the structures [6.4]. The authors strongly believe that interface phonon depopulation, which moves level 3) to level 1) transitions out of the phonon bands is the most efficient way to design THz lasers, and believe the current exciting devices being demonstrated in Europe and the U.S. [6.7,6.8] can be significantly improved with the incorporation of interface phonon relaxation.

As part of the DARPA/AFOSR ABCS effort the Photonics Center and the Submillimeter-wave Technology Laboratory of the University of Massachusetts Lowell in conjunction with Quantum Semiconductor Algorithms, Inc. (our group) was given a small amount of funds to conduct an approximately 9 month study to develop an understanding of some of the critical issues involving the development of terahertz phonon-meadiated quantum cascade AlGaAs lasers. Since two graduate students, Jin Li and Beihong Zhu, decided to make portions of this work their Ph. D. theses, the work continues beyond this program. During the effort multi-band multi-parameter computer codes were developed to optimize the laser structure at user selected wavelengths; a phonon model was developed to predict interface, well and barrier phonons; a frequency selective surface structure was applied to a high-index low-loss semiconductor to demonstrate that facet reflectivity can be made up to 95% reflecting; a state-of-the-art Veeco Gen II MBE system was installed in the Photonics Center; and simple photonic crystal terahertz waveguide structures were designed to transform the highly divergent terahertz semiconductor waveguide laser output beam into a more user-friendly directed beam with minimal loss.

The results of the work are as follows:

1) Two new THz QCL laser designs were developed using the models developed here.
2) Wax-jet prototype THz photonic crystals were demonstrated as slot filters.
3) Prototype GaAs THz photonic crystal waveguides were fabricated.
4) Epitaxial Structures were grown using the new designs both at WPAFB and UMass Lowell (using the Photonic Center's New Gen II MBE System). Fabrication issues were also examined in this portion of the work.

5) A simple experiment was performed to demonstrate the usefulness of developing a terahertz imaging system for homeland security.

These results are described in more detail in the subsections below.

6.2. QCL Device Modeling

Professor Ram-Mohan of Quantum Semiconductor Algorithms, Inc., has been providing theoretical support by developing the group's modeling capability. At the present time, the theory aspects of the design of the quantum cascade structure are well understood in general. In this effort he has focused on the development of modeling software and on developing theoretical methods to make the software efficient.

The modeling codes are being developed in a Finite Element framework for maximum flexibility, for ease of use and for accounting for the physical issues such as building in the proper boundary conditions and requiring Schroedinger Poisson selfconsistency in the band bending in the presence of charge redistributions in the multi-layered heterostructure. The finite element method may be thought of as the discretization of the action integral followed by the principle of least action, a principle that is central to all of physics. In this sense, the method provides a direct connection between the theory and the programming implementation for simulations.

Given layer thickness for each layer in a multi-layered heterostructure, we solve the Schrödinger equation for energy levels and wavefunctions. This work has been done in fair generality so that any number of layers can be included. The effect of external bias on the energy levels and the wavefunctions has been modeled so far.

The finite element calculations of the Schroedinger and the Poisson equations, in an iterative manner, are done using sparse matrix methods developed by Ram-Mohan. The sparse matrix package used by us has been in development since 1997 and is now giving us the ability to perform such calculations with the tightest memory requirements and with high speed.

6.2.1 Outcomes To-Date

1. The finite element programming now allows us to obtain wavefunctions and energy levels in the quantum cascade structure under bias and with doping.
2. We now have a reliable method for the calculation of the total rate for electron-electron (*ee*) scattering. This requires the evaluation of a seven-dimensional integral to account for the "dephasing" of the electrons in various energy levels. The method uses Gauss-Legendre quadrature in its innermost integrals followed by a Monte-Carlo approach to the outer 5 integrals. This has speeded up the evaluation of the integrals for a final total rate for *ee*-scattering. Despite this, the calculation takes several hours on a fast PC. We are now ensuring ANSI-compatibility of the codes in order that they could be run on mainframe computers.

3. The modeling of electron-phonon interaction, for confined phonon and interface phonons, has been set up and we are in the process of integrating these calculations with the Schroedinger-Poisson solver. (Independently, Ram-Mohan has performed a comprehensive survey of the theory and experimental status of our understanding of LO-phonons in ternary compound semiconductors. At issue is the nature of the modes in mixed crystals and obtaining a general approach to the modeling of these lattice excitations and their interactions with electrons. The review article is under preparation.)
4. The numerical modeling is focusing on the calculation of the gain in the quantum cascade structure and the solution of the rate equations. This is work still continuing.
5. Given a target wavelength in the region of 60-200 microns, the question to address is, "What is the optimal QCL structure that would show enhanced emission/lasing at that desired wavelength?" This requires optimization of the QCL structure for layer thicknesses and for gain. Ram-Mohan has initiated an effort in this direction. We already have insights into the layer ordering and the basic structure of each period. A fuller development of the codes with a "wrapper program" around the physical modeling for the optimization of the input parameters is desirable.

The above considerations make the modeling problem challenging and we are steadily progressing towards the goal of being able to design structures for any wavelength in the region of 60-200 microns. These codes will be made compatible with the parallel effort in the design of the laser cavity and the photonic aspects of the laser design.

6.2.2 New QCL Designs

Graduate student Beihong Zhu has developed two new four well cascade structures, A (Fig.6.1 a) BH401/G2959) and B (Fig.6.1 b) BH402). For A, emission is expected at 122.8 micrometers (10.1 meV) from E_5 to E_4 at a bias of 0.065 V per module. For B, emission is expected at 75.2 micrometers (16.5 meV) from E_5 to E_4 at a bias of 0.069 V per module. Details of the phonons, photon modes, wavefunctions, and energy levels are given below.

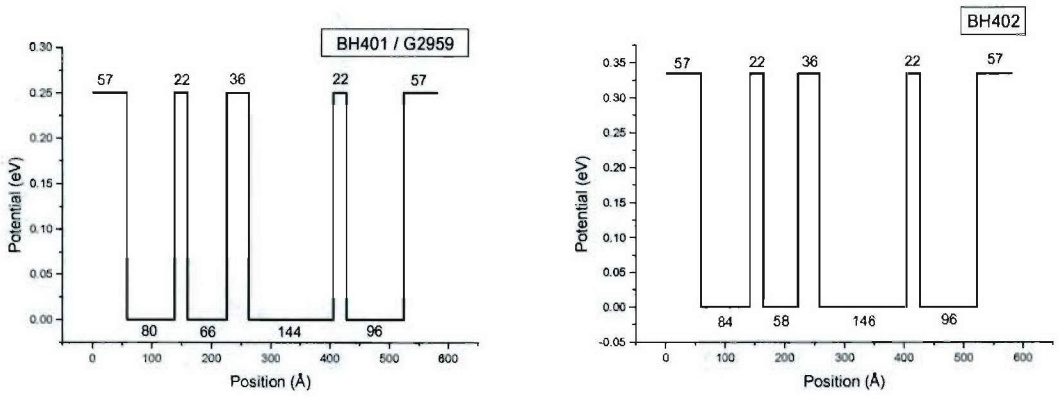

(a) (b)

Figure 6.1. Conduction-band diagrams of the two new four-well designs. The design in a) is expected to emit at 122.8 micrometers while that of b) is expected to emit at 75.2 micrometers.

As shown in Fig. 6.2, BH401/G2959 structure is grown in GaAs/$Al_{0.3}Ga_{0.7}As$, and the radiative transition is vertical, mainly located in the previous two wells, while the depopulation is highly selective, as fast electron-phonon scattering takes place in the next adjacent well. At design bias (65 mV/module), vertical radiative transition between levels 5 and 4 levels (E_{54} = 10.1 meV) gives the lasing emission at 2.45 THz, level 4 and 3 are brought into resonance with an anticrossing gap of 3.1 meV, enabling fast depopulation via all phonon modes (confined and interface-phonon modes) scattering into the levels 2 and 1 (E_{32} = 47 meV). The center barrier is relatively thick (36 Å), limiting parasitic scattering out of the upper state 5. Besides assuming a fully coherent tunneling process between levels 4 and 3, additional depopulation of level 4 can take place via electron–electron scattering into level 3, which also has a short lifetime of ps. Electrons collect in the anticrossed 2-1 doublet (E_{21} = 4.7 meV), where they are injected into the level 5 state in the next module.

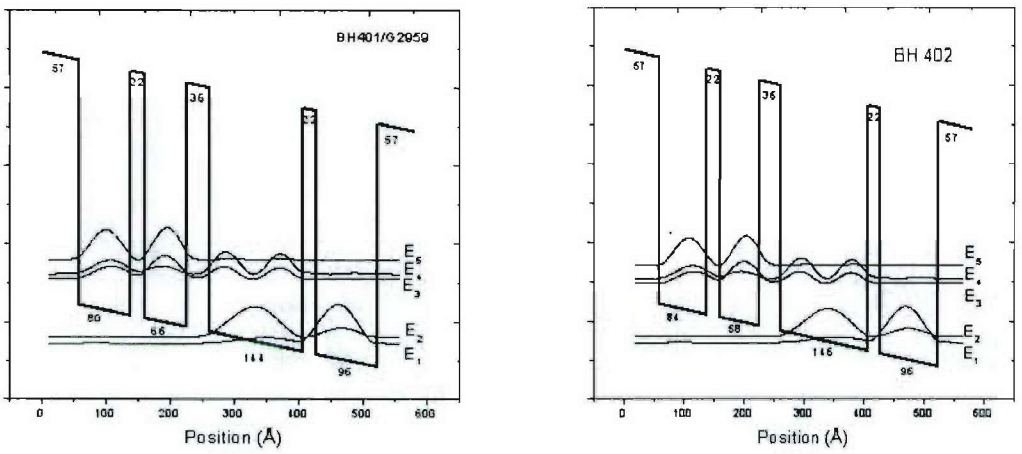

Figure 6.2. Wavefunctions of the first 5 energy levels generated in the four well structures A (plot a) and B (plot b) being explored as the modules for terahertz quantum cascade lasers.

The first two confined well modes for A (BH401) are shown in Fig. 6.3. All of the confined well modes have energies of about 36 meV. The first few GaAs-like interface modes are shown in Fig. 6.4 and the last few AlAs-like modes are shown in Fig. 6.5. Note that the highest modes have energy levels of approximately 47 meV.

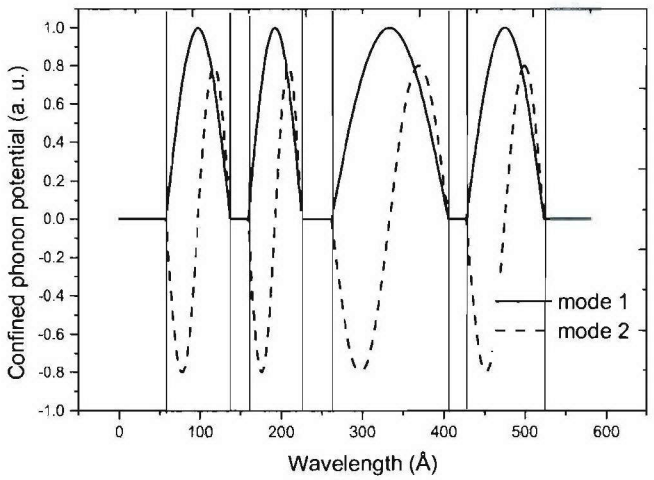

Figure 6.3. The first two confined -well phonon modes of the four-well module A (BH401) are shown in the plot. All of the confined-well modes have energies of about 36.25 meV.

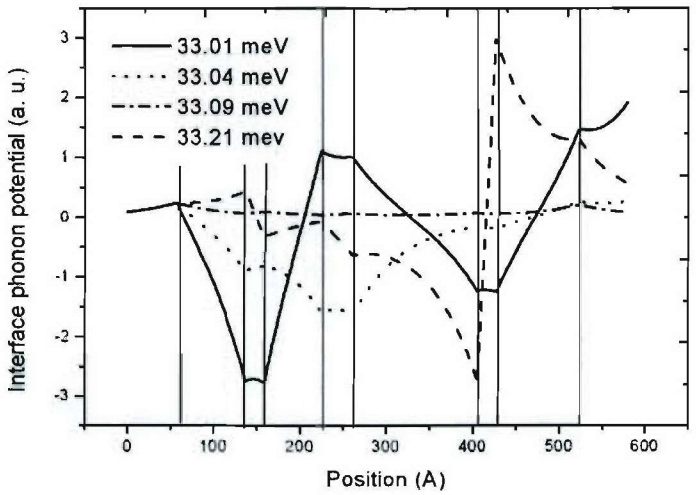

Figure 6.4. Low-energy (GaAs-like) interface modes of the four-well module A (BH401) are shown in the plot. These modes have energies around 33 meV as shown in the key.

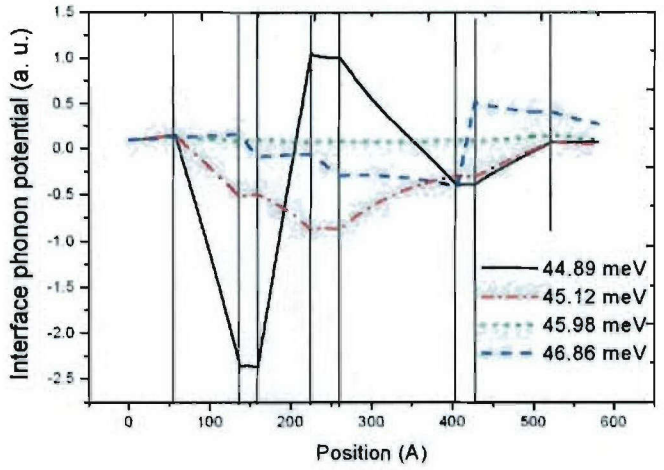

Figure 6.5. High energy (AlAs-like) interface modes of the four-well module A (BH401). 24 phonon modes are available in this structure. Note that these modes have energies as high as 46.8 meV.

In these four-well designs as in previous two and three-well designs we have attempted to use the higher energy modes of the structure as the mechanism to sweep the electrons out of the lower laser level quickly and maintain inversion while suppressing phonon assisted non-radiative recombination between the upper lasing level and the ground states. We find the process appealing and compatible with designing the structure to also minimize electron-electron scattering problems and to maximizing gain.

6.3 Phonon-Mediated QCL Materials and Fabrication Effort

6.3.1. Facet Reflectivity Control

The long-wavelength QC devices ($\lambda > 20$ microns) recently reported by the Bell Labs group [6.9, 6.10] operated above threshold with cleaved end facets only, implying a cavity reflectivity of roughly 30%. Output power of these devices could be substantially improved if end facet reflectivity could be increased. We propose to enhance the reflectivity of the bar ends by depositing a high-reflectivity frequency-selective-surface (FSS) consisting of vertical metallic strips deposited directly on the facet ends. UML researchers have designed, fabricated, and implemented "strip-type" high-reflectivity, low-absorption FSS laser output couplers for use in their THz molecular gas lasers (Fig. 6.6). The couplers have clearly shown to improve both their output power and spatial mode characteristics. These couplers consist of metallic strips of a specific width and periodicity deposited onto low-loss substrates and are designed to have reflectivities in the 90%-97% range as well as having low overall absorption (<1%). Shown below are several reflectance spectra of output couplers (strip width 13.5 microns, periodicity 20 microns) designed for a THz laser operating near 205 microns.

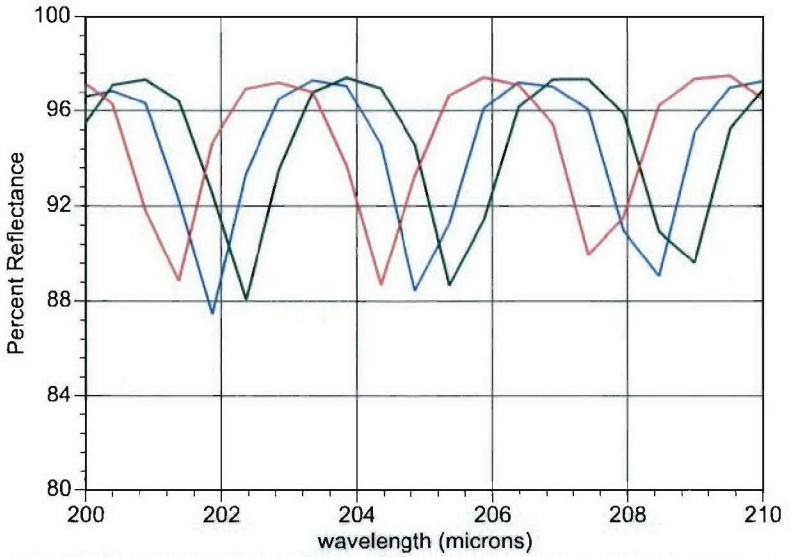

Figure 6.6. FTIR reflectance spectra of three THz laser output couplers. The percent reflectance was found by subtracting the measured transmittance from unity.

For vertically polarized intersubband emission wavelengths near 80 microns, our theoretical calculations indicate that 4-micron-wide metal strips with 11 micron spacing will provide >95% facet reflectivity. Use of metallic strips is a relatively straightforward task compared to the challenge of growing high-reflectivity dielectric stacks at these long wavelengths.

6.3.2 Epitaxial Growth of THz QCL Structures

The group is very fortunate to be working with Drs.Thomas Nelson and James Ehret of Wright-Patterson Air Force Base who supplied us with a number of epistructures for the work. Ten device wafers were grown for the effort at WPAFB. All of the WPAFB material show excellent photoluminescence characteristics. The material was used to both develop fabrication techniques as well as to fabricate THz laser structures. While working with the WPAFB material the Photonics Center installed (with partial funding from this effort) a GEN II MBE machine recently donated to the Center by Corning, Fig. 6.7. This state-of-the-art-system has unique in situ ellipsometry capabilities that will be of significant help in growing these complex devices. Both WPAFB and the Photonics Center grew wafers that incorporated the new phonon mediated THz QCL designs developed in this work

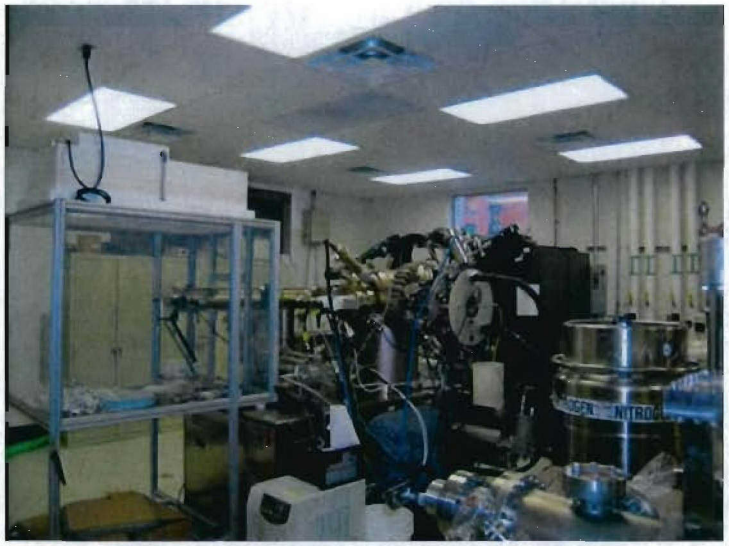

Figure 6.7. Photograph of the Photonic Center's recently acquired Veeco Gen-II MBE system. The system in on–line in a newly constructed laboratory in the UMass Lowell Photonics Center.

Here the focus will be on discussing wafers grown using the new designs A and B. Sample A, (BH401 was grown at both WPAFB and the Photonic Center using the Center's Gen II. The Photoluminescence for each sample is shown in Fig. 6.8. As one sees from the figure, both samples were high quality. Table 6.1 shows how the peaks matched up to the theory. From the table one sees that the agreement was excellent. Although the ABCS project is now over Beihong will attempt to fabricate lasers out of these materials and then test the devices to see if they lase.

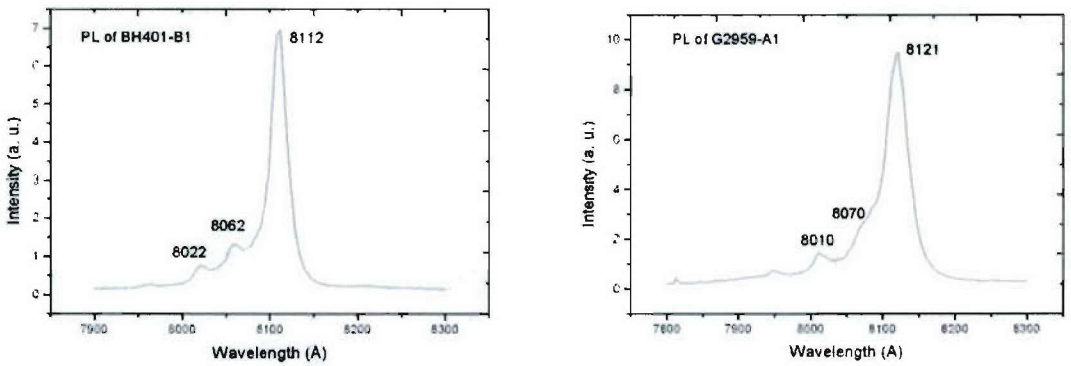

(a) (b)

Figure 6.8. Photoluminescence spectra from (a) sample A (BH401) grown at the photonic center and (b) sample A (G2959) grown at Wright-Pat.

Opt. transitions	$E_{e1\text{-}hh1}$ (eV / Å)	$E_{e1\text{-}lh1}$ (eV / Å)	$E_{e2\text{-}hh1}$ (eV / Å)
Theory	1.528 / 8116	1.537 / 8068	1.547 / 8016
Exp. of BH401-A1	1.529 / 8110	1.539 / 8060	1.549 / 8006
Exp. of BH401-B1	1.529 / 8112	1.539 / 8060	1.546 / 8022
Exp. of BH401-B2	1.529 / 8112	1.538 / 8064	1.545 / 8024
Exp. of G2959-A1	1.527 / 8121	1.537 / 8070	1.548 / 8010
Exp. of G2959-A2	1.527 / 8120	1.539 / 8070	1.547 / 8014
Exp. of G2959-B1	1.528 / 8114	1.537 / 8166	1.548 / 8012

Table 6.1 Comparisons of the theory to the photoluminescence peaks obtained from sample (A) (BH401) grown at the Photonic Center to those of (A) (G2959) grown at Wright-Pat.

6.3.3 Terahertz Quantum Cascade Laser Fabrication

6.3.3.1 Mask design

Our laser chip design has borrowed the idea from Ref [6.11]. The schematic diagram of the structure is shown in Fig. 6.9. To fabricate the laser chip, a set of photomasks were designed and fabricated.. The set includes three photomasks. The first mask is used for the laser ridge formation. Five different ridge widths ranging from 60 μm to 140 μm were designed for the evaluation of the impact of the ridge width on the laser performance. The second mask defines the ridge and bottom contacts. Two bottom contacts were at 60 μm and 180 μm away from the ridge, respectively. Two contacts are expected to reduce the series resistance of the laser. On the other hand, two separate bottom contacts can be used to study the effect of the series resistance. The third mask is for the top bonding pad, with which wire bond for the laser ridge can be done away from the ridge, protecting the laser active region from the potential damage by the wire bonding process.

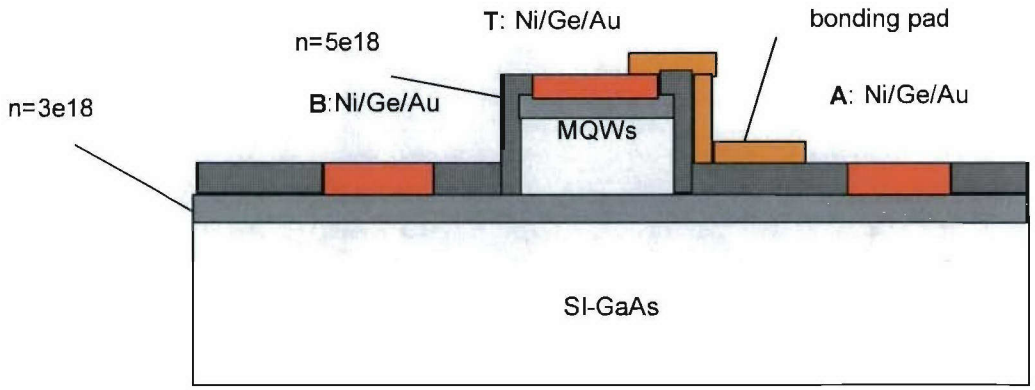

Figure 6.9. Schematic diagram of the laser

6.3.3.2 Ohmic Contacts and Device Resistance

Zhu has optimized two of recipes for the formation of ohmic contacts on the laser chips. One recipe uses the metal contact layers of Ni/Ge/Au. By using transmission line method (TLM), his experiments show that annealing the contact at a temperature of 495 °C yields the lowest contact resistance. The other recipe is based on layers of Ni/Ge/Au/Ni/Au. This recipe gives low contact resistance at an annealing temperature 520-580 °C depending on the individual thickness of the metals.

The laser chips fabricated using the photomasks described above and optimized ohmic contact recipes produces total resistances (including the ohmic and series resistance) in the range of 2 to 4 ohms. For the ridge formation, dry etching (Bromine ion beam assisted etching) and wet etching (the etchants based on $H_2SO_4/H_2O_2/H_2O$, and $NH_4OH/H_2O_2/H_2O$) are used. These etches are used to obtain

smooth ridge formation and optimized pre-ohmic surface quality. The later is crucial for the formation of high quality ohmic contacts that ball bond well.

Device resistance is an important parameter in these 50 to 150 period structures. This is especially true since one needs to dope the wells very lightly in order to reduce electron – electron scattering while maintaining a low resistance to allow reasonable drive voltages. The problem is compounded by the fact that to keep the quantum wells robust the AlGaAs should be grown at lower temperatures to avoid GaAs/AlGaAs mixing while growing lower temperature AlGaAs can lead to electron traps in the AlGaAs layers. The use of ultra high purity materials and proper MBE machine growth preparation are critical elements for obtaining layer structures with a chance of working as lasers.

6.4 Thermo-Wax-Jet Rapid Prototype Photonic Crystals

6.4.1 Thermojet® Rapid Prototyping Overview

Thermojet® solid object printer is a solid freeforming method. It is an inexpensive way to build complex two-dimensional (2-D) or three-dimensional (3-D) models quickly. The prototypes built can also be used for investment casting and molding. First, a 3-D Computer-Aided Design (CAD) file of the structure design is generated with a software package such as SolidWorks and then imported to the ThermoJet® solid object printer. The printer "prints" physical models from the CAD data files by spraying layers of tiny droplets of wax onto a platform surface and the structure is built up layer by layer until it is complete. The specified resolution of our ThermoJet® printer is 300 x 400 x 600 dpi (XYZ) with the layer thickness of 0.042 mm. It took less than one hour to fabricate a 3-D structure with the dimension of 24 cm × 24 cm × 5 cm, compared to weeks to fabricate the 3-D structures using micro-machining or semiconductor processing. The build material, called Thermo Jet 88 wax, is a solid thermopolymer material, which contains hydrocarbons, amides and esters. It melts around 80 – 90°C. The supporting wax maybe used during the "printing" process to support the suspended structure, which can be broken out from the support after being kept in refrigerator for around half hour. This work and write up along with that of the waveguide section has been taken from graduate student Jin Li's thesis.

6.4.2 Optical Properties of the Thermojet Wax

The optical properties of the build wax and the photonic crystals were characterized using a Bruker IFS 66v Fourier Transform Infrared Spectrometer (FTIR). It is equipped with a mercury arc-lamp as the radiation sources, mylar beamsplitters and a liquid helium-cooled Silicon bolometer to operate from 7500 cm^{-1} to 5 cm^{-1}. The maximum scanning resolution is 0.05 cm^{-1}. To avoid the impact from the water and CO_2 absorption in far infrared region, the sample and all optics are kept in the separate compartments which are pumped down to vacuum during the data collection. A wire grid polarizer can be placed between the far infrared source and the sample to measure the transmission spectra for either TE or TM polarizations.

The index of refraction and the extinction coefficient of the Thermo Jet 88 wax were determined from the transmission spectra of a plane-parallel, homogeneous, smooth sample of known thickness t, using the multiple-beam interference model [6.12]. The FTIR spectrum of a solid block of the wax was measured from 5 cm^{-1} (0.15 THz) to 50 cm^{-1} (1.5 THz) with a resolution of 0.05 cm^{-1}, shown as the pink curve in Figure 6.10. The transmission curve is modulated by a pattern of Fabry-Perot fringes due to the interference effect between the front and rear surfaces of the sample. The real part of the refractive index n can be determined from the locations in frequency of the transmission maxima (or minima). The extinction coefficient k of the material as the function of frequency can be derived by fitting the experimental data. The fitted transmission curve for the wax is shown in the black dotted line. The refractive index was determined to be 1.47 between 200GHz to 1.5THz, which corresponds to a dielectric constant (ε) of 2.16. The fitted extinction coefficient (k), illustrated as the thick black curve, shows that the

optical absorption of the wax increases with the frequency. At the frequency of 1.5 THz, the absorption coefficient is 9.12 cm^{-1} and less than 1% radiation will transmit through a 1 cm thick wax block. Therefore, the wax is more suitable to the application at lower frequency.

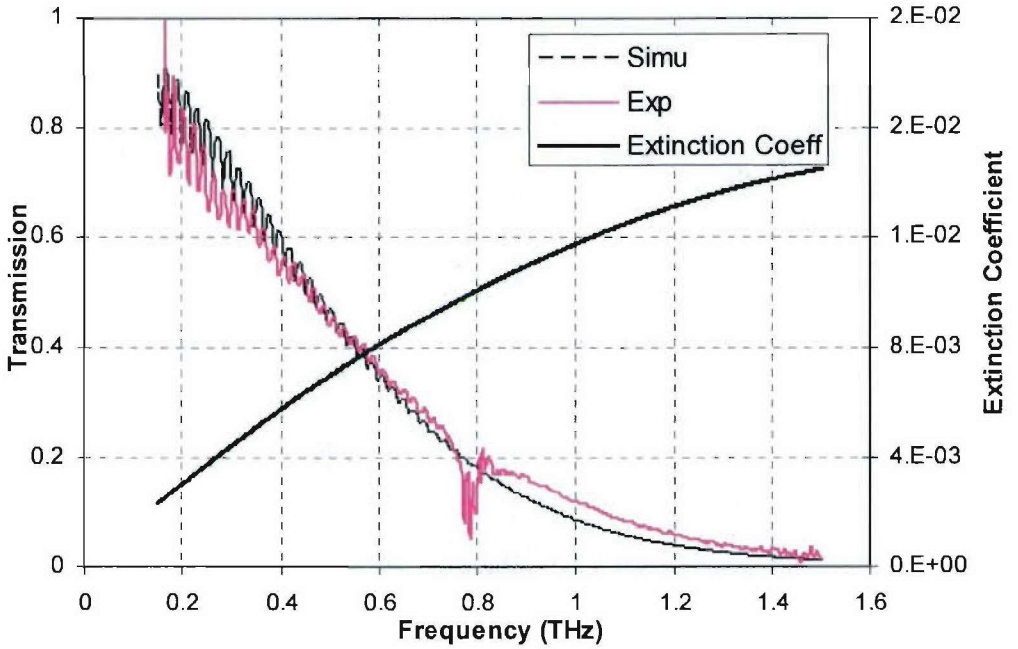

Figure 6.10 Transmission spectrum of the Thermo Jet 88 wax. The pink curve is the experimental result.

6.4.3 Two-dimensional Photonic Crystals based on Thermo Jet Wax

To print a 3-D structure with Thermojet® printer, the supporting wax is required. If the 3-D structure designed to have very small air spaces between layers which are filled with supporting wax during printing, it is usually very difficult to clear out these spaces. Therefore, 2-D structures are preferred since no supporting wax is required if the structure is printed along the air column. The contrast in the dielectric constant ε of Thermo Jet wax to air is low (2.16:1), resulting in smaller photonic bandgap compared to materials with higher n. Two-dimensional triangular lattice photonic crystals have shown wider photonic bandgap compared to other 2D photonic crystal structures and were selected as our 2-D structures. The dielectric constant was then used in the theoretical bandgap calculation by a block-iterative frequency-domain method for Maxwell's equations in a planewave basis [6.13]. For a 2-D photonic crystal with triangular lattice of air columns in wax, there is no full TM bandgap observed. The maximum TE bandgap was obtained when the ratio of air column radius (r) to the period (a) was optimized to around 0.37. The TE bandgap extends from 0.500 c/a to 0.514 c/a, where c is the speed of the light. The band diagram is shown in Figure 6.11 a). It also shows that there is a wider TE band gap from 0.438 c/a to 0.514 c/a as well as a TM band gap along Γ-M direction. The r/a was selected as 0.28 for the photonic crystal with a triangular lattice of wax rods. The TM bandgap from 0.506 c/a to 0.537 c/a and no complete TE bandgap

were observed in this case. Again, the TM bandgap is wider and the TE bandgap is open along Γ-M direction.

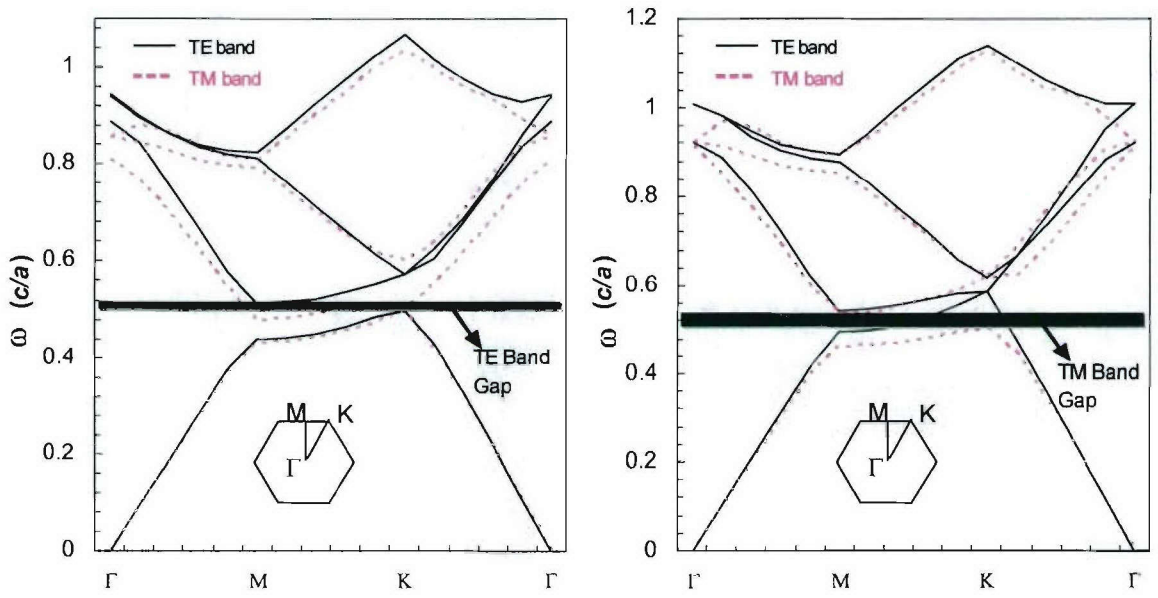

Figure 6.11. Band diagram of 2-D photonic crystals (a): triangular lattice of air columns in wax (b) triangular lattice of wax rods surrounded in air.

The actual dimensions of photonic crystals can then be determined, given the interested frequency. For example, to obtain a bandstop filter for TE polarization operating at 0.25 THz, the period and air column radius were then calculated to be 0.60 mm and 0.22 mm, respectively. Similarly, a = 0.80 mm and r = 0.296 mm were obtained for 0.187 THz bandstop filter. For TM polarization, the rods radius r = 0.175 mm and a = 0.624 mm was designed for bandgap around 0.25 THz, and the rods radius r = 0.233 mm and a = 0.833 was designed for bandgap around 0.187 THz. Next, three-dimensional computer aided design (CAD) models were generated for the designs by SolidWork. The overall dimensions of the samples are 24 mm x 24 mm, and there are a total of either 5 rows or 9 rows of the air columns in the third direction for each design. The data file was exported to the Thermojet printer and the photonic crystals were printed in the direction along the air column. Figure 6.12 shows examples of (a) the 3-D model of the 2-D triangular lattice of air columns in the wax; (b) the top view of a 2-D photonic crystal with air columns embedded in the wax; (c) the 3-D model of the 2-D triangular lattice of wax rods; (d) the top view of a 2-D photonic crystal with wax rods.

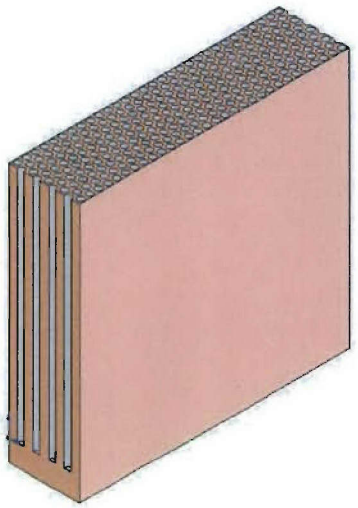

(a)

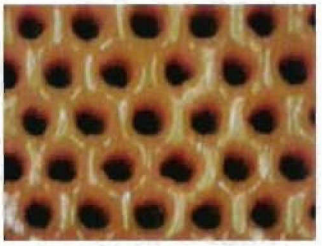

(b)

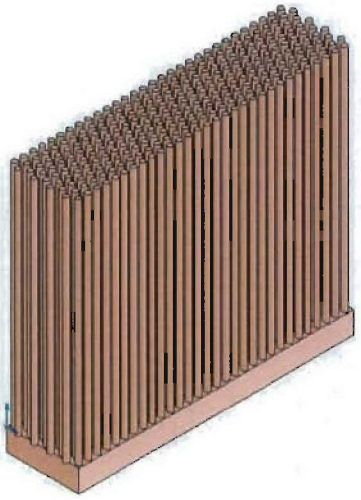

(c)

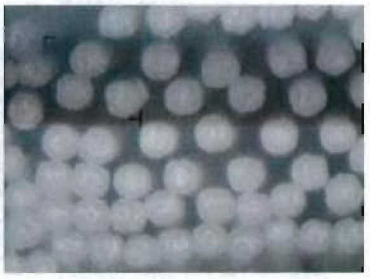

(d)

Figure 6.12 (a) the 3-D model of the 2-D triangular lattice of air columns in the wax; (b) the top view of a 2-D photonic crystal with air columns embedded in the wax; (c) the 3-D model of the 2-D triangular lattice of wax rods; (d) the top view of a 2-D photonic crystal with wax rods.

Measurements of the periods and air column radii for samples were approximately 2% smaller than designed. This discrepancy was attributed to wax shrinkage during the cooling process. The effect can be compensated by programming the wax shrinkage rate in the printer. The variation in the air column radius is roughly within ±10% and is attributed to the limitation in the "printing" resolutions. Figure 6.12(d) shows that the array of rods can not maintain their position because of the high aspect ratio between the rod length to the diameter and the wax is a soft material. A solid block of wax is required

on the top of the structure to keep the rods in their place. However, the supporting wax will then be used during the printing process to support the top block. Due to the small space between the rods (<0.5mm), it is extremely difficult to remove the supporting wax after the printing process.

There are total four types of wax samples based on the triangular lattice of air columns structures were successfully fabricated using Thermojet® printer, listed in Table 6.2. There were at two samples made for each type of structure.

Table 6.2. Summary of the sample types based on the triangular lattice of air columns structure.

Type	Lattice constant a (mm)	Radius r (mm)	Periods in Γ-M direction	Expected frequency of the bandgap
1	0.586	**0.183**	5	**0.250 THz**
2	0.586	**0.183**	**9**	**0.250 THz**
3	0.787	0.254	5	0.187 THz
4	0.787	0.254	**9**	0.187 THz

6.4.4 Results and Discussion

Transmission spectra of the photonic crystals with the triangular lattice of air columns were measured with a Bruker IFS 66v FTIR. A wire grid polarizer was placed between the far infrared source and the sample for measurement in TE and TM polarizations, respectively. For each type of sample, a solid block of ThermoJet® wax with comparable thickness was fabricated and its transmission spectral was measured for comparison to the photonic crystal.

Figure 6.13 shows the calculated dispersion relations of the photonic crystal (left-hand side) and experimental transmission spectra (right-hand side) of the sample of 9 rows air columns with a = 0.586 mm and r = 0.187 mm (Type 2) for (a) TE and (b) TM polarization. The dotted curves on the right-hand sides are the spectra of the reference wax block for TE and TM polarization. The general trends show that the transmission loss of increases with frequency and is independent of polarization. The fringes are caused by interference between the light reflected from the front and back surfaces of the solid wax block. The plane wave expansion simulations show a TE bandgap from 0.256 THz to 0.263 THz (Fig. 6.13 a)), while there exists no TM bandgap for all wave vector directions (Fig. 6.13 b)). However, in the Γ-M direction, the direction of the wave propagation in the experiment, the gap extends from 0.224 THz to 0.263 THz for TE polarization and there is a small gap from 0.221 THz to 0.245 THz for TM polarization. As predicted by the simulations, a clear transmission dip was observed in the TE spectrum from 0.208 THz to 0.255 THz (solid curve on the right-hand side plots) of the type 2 sample, which indicates the presence of photonic crystal effect. The TM spectrum measured on the same sample showed a narrow dip from 0.208 THz to 0.233 THz, which can be explained by the smaller gap predicted by the dispersion relation.

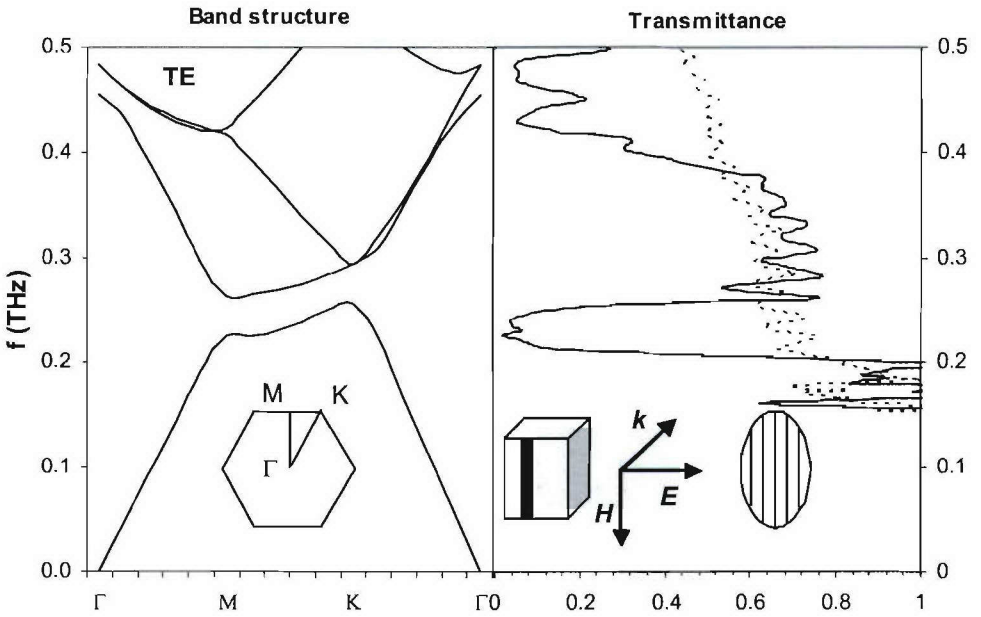

(a)

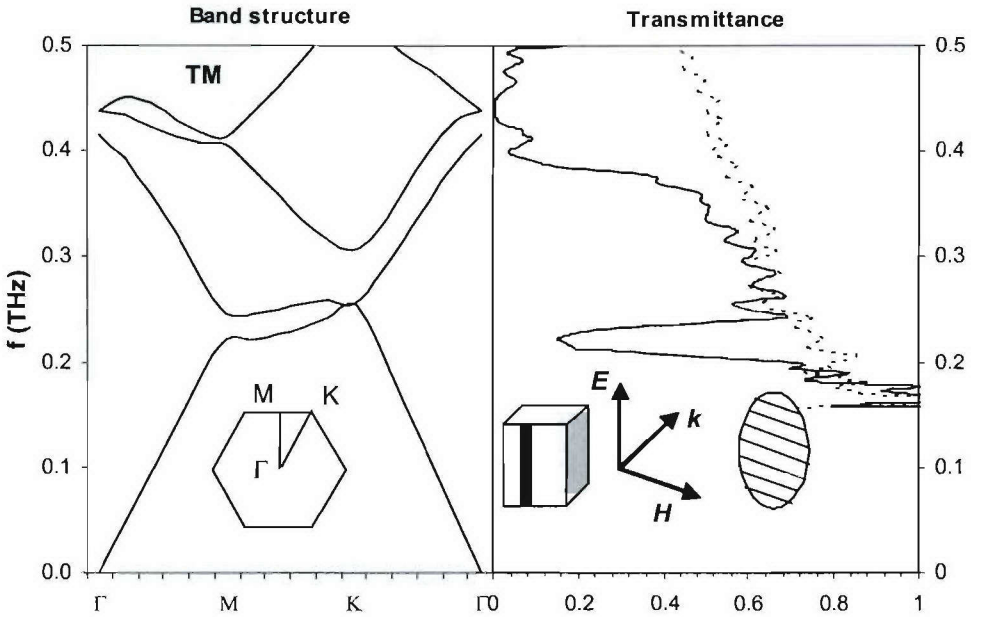

(b)

Figure 6.13. The dispersion ration (left-hand side) and transmittance (right-hand side) of a photonic crystal with triangular lattice of air columns in a wax substrate for (a) TE polarization and (b) TM polarization. The insets in the left-hand sides show irreducible Brillouin zone. The sample orientation, light polarization and wire grid polarizer are shown on the right-hand side plots. A small bandgap around 0.26 THz was calculated for TE polarization.

According to the scaling law of photonic crystals, the wavelength of the bandgap will change proportionally with respect to the dimensions of the structure. For the sample with a = 0.787 mm and r = 0.254 mm (Type 3 and Type 4), the bandgap in Γ-M direction were predicted to be shifted to from 0.167 THz to 0.193 THz for TE polarization and from 0.165 THz to 0.183 THz for TM polarization, respectively.

The results of observed photonic bandgap frequencies and the simulations for all types of samples are summarized in Table 6.3 for comparison. For each sample, the locations of the TE and TM gap are in good agreement with the gaps between first and second TE and TM bands in the Γ-M direction as predicted by the theoretical calculations. The measured TE band widths are around 20% wider than the ones calculated and the observed TM band width is only around 5% wider than the simulation. This is attributed to two factors. First and the most important is the non-uniformity in the radius of the air column, with an up to ±10% variation that can effectively broaden the bandgap. Secondly, the FIR source used in the Bruker is mainly TM polarized. The weaker signal in the TE polarization may contribute more to the uncertainty in determining the band edges in the transmission spectrum.

Table 6.3. Comparison of the measured photonic bandgap frequencies in Γ-M direction with the calculated ones. The simulation assumes ε = 2.16.

Type	a (mm)	r (mm)	TM gap (THz)		TE gap (THz)	
			Simulation	Measured	Simulation	Measured
1	0.586	0.183	0.221 – 0.245	**0.215 – 0.240**	0.224 – 0.263	**0.213 – 0.264**
2	0.586	0.183	0.221 – 0.245	**0.208 – 0.233**	0.224 – 0.263	**0.208 – 0.255**
3	0.787	0.254	0.165 – 0.183	**0.163 – 0.181**	0.167- 0.193	**0.161 - 0.201**
4	0.787	0.254	0.165 – 0.183	**0.158 – 0.177**	0.167- 0.193	**0.159 – 0.190**

6.4.5 Conclusions

We explored and demonstrated functional photonic crystals made from ThermoJet® wax using rapid prototyping method. This method can produce 2D and 3D photonic crystal structures easily and cheaply. The stop bands were observed around 0.167 THz and 0.225 THz for photonic crystals with periods of 0.586 mm and 0.787 mm, respectively. The results agree with the theoretical calculations. In the future, the freeforming method is expected to bridge the dimensional gap between the micromachining and lithography methods. However, the ThermoJet® printer as well as other current available solid freeforming technologies lack the resolution to produce crystals operating in the terahertz regime. In addition, the high electromagnetic absorption of the current wax materials at terahertz frequencies also limits the technique's potential for terahertz applications.

6.5 THz Waveguides Using GaAs Based Photonic Crystals

6.5.1 Material Selection

Due to limitations in the optical properties of the material and the resolution of the structure with the ThermoJet rapid prototyping method for terahertz application as discussed in Section 6.4, the semiconductor materials and their processing methods were investigated to develop terahertz photonic crystals. The ideal material should have high dielectric constant and low extinction ratio at the terahertz regime. The high dielectric constant widens the bandgap and the low extinction ratio is important to have minimal material loss. The n-type GaAs wafer with crystal orientation of 100 showed the index of refraction (n) of 3.746 and the extinction coefficient (k) of 0.0036 at the frequency of 1.56 THz, and is a good candidate for the terahertz devices. The GaAs material is also interested because it offers the potentials to integrate the photonic crystal structures with the GaAs/AlGaAs material system based quantum cascading laser or the photodetectors.

6.5.2 Device Design

There are two basic types of photonic crystal slabs. One is the lattice of the high dielectric constant (ε) rods in low dielectric constant media; and the other is constructed by the lattice of low ε holes in the slab with high dielectric constant (illustrated in Fig. 6.14). The air is conveniently used as the low ε medium in those structures. Similar to the 2-D photonic crystals, the dielectric rods slab has a bandgap in odd modes (TM like) while the dielectric slab with air holes has a bandgap in even modes (TE like). It was also shown [6.14] that the widest bandgap was achieved when the slab thickness t is around $2a$, where a is the lattice constant, for the dielectric rods slab, whereas the slab thickness $t \approx 0.6a$ is required for the dielectric slab with air holes to achieve the maximal bandgap. The thinner slab implies less etching time for the holes and therefore less stringent requirement on the vertical straightness of the wall. In addition, the connectivity of the dielectric material for the hole structure is also a preferred feature for semiconductor fabrication processes. Therefore, triangular lattice of air holes in GaAs slab is selected as the photonic crystal structure.

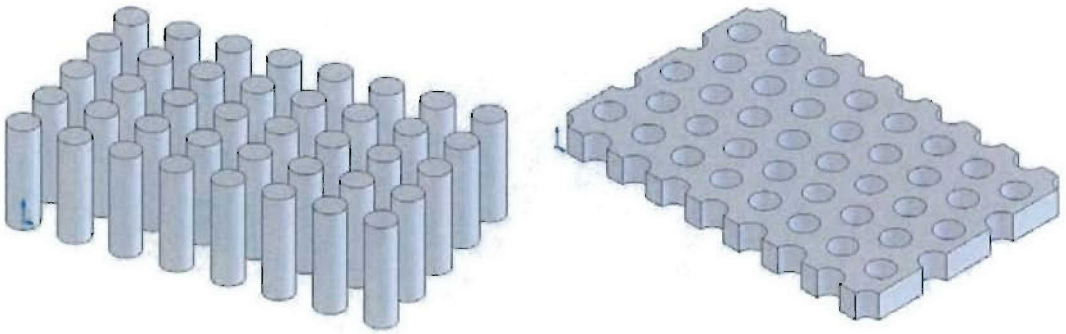

(a) (b)

Figure 6.14 Photonic crystal slabs (a). Square lattice of high ε rods in low ε medium (b). Triangular lattice of low ε holes in a high ε medium.

First, theoretical computation of the band structure was performed using the MIT Photonic-Bands package running in Linux environment. Given the dielectric constant ε = 14 for GaAs, the radius of the hole r and the slab thickness t were varied to calculate the band structures. A typical band diagram for a slab based on GaAs material is shown in Figure 6.15. The shaded area is the light cone due to the index guiding in the vertical direction. The calculated band structures showed that the band gap changes as a function of the hole radius r and the slab thickness t (Fig. 6.16). The band gap size was calculated as the percentile relative to the midgap frequency of the lowest band gap. It is evident that the band gap widens with increased hole radius. And for a given hole radius r, there is an optimal slab thickness t with which the gap is maximal, as expected. The band gap size is less sensitive to the slab thickness for the structure with smaller hole radius.

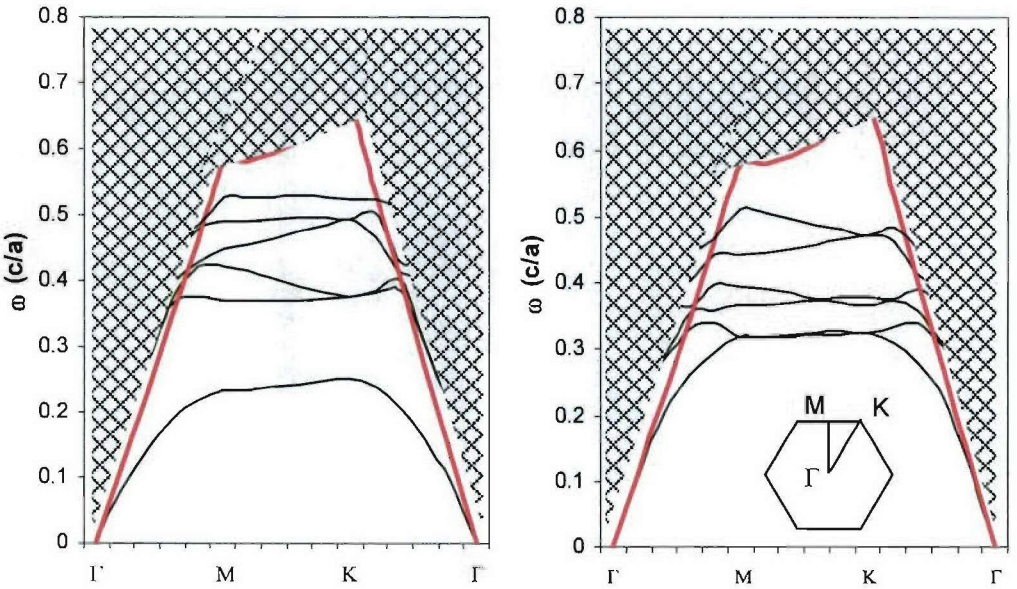

(b)

Figure 6.15. Band diagram for the photonic crystal slab (r = 0.3 a, t = 0.6 a, ε = 14). The shaded areas represent the radiation modes.

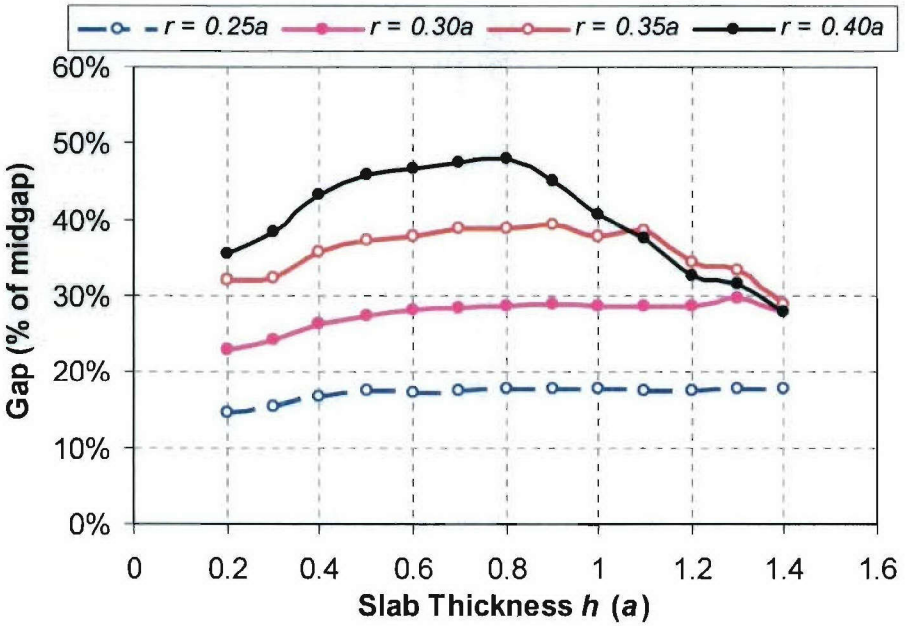

Figure 6.16. Photonic band gap size as a function of the slab thickness and the hole radius.

However, for the photonic crystal slab with large air holes, the spacing between the adjacent holes is reduced. Consequently, it is difficult to etch the pattern with large holes if a thick slab is also required. The adjacent holes can cross over at the bottom of the slab

because of the variability in the fabrication process and small tapering of the wall during the holes formation. To prevent it from happening, the hole radius $r = 0.3\ a$ and the slab thickness of $t = 0.6\ a$ are selected for our design. Figure 6.15 shows an even (TE-like) bandgap at frequency $\omega = 0.251\text{-}0.368$ in the unit of c/a. To form a bandgap around the frequency of 1.56 THz or 191 μm, the lattice constant a, hole radius r, and the slab thickness t can be calculated as below:

$a = 0.30 * \lambda = 0.30 * 191\ \mu m = 58\ \mu m$
$r = 0.30 * a = 0.30 * 58\ \mu m = 17\ \mu m$
$t = 0.60 * a = 0.60 * 58\ \mu m = 35\ \mu m$

The terahertz photonic crystal slab thickness is around 30-40 μm. This is much thicker than the slab thickness for near infrared application which is usually less than 1 μm. Therefore, the epitaxy growth methods used for near infrared photonic crystal slab becomes impractical for terahertz applications. Wafer thinning is instead used. On the other hand, the slab is very thin and is difficult to handle by itself. A supporting substrate is often required. To avoiding breaking the symmetry of the slab, an air gap between the substrate and the slab is required. The final designs of the structures are shown in Fig. 6.17.

In Fig. 6.17 a), a 35 μm thick photonic crystal GaAs slab is placed on the top of a supporting substrate. There are 18 periods of holes along Γ-K direction. To reserve the slab symmetry, an air pocket should be created in the substrate. The depth of the air pocket should be comparable to the wavelength so that the guided mode amplitude is negligible beyond the gap. Therefore, a depth around 190 μm is required for the terahertz application. The candidate substrate should be relatively easy to be etched deeply. It should also be insensitive to the etchant used for the GaAs slab. The InP wafer satisfies both criteria. It can be etched 100 μm deep with hydrochloric acid (HCl) in several minutes at 30°C, and it is insensitive to the H_2SO_4:H_2O_2:H_2O etching system used for GaAs. In addition, the doped InP wafer is opaque to terahertz frequency, thus preventing any mode coupling between the photonic slab and the supporting substrate. There are rectangular holes on the four corners of GaAs slab to form the input and output ridge waveguides. These holes also serve as the alignment marks with respect to the supporting substrate. Figure 6.17 b) shows a waveguide structure by creating a line defects along Γ-K direction of the triangular lattice of air holes. The taper structure was used to improve coupling the wave in and out the line waveguide. To facilitate the characterization, a GaAs slab with the same input and output ridge waveguide was fabricated adjacent to the photonic crystal structures as the testing reference, shown in Figure 6.17 c).

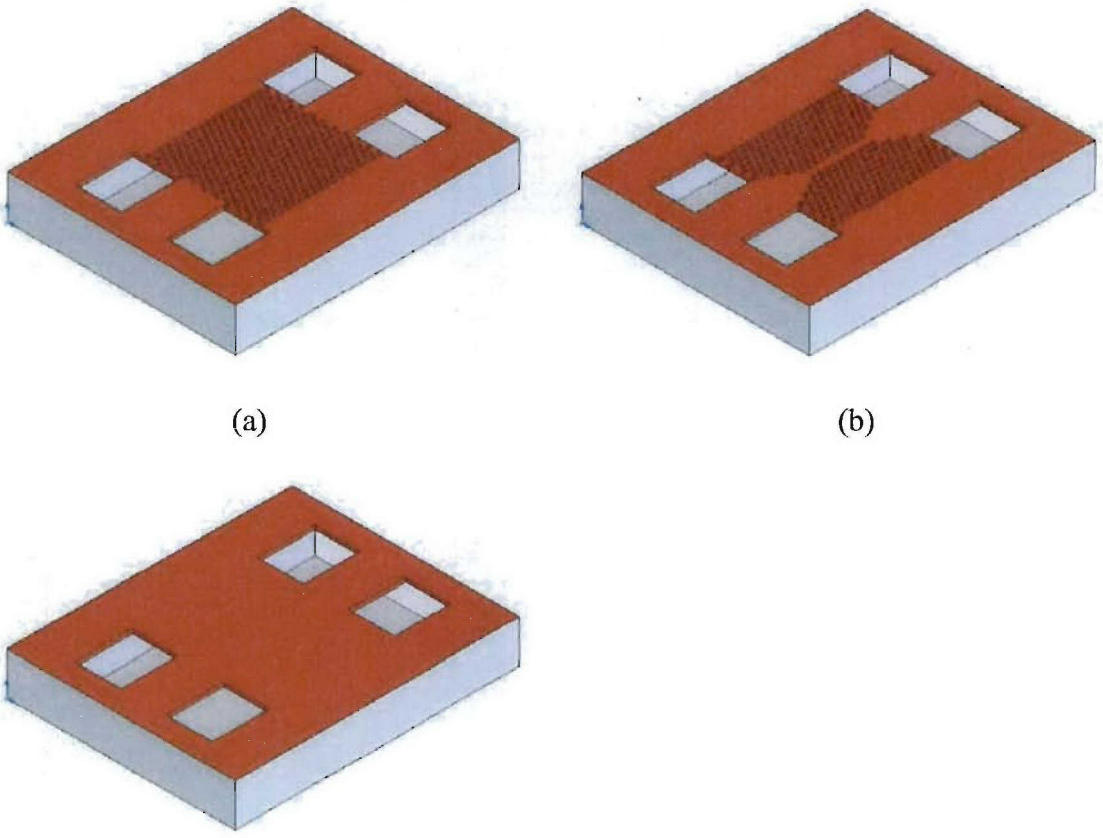

(a) (b)

(c)

Figure 6.17. (a) Schematics of the perspective view of the photonic crystal slab (b), taper coupling to a defect mode (c) Characterization reference slab.

6.5.3 Device Fabrication and Process Development

There are several challenges in fabricating the structure shown in Fig. 6.17. First, the slab is too thick to grow using epitaxy method such as Molecular Beam Epitaxy (MBE). The GaAs is usually grown at 1.0 μm/hr with MBE. A 35 μm slab would take 35 hours to grow at this rate and thus is impractical. On the other hand, it becomes very difficult to thin the wafer from 350 μm or 512 μm down to 30 to 40 μm. Even though thinning wafer down to 100 to 150 μm has been an industry practice, the GaAs wafer becomes extremely fragile when it is to be thinned further. Secondly, a strong and reliable bonding between the GaAs slab and the supporting substrate is important to keep the sample intact for the following photolithography and etching processes. Thirdly, a dry etch process with high directionality is critical to achieve a vertical wall for the holes through the GaAs slab. A significant effort has been taken to research and develop these processes.

The fabrication process consists of three steps. First step is to create the air pockets in the InP supporting substrate. Then, a GaAs wafer is thinned and bonded to the patterned InP substrate. A further thinning is accomplished by chemical wet etching. Finally, the triangular lattice of air holes are created on the GaAs slab and the sample is cleaved into individual bars.

6.5.4 The InP Supporting Substrate Fabrication Process

To fabricate the InP supporting substrate, the conventional semiconductor photolithography and wet etching methods were used. The procedure is shown in Fig. 6.18. The positive photoresist (AZ4620) is first spun on the InP wafer at 3000RPM. The contact printing is then used to transfer the pattern from the mask to the wafer (a). After developing and a hard bake at 110°C, a metal mask of thin film composing of Ni/Ge/Au (30.0nm/40.0nm/250.0nm) is deposited on the sample surface by electron beam evaporation (b). The recipe of the metal film is selected to withstand the chemical etchants such as HCl, H_2SO_4:H_2O_2:H_2O that are used in the sequential process. The metal film of Ti/Au (30.0nm/200.0nm) which was first experimented peeled off during wet etching with H_2SO_4:H_2O_2:H_2O. In the next step (c), the photoresist is then lifted off by soaking the coated sample in acetone bath and a metal mask is formed on the InP wafer. The sample is then attached to a glass slide with un-patterned side down using black wax. The wax is also applied along the perimeter of the sample to prevent the acid from seeping into the back of the wafer (d). The wax protected sample is etched then in HCl at 35°C for 3 min to create the air pockets, and rinsed under running DI water for 10 min (e). The air pocket is roughly 160 μm in depth. Finally, the sample is soaked in trichloroethalene for several hours to fully remove the black wax (f). The sample is then cleaned with fresh trichloroethalene, acetone, methanol, and isopropanol, and dried with Nitrogen.

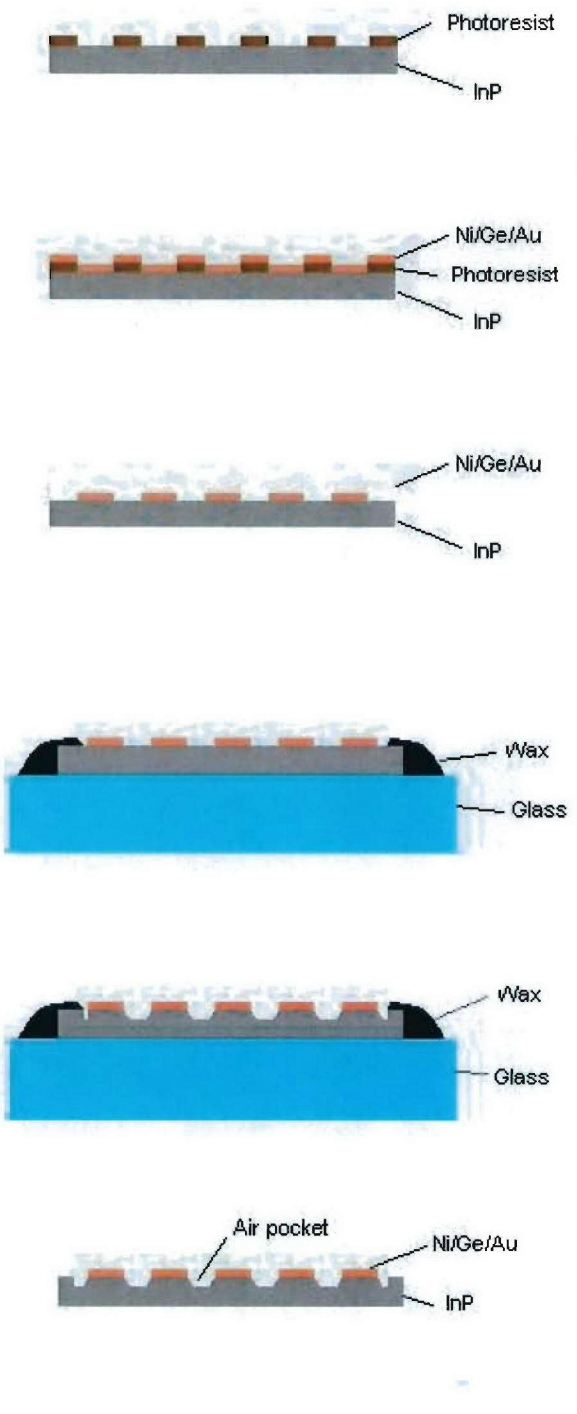

Figure 6.18 Schematics of the fabrication procedure of the InP substrate.

6.5.5 The Thin GaAs Slab Fabrication Process

A GaAs wafer is first polished down to around 125 μm manually. Benzocyclobutene (BCB) is first spun on the patterned InP wafer (Fig. 6.19 a)) and pre-baked. The thinned GaAs wafer is then bonded to the InP wafer at elevated temperature. Both InP and GaAs wafer have the same crystal orientation (100) and are positioned with the cleavage planes aligned (Fig. 6.19 b)). The bonded sample is then etched in H_2SO_4:H_2O_2:H_2O etching system for around 2.5 hours to reach the final thickness of the GaAs slab to around 30-40 μm.

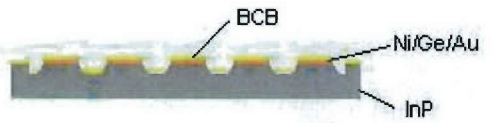

(a)

(b)

Figure 6.19. The GaAs slab fabrication procedure.

6.5.6 The Fabrication Process of the Photonic Crystal GaAs Slab

The procedure to fabricate the photonic crystal on the thin GaAs slab is shown in Fig. 6.20. In this process, photoresist is used as the softmask during the dry etching at elevated temperature. The positive photoresist AZ 1512 showed better resilience to the high temperature around 100°C for extended hours than AZ 4620 and thus is selected for the photolithography procedure. AZ 1512 is first spun on the thinned GaAs sample at 3000RPM and then soft baked at 90°C for 30 min. A contact aligner is used to align the photonic crystal patterns to be transferred on the GaAs slab relative to the air pockets previously created on the InP supporting wafer before the UV exposure. The sample is then developed in AZ 327 K developer and rinsed under running DI water for 10min (a). Then the sample is subject to a hard baked at 110°C for 10 min. Next, the sample is loaded into Bromine Ion-Beam Assisted Etching (Br-IBAE) system. Because the actual temperature on the sample surface can increase with time due to the increased heat from the Argon gun over time, the continuous etching at elevated temperature for several hours could burn the photoresist. The Br-IBAE etching is done in several sessions of 45 min each with a half hour interrupt to allow the sample surface to cool down. In each session, the sample holder is first heated to around 90°C with the resistance heating. After a vacuum pressure of 2.0 x 10^{-7} Torr is reached, 5 min Argon ion milling is first done to remove the surface oxides. Then the sample is etched under Bromine pressure of 0.040mmHg for 45 min. The sample holder temperature is then returned to the ambient temperature and the Argon ion gun is shut down. After a half hour interrupt, the same

procedure is repeated until the holes are etched through the slab (b). Next, the sample is removed from the etcher and the photoresist is cleaned with acetone (c). The wafer is then cleaved intro bar.

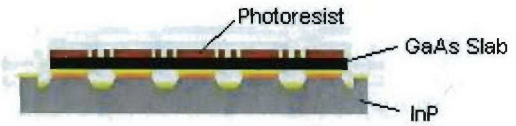

(a)

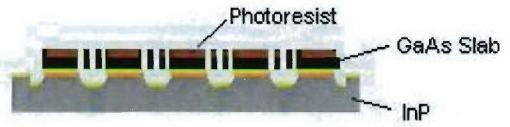

(b)

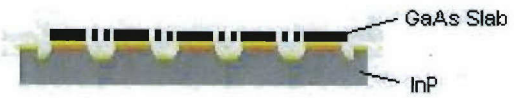

(c)

Figure 6.20. The photonic crystal slab fabrication process.

Figure 6.21 shows the images of the photonic crystal slabs successfully fabricated from GaAs material. The current effort is focusing on setting up the characterization station using a far infrared (FIR) laser optically pumped by a CO_2 laser. The frequency of the FIR laser can be tuned to scan from 1 THz to 3 THz by changing the low pressure molecular gas of FIR laser, tuning the grating of the CO_2 laser and the cavities of both lasers. The transmitted signal through the sample is collected by a Helium cooled bolometer.

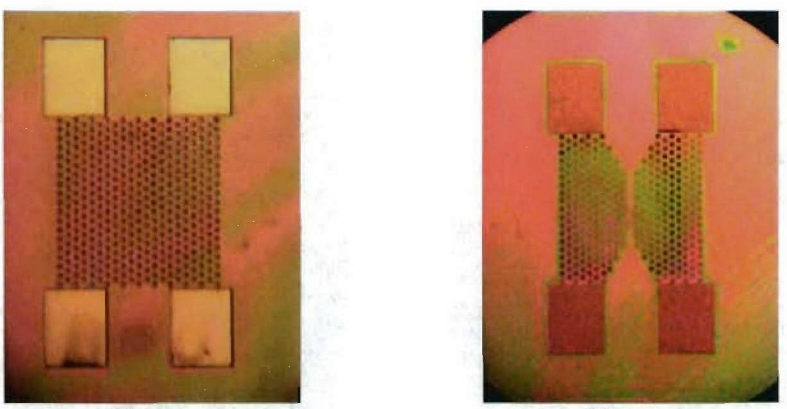

(a) (b)

Figure 6.21. Top view of the photonic crystal slabs: (a) triangular lattice of air columns in GaAs slab; (b) photonic crystal slab waveguide with taper structure.

6.6 Concealed Weapon Imaging Experiment

As part of the effort, the group discussed possible applications for the technology. One area where the UMass Lowell Submillimeter-Wave Technology Laboratory (STL) excels is in remote terahertz imaging. Prof. J. Waldman and Mr. J. Dickinson ordered a mannequin and dressed it in a flannel shirt along with a concealed a tie-wrap gun. They then imaged the object in the THz. The optical and 1.56 THz images of the mannequin are shown in Fig. 6.22 . The actual terahertz data set forms a short animated film of the mannequin being rotated about 100 degrees and is available on request.

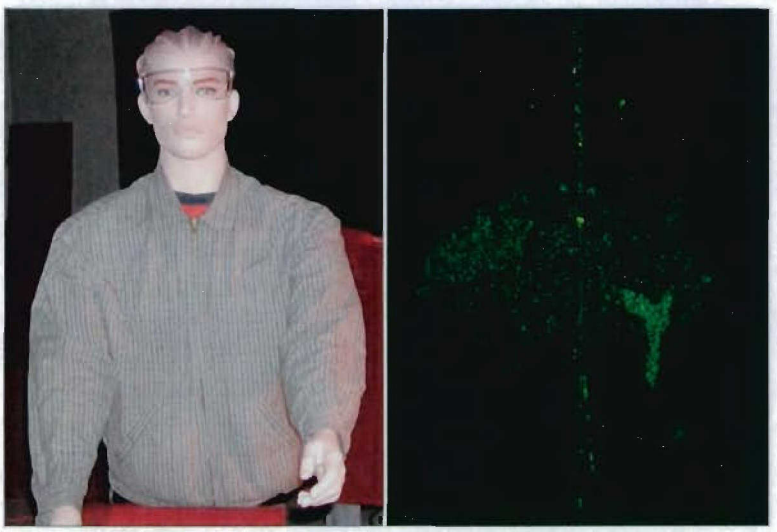

(a) (b)

Figure 6.22. Part (a) Optical image of a mannequin with concealed weapon. Part (b) 1.56 THz image of the mannequin. The image was taken about 25 m away from the transceiver.

The image was generated using CO_2 pumped gas THz lasers with the transmitter and local oscillator operating at 1.5626 and 1.5645 THz. Detection was accomplished with a quasi-optical Schottky diode mixer with an NEP of 10^{19} Watts/Hertz. The transmitter power was 50 to 100 mW (CW). The pixel resolution was 1 mm x 1mm and the standoff distance from the transmitter was 25 m. The pseudo-color scale of the image runs from -10dB per square meter (white) to -80 dB per square meter (Black). The laser power on the subject was 2 x 10^{-5} Watts/cm^2 and the acquisition time was 3 minutes.

The STL has a number of test beds that can be immediately used to test terahertz imaging, remote sensing, chemical sensing, and biological sensing concepts at frequencies from 0.3 to 5.0 THz. Such a capability allows one to experimentally determine or to verify the appropriate frequency for an application without having to first develop the high-risk components of a system and then build them before the first data can be taken to verify the concept.

6.7 Summary of THz Effort Technical Achievements

Significant progress was made in the THz QCL effort. We are close to being able to specify a wavelength and then have the model determine an optimized module. In the phonon effort we have reproduced earlier results and are close to finishing the modeling of modules that will help us more carefully understand the interface modes of these structures. At the same time a new four-well module has been designed and grown as a cascade laser in house and at Wright-Patterson AFB. We will be testing the laser for emission and lasing shortly with our optimized step-scan Fourier transform spectrometer. During the period we have demonstrated that frequency selective surfaces can be used to control the reflectivity of high-index semiconductors. Such surfaces may be used to control the facet reflectivity of these low-gain lasers. We have also developed THz waveguide designs using photonic crystals with an eye to making very robust portable systems. The waveguide work will also help us develop an optical transition component for use between the highly-divergent QC laser and the rest of the system. Finally, we have shown that a coherent THz imaging systems can be built to find weapons under clothing at a resolution of 1 mm x 1 mm from a range of 25 m.

6.8 Reference

6.1 Vinod M. Menon, W.D. Goodhue, A.S. Karakashian, and L.R. Ram-Mohan, "Phonon mediated lifetimes in intersubband terahertz lasers," J. Appl. Phys. 88, 5262 (2000).

6.2 V.M. Menon, "Design, fabrication, and characterization of quantum cascade terahertz emitters," Ph. D. Thesis, University of Massachusetts Lowell (2001).

6.3 "Role of Interface Phonons in Quantum Cascade Terahertz Emitters", V. M. Menon, L. R. Ram-Mohan, W. D. Goodhue, A. J. Gatesman, A. S. Karakashian, *Physica B* **316-317**, 212-215 (2002).

6.4 V. M. Menon, L. R. Ram-Mohan, W. D. Goodhue, A. S. Karakashian, A. Naweed, A. Gatesman, J. Waldman, "Phonon Engineered Quantum Cascade Terahertz Emission", *Physica E* **15**, 197-201 (2002).

6.5 V. M. Menon, W. D. Goodhue, A. S. Karakashian, L. R. Ram-Mohan, " Wave guide design optimization of a quantum cascade laser emitting at 77 μm", *Proceedings of the Conference on Intersubband Transitions in Quantum Wells 1999,* Austria (1999).

6.6 V.M Menon, W.D. Goodhue, A.S. Karakashian, A. Naweed, J. Plant, L.R. Ram-Mohan, A. Gatesman, V. Badami, and J. Waldman, " Dual-frequency quantum-cascade terahertz emitter," Appl. Phys. Lett. 80, 2454 (2002).

6.7 R. Koehler, A. Tredicucci, F. Beltram, H.E. Beere, E.H. Linfield, A.G. Davies, D.A. Ritchie, R.C. Iotti, and F. Rossi, "THz quantum cascade laser", Bull. Am. Phys. Soc., (2002).

6.8 Benjamin S. Williams, Hans Callebaut, Sushil Kumar, Qing Hu, and John L. Reno, "3.4 THz quantum cascade laser based on longitudinal-optical-phonon).

6.9. Jerome Faist, Federico Capasso, Deborah L. Sivco, Carlo Sitori, Albert L. Hutchinson, and Alfred Y. Cho, "Quantum cascade laser", *Science*, vol 264, pp. 553-556, Apr. 22, 1994.

6.10. Mattias Beck, Daniel Hofstetter, Thierry Aellen, Jerome Faist, Ursula Oesterle, Marc Ilgems, Emilio Gini, and Hans Melchior, "Continuous wave operation of a mid-infrasred semiconductor laser at room temperature", *Science*, vol 295, pp. 301-305, Jan. 11, 2002.

6.11. Barbieri, S., Alton, J., Dhillon, S. S., Beere, H. E., Evans, M., Linfield, E. H., Davies, A. G., Ritchie, D. A., Köhler, R., Tredicucci, A., and Beltram, F., "Continuous-wave Operation of Terahertz Quantum-Cascade Lasers," *IEEE Journal of Quantum Electronics*, vol. **39**, no. **4**, (2003).

6.12. Hecht, Optics, 2nd edition, Addison-Wesley Publishing Company, Inc, pp363-372, 1989.

6.13 Johnson, S. G., and Joannopoulos, J. D., "Block-Iterative Frequency-Domain Methods for Maxwell's Equations in a Planewave Basis," *Optics Express*, **8**(3), p173-190, (2001).

6.14. G. Johnson, S. Fan, P.R. Villeneuve, and J.D. Joannopoulos, "Guided modes in photonic crystal slabs," Physical Review B., 60(8), p5751-5758, 1999

7. Personnel, Thesis, Conference and Journal Papers

At the University of Massachusetts Lowell Prof William Goodhue, Photonics Center, served as the Principal Investigator of the project with Prof. Changmo Sung, Center for Advanced Materials (CAM), serving as the Co-principal Investigator (until his departure from the university in 2004). Prof. James Whitten of CAM, and Prof. Jerry Waldman of the Submillimeterwave Technology Laboratory (STL) also played important roles in the project in the areas of surface analysis and terahertz technology, respectively. Dr. Lisa Allen of Galaxy Compound Semiconductors, Inc. (formally with Epion, Inc), and Prof. Ramdas Ram-Mohan, Quantum Semiconductor Algorithms, Inc. provided expertise in the areas of ion beam processing and theoretical modeling, respectively. Mr. Christopher Santeufemio (UMass) provided AFM characterization and Mr. William DeFeo (UMass) provided optical charachterization assistance. Dr. David Bliss of AFRL/SNHC was the Principal investigator of the bulk growth portion of the project with Dr. Gerry Isler of Isler Associates his Co-Principal investigator. Dr. Thomas Nelson AFRL/SNDD, Dr. James Ehret AFRL/Materials Directorate and a number of UMass Lowell graduate and undergraduate students were also involved in the project. The UMass Lowell graduate students who received a degree based on there work in the project included, Xianglin Li, M.S., Department of Chemical Engineering, Maria Ospina, M.S., Department of Chemical Engineering, Shiva Vangala, M.S. Physics Department, William Saggio, M.S. Physics Department, and Kannan Krishnaswami, Ph.D., Physics Department. Furthermore graduate students Jin Li (terahertz photonic crystals and Beihong Zhu (QCL's) are expected to finish their Ph.D thesis work over the next 9 months.

7.1 List of Completed Theses

1. Xianglin Li, "Nano-charterization of Gas Cluster Ion Beam Processed Gallium Antimonide Substrate Surface by Atomic Force Microscopy and X-ray Photoelectron Spectroscopy," UMass Lowell Department of Chemical Engineering, M.S. Thesis (C. Sung, Advisor) 2002.

2. Maria C. Ospina, "Nano-characterization of Surface Engineered Gallium Antimonide and Investigation of its Mechanical Properties," UMass Lowell Department of Mechanical Engineering, M.S. Thesis (C. Sung, Advisor) 2003.

3. William J. Saggio, "Calibration of the Throughput of a Fourir Transform Interferometer for the Purpose of Characterizing a Quantum Cascade Laser," UMass Lowell Department of Physics, M.S. Thesis (J. Waldman, Advisor) 2004.

4. Kannan Krishnaswami, "Preparation of Epiready GaSb Substrates with Gas Cluster Ion Beams," UMass Lowell Department of Physics, Ph. D. Thesis (W. Goodhue, Advisor) 2004.

5. Shivashankar R.Vangala, "Development of Epi-ready Bromine ion-Beam-Assisted etched GaSb Substrates for GaSb molecdular Beam Epitaxy," UMass Lowell Department of Physics, M. S. Thesis (W. Goodhue, Advisor) 2005.

7.2 List of Conference and Journal Papers

1. 1. L.P Allen, T.G. Tetreault, C. Santeufemio, X. Li, W.D. Goodhue, D. Bliss, M. Tabat, K.S. Jones, G. Dallas, D. Bakken, and C. Sung,"Gas-cluster ion-beam smoothing of chemo-mechanical-polish processed GaSb (100) Substrates," Jour. Electron. Matt. 32, 842 (2003).

2. X. Li, W.D. Goodhue, C. Santeufeimio, T.G. Tetreault, R. MacCrimmon, L.P. Allen, D. Bliss, K. Krishnaswami, and C. Sung, "Gas cluster ion beam processing of gallium antimonide wafers for surface and sub-surface damage reduction," Appl. Surface Science (in press).

3. K. Krishnaswami, L.P. Allen, C. Santeufemio, X. Liu, S.R. Vangala, M.C. Ospina, B. Zhu, J. Whitten, C. Sung, D. Bliss, G. Dallas, D. Bakken, K.S. Jones, and W.D. Goodhue, "Epitaxial growth on gas cluster ion beam processed GaSb substrates using molecular beam epitaxy," Journ., Vac. Sci. and Technol. B, Vol. **22(3)**, 1455-1459 (2004)

4. S.R. Vangala, B. Krejca, K. Krishnaswami, X. Qian, B. Zhu, H. Dauplaise, K. Vaccaro, D. Bliss, W. D. Goodhue, "Preparation and Patterning of GaSb Surfaces with Br-IBAE for Antimonide Based Molecular Beam Epitaxy," Materials Research Society Symposium Proceedings, Vol. **792**, 569-574 (2004)

5. B. Krejca, S.R. Vangala, K. Krishnaswami, R. Kolluru, M.C. Ospina, C. Sung, W.D. Goodhue, "Fabrication of Nanotips and Microbeams in Antimonide Based Semiconductor Material using Bromine Ion Beam Assisted Etching," Materials Research Society Symposium Proceedings, Vol. **792**, 309-314 (2004)

6. K. Krishnaswami, S.R. Vangala, B. Krejca, L.P. Allen, C. Santeufemio, H. Dauplaise, X. Liu, J. Whitten, M. Ospina, C. Sung, D. Bliss, and W.D. Goodhue, "Gas Cluster Ion Beam Processing of GaSb and InSb Surfaces," Materials Research Society Symposium Proceedings, Vol. **792**, 617-622 (2004)

7. K. Krishnaswami, B. Krejca, S.R. Vangala, M. Ospina, C. Sung, L.P. Allen, C. Santeufemio, K. Vaccaro, and W.D. Goodhue, "Determination of nano and sub-nano fluctuations in surface oxides of GaSb with Br-IBAE," Materials Research Society Symposium Proceedings, Vol. **786**, 329-334 (2004)

8. N. Ma, D. F. Bliss, and G. Iseler, "Vertical Gradient Freezing of doped GaSb semiconductor crystals using submerged heater growth and electromagnetic stirring" Journal of Crystal Growth, Vol. **259, 1/2**, 26-35 (2003)

9. Xianghong Wang, Nancy Ma, David F. Bliss and Gerald W. Iseler, "Semiconductor crystal growth by modified vertical gradient freezing with electromagnetic stirring", AIAA Journal of Thermophysics and Heat Transfer, accepted.

10. G. Iseler, D. Bliss, X. Wang, and N. Ma, "Modified Bridgman growth of GaSb and GaAlSb alloy crystals using a submerged heater in the presence of crossed magnetic and electric fields", Presented at: 14th International Conference on Crystal Growth, Grenoble France, Aug. 2004

11. S.R. Vangala, L.P. Allen, V. DiFilippo, C. Santeufemio, J. Li, X. Qian, Y. Park, K. Krishnaswami, B. Zhu, G. Dallas, D. Bliss, H. Dauplaise, K.S. Jones, and W.D. Goodhue, "HBr-based gas cluster ion beam smoothing as a final polish for the production of MBE-epi-ready GaSb wafers," Digest of papers, 2005 International Conference on Compound Semiconductor Manufacturing Technology, 14.24, p 335, April, 2005.

12. K. Krishnaswami, D.B. Fenner, S.R. Vangala, C. Santeufemio, M. Grzesik, L.P. Allen, G. Dallas, and W.D. Goodhue, "Roughness Analysis of Episurfaces Grown on Ion-Beam Processed GaSb Substrates," Mater. Res. Soc. Symp. Proc., B6.3, Vol. 829, 2005.

13. M. Ospina, S. R. Vangala, D. Yang, J. A. Sherwood, C. Sung, and W. D. Goodhue, "Micromechanical Characterization of GaSb by Microbeam Deflection using Nanoprobe and Finite Element Analysis," Mat. Res. Soc. Symp. Proc., A5.14, Vol. 782, 2004

8. Strategic Partnerships for Commercialization

This ABCS effort has spawned two complementary SBIR efforts amongst the collaborators. Under a DARPA/Army SBIR Phase I contract, DAAH01-03-CR018 and the follow-on DARPA/Army sponsored SBIR Phase II contract, W31P4Q-04-C-R001lead by Galaxy Compound Semiconductors, Inc.; Galaxy, UMass Lowell and Epion Corp. are working to commercialize the GCIB process as a final wafer polishing technique. Under an AFOSR sponsored SBIR Phase I contract, FA8650-04-M-5426, again lead by Galaxy; Galaxy, UMass and Epion developed a bromine-based GCIB final polish method for preparing GaSb wafers for superlattice overgrowth. With the ability of both GCIB and ICP to handle large multiple wafer processing runs and a new divergent beam Br-IBAE which was built under this program to process 3 in wafers, there are expected to be opportunities to use the technologies developed here for wafer polishing, wafer patterning/regrowth, and surface preparation prior to applying contact or passivation layers.

9. Summary and Future Work

Over the course of this program, the Photonics Center, the Center for Advanced Materials and the Submillimeterwave Technology Laboratory all of the University of Massachusetts Lowell in partnership with AFRL/SNHC developed technology for producing low defect density substrates and high-quality epi-substrate interfaces for ABCS device applications as well as developing fabrication and device concepts for incorporation into quantum-cascade THz lasers. During the course of the project a number of new technologies were developed and demonstrated. A new Bridgeman-magnetic-stirring antimonide bulk growth method was developed and using the method 1) uniformly selinium n-type doped bulk GaSb crystals were grown, 2) Bulk InGaSb crystals were grown, and 3) GaAlSb bulk crystals were grown. In the areas of wafer polishing and epi-substrate interface control, novel gas cluster-ion-beam (GCIB) final polishing methods, bromine ion-beam assisted etching final polishing methods and inductively coupled plasma final polishing methods were developed that allow control of the epi-substrate interface when molecular beam epitaxy is employed for epigrowth. In the THz portion of the project novel THz photonic crystals were demonstrated and new phonon mediated THz quantum cascade laser design developed.

The ABCS polishing work was moved toward commercialization through two joint collaborations with Galaxy Compound Semiconductors, Inc, a Phase I SBIR to develop bromine-based GaSb GCIB polishing (AFRL) and a PhaseI/II project to develop novel final polishing techniques for GaSb and InSb wafers (DARPA).

On the antimonide side of the effort, future work should be directed at continuing the ternary bulk growth effort and working to find dry-etch final polishing recipes that will work on the ternary bulk materials. On the THz side of the effort, work should continue to develop compact THz sources for imaging applications as well as to develop passive photonic crystal structures for compact THz imaging and remote sensing systems.

10.Acknowledgements and Disclaimer

The Photonic Center and SNHC appreciate the support of DARPA and AFOSR on this project. Special thanks goes to Dr. Jag Shah, Dr. Mark Rosker and Dr. Gernot Pomrenke, the program managers for all their helpful guidance during the project. Thanks also to Lisa Allen, Gordon Dallas and Daniel Barker of Galaxy Compound Semiconductors, Inc.; David Fenner and Allen Kirkpatrick of Epion Corp.; Helen Dauplais of AFRL/SNHC; and George Turner and Christine Wang of MIT Lincoln Laboratory for all of their help and suggestions. The opinions, interpretations, conclusions, and recommendations contained in this report are those of the authors and not necessarily endorsed by DARPA, the United States Air Force or the United States Army.